

COMPUTATIONAL SPECTRAL IMAGING TECHNIQUES USING
DIFFRACTIVE LENSES AND COMPRESSIVE SENSING

A THESIS SUBMITTED TO
THE GRADUATE SCHOOL OF NATURAL AND APPLIED SCIENCES
OF
MIDDLE EAST TECHNICAL UNIVERSITY

BY

OĞUZHAN FATİH KAR

IN PARTIAL FULFILLMENT OF THE REQUIREMENTS
FOR
THE DEGREE OF MASTER OF SCIENCE
IN
ELECTRICAL AND ELECTRONICS ENGINEERING

JULY 2019

Approval of the thesis:

**COMPUTATIONAL SPECTRAL IMAGING TECHNIQUES USING
DIFFRACTIVE LENSES AND COMPRESSIVE SENSING**

submitted by **OĞUZHAN FATİH KAR** in partial fulfillment of the requirements for
the degree of **Master of Science in Electrical and Electronics Engineering De-
partment, Middle East Technical University** by,

Prof. Dr. Halil Kalıpçılar
Dean, Graduate School of **Natural and Applied Sciences** _____

Prof. Dr. İlkay Ulusoy
Head of Department, **Electrical and Electronics Engineering** _____

Assist. Prof. Dr. Figen S. Öktem
Supervisor, **Electrical and Electronics Eng. Dept., METU** _____

Examining Committee Members:

Prof. Dr. Gözde Bozdağı Akar
Electrical and Electronics Engineering Dept., METU _____

Assist. Prof. Dr. Figen S. Öktem
Electrical and Electronics Engineering Dept., METU _____

Prof. Dr. A. Aydın Alatan
Electrical and Electronics Engineering Dept., METU _____

Assist. Prof. Dr. Elif Vural
Electrical and Electronics Engineering Dept., METU _____

Assoc. Prof. Dr. Tolga Çukur
Electrical and Electronics Engineering Dept., Bilkent University _____

Date:

I hereby declare that all information in this document has been obtained and presented in accordance with academic rules and ethical conduct. I also declare that, as required by these rules and conduct, I have fully cited and referenced all material and results that are not original to this work.

Name, Surname: Oğuzhan Fatih Kar

Signature :

ABSTRACT

COMPUTATIONAL SPECTRAL IMAGING TECHNIQUES USING DIFFRACTIVE LENSES AND COMPRESSIVE SENSING

Kar, Oğuzhan Fatih

M.S., Department of Electrical and Electronics Engineering

Supervisor: Assist. Prof. Dr. Figen S. Öktem

July 2019, 103 pages

Spectral imaging is a fundamental diagnostic technique in physical sciences with application in diverse fields such as physics, chemistry, biology, medicine, astronomy, and remote sensing. In this thesis, we first present a modified version of a high-resolution computational spectral imaging modality and develop a fast sparse recovery method to solve the associated large-scale inverse problems. This technique uses a diffractive lens such as a photon sieve for dispersing the optical field. We then extend this technique to obtain super-resolution using an additional coded aperture to spatially modulate the field before dispersion. We also demonstrate the capability of the system in a compressive setting where the entire three-dimensional spectral cube is reconstructed from highly compressed measurements through sparse recovery. In all of the imaging modalities, we numerically illustrate the performance for various settings and obtain promising results. Lastly, we provide a detailed analysis on the spatio-spectral resolution and optimization of the system from both analytical and numerical aspects.

Keywords: Diffractive lens, photon sieve, spectral imaging, sparsity, compressive sensing, inverse problems, super-resolution, image reconstruction

ÖZ

KIRINIMLI LENSLE VE SIKIŞTIRILMIŞ ALGILAMAYA DAYALI HESAPLAMALI SPEKTRAL GÖRÜNTÜLEME TEKNİKLERİ

Kar, Oğuzhan Fatih

Yüksek Lisans, Elektrik ve Elektronik Mühendisliği Bölümü

Tez Yöneticisi: Dr. Öğr. Üyesi. Figen S. Öktem

Temmuz 2019 , 103 sayfa

Spektral görüntüleme fizik bilimleri için temel bir tanılayıcı araç olup fizik, kimya, biyoloji, tıp, astronomi ve uzaktan algılama gibi pek çok alanda kullanılmaktadır. Bu tezde, ilk olarak bir yüksek çözünürlüklü hesaplamalı spektral görüntüleme tekniğinin farklı bir versiyonu sunulmakta ve ilgili büyük ölçekli ters problemlerin çözümü için hızlı bir seyrek gerikazanım yöntemi geliştirilmektedir. Bu teknik, optik alanı dağıtmak için foton süzgeci adı verilen kırınımlı bir lens kullanmaktadır. Geliştirilen teknik, sahneyi uzamsal olarak modüle eden bir kodlu açıklık eklenerek süperçözünürlüklü görüntüleme durumuna genişletilmiştir. Son olarak sistemin kapasitesi sıkıştırılmış durum için incelenmiştir. Bu durumda, yüksek miktarda sıkıştırılmış ölçümlerden seyrek gerikazanım yoluyla üç boyutlu spektral veri kübü geri oluşturulmuştur. Tüm görüntüleme modellerinde performans çeşitli durumlar için sayısal olarak gösterilmiş ve umut verici sonuçlar elde edilmiştir. Son olarak, sıkıştırılmış sistemin uzamsal-spektral çözünürlüğü ve optimizasyonu analitik ve sayısal yönlerden incelenmiştir.

Anahtar Kelimeler: Kırınımlı lens, foton süzgeci, spektral görüntüleme, seyreklik, sıkıştırılmış algılama, ters problemler, süper-çözünürlük, görüntü geriçatımı

To my dear wife Zeynep

ACKNOWLEDGMENTS

First and foremost, I would like to express my sincere gratitude to my supervisor, Asst. Prof. Dr. Figen S. Öktem. Starting from my undergraduate research project, I learned a lot from her about scientific research and writing. I thank her for her guidance and for allowing me to pursue what interested me the most.

I am grateful to Prof. Dr. Gözde Bozdağı Akar, Prof. Dr. Aydın Alatan, Asst. Prof. Dr. Elif Vural, and Assoc. Prof. Dr. Tolga Çukur for showing interest in my studies and accepting to review my thesis.

This work was supported in part by the Scientific and Technological Research Council of Turkey (TUBITAK) under grant 117E160 (3501 Research Program). I also would like to thank TUBITAK for their support under 2210/A Scholarship Program.

I am thankful to my colleagues in ASELSAN Research Center, Dr. Can Barış Top, Mert Kalfa, Serhat İlbey, Berkan Kılıç, and Umut Bahçeci, for creating an enjoyable work environment and for many interesting discussions about scientific and non-scientific topics. A special thanks to Alper Güngör, from whom I learnt a lot about programming and optimization. I also thank Dr. H. Emre Güven for his support and encouragement.

I would like to express my deepest gratitude to my family for their unconditional love, caring, and support throughout my life. I am very lucky to have my mother Şerife and my brothers Furkan and Batuhan beside me in all my endeavors. I am also thankful to my father-in-law Hüsametdin and my mother-in-law Zerrin for their constant emotional support. Finally, I am deeply grateful to my dear wife Zeynep for her endless love, patience, and being my best friend. I dedicate this thesis to her.

TABLE OF CONTENTS

ABSTRACT	v
ÖZ	vii
ACKNOWLEDGMENTS	x
TABLE OF CONTENTS	xi
LIST OF TABLES	xiv
LIST OF FIGURES	xvi
LIST OF ABBREVIATIONS	xx
CHAPTERS	
1 INTRODUCTION	1
2 HIGH-RESOLUTION COMPUTATIONAL MULTI-SPECTRAL IMAGING USING DIFFRACTIVE LENSES	5
2.1 Introduction	5
2.2 Forward Problem	8
2.2.1 Imaging System and Assumptions	8
2.2.2 Continuous Image Formation Model	8
2.2.3 Discrete Model	10
2.3 Inverse Problem	12
2.4 Image Reconstruction Method	14

2.4.1	Computational Complexity	18
2.5	Numerical Results	19
2.5.1	Reconstructions in EUV Band	20
2.5.2	Resolution Analysis	25
2.5.3	Reconstructions in Visible Band	29
2.6	Conclusions	30
3	SPATIAL SUPER-RESOLUTION IN DIFFRACTIVE LENS BASED SPECTRAL IMAGING	33
3.1	Introduction	33
3.2	Forward Problem	35
3.2.1	Photon Sieve Spectral Imaging (PSSI)	35
3.2.2	Coded Photon Sieve Spectral Imaging (C-PSSI)	38
3.3	Inverse Problem	39
3.4	Image Reconstruction Method	40
3.4.1	Computational Complexity	42
3.5	Numerical Results	43
3.5.1	PSSI	43
3.5.2	C-PSSI	49
3.6	Conclusions	50
4	COMPRESSIVE SPECTRAL IMAGING WITH DIFFRACTIVE LENSES	53
4.1	Introduction	53
4.2	Forward Problem	55
4.3	Image Reconstruction Method	56

4.3.1	ℓ_1 -norm Based Regularization	57
4.3.2	ℓ_0 -norm Based Regularization	59
4.3.3	Computational Complexity	60
4.4	Numerical Results	61
4.4.1	ℓ_1 -norm Based Regularization	61
4.4.1.1	Effect of Different Transform Choices	65
4.4.2	ℓ_0 -norm Based Regularization	72
4.4.2.1	Effect of Different Transform Choices	75
4.5	System Analysis	79
4.5.1	Spatial Resolution	79
4.5.2	Spectral Resolution	84
4.5.3	Measurement Plane Optimization	85
4.6	Conclusions	89
5	CONCLUSIONS	91
	REFERENCES	95

LIST OF TABLES

TABLES

Table 2.1 PSSI reconstruction algorithm	18
Table 2.2 PSNR (dB) and SSIM values for different input SNRs when <i>moving detector</i> (MD) and <i>fixed detector</i> (FD) measurement settings are used. SNR and PSNR values are reported in decibel (dB).	25
Table 2.3 PSNR (dB) and SSIM values for different number of sources (P) and measurements (K) for 25 dB SNR.	25
Table 2.4 Comparison of mean PSNRs (dB) and SSIMs for different SNR levels when the FD measurement setting is used.	30
Table 3.1 Spatial super-resolution in PSSI algorithm	43
Table 3.2 PSNR(dB)/SSIM values for EUV band images ($K = 2$).	45
Table 3.3 PSNR(dB)/SSIM values for visible band images ($K = 6$).	45
Table 3.4 PSNR(dB)/SSIM values for visible band images ($K = 6$) at different L and input SNR values.	49
Table 4.1 ℓ_1 -norm based reconstruction algorithm for CSID	59
Table 4.2 ℓ_0 -norm based reconstruction algorithm for CSID	60
Table 4.3 Comparison of average PSNRs (dB) for different compressive measurement scenarios and SNRs.	63
Table 4.4 NMSE of the spectrum at the selected points.	65

Table 4.5 Comparison of average PSNRs (dB) for different priors, different compressive measurement scenarios, and SNRs. Prior results are given in the following SNR order: 20 dB, 30 dB, 40 dB. For a given CR and input SNR, priors with highest PSNR (within 0.1 dB margin) are given in bold numbers.	71
Table 4.6 Comparison of NMSE of the spectrum (in %) at the selected points for different priors and different compressive measurement scenarios when the input SNR is 30 dB. Prior results are given in the following point order: P1, P2, and P3. For a given CR and point, priors with lowest NMSE (within 0.1 % margin) are given in bold numbers.	71
Table 4.7 Comparison of average PSNRs (dB) for different compressive measurement scenarios and SNRs.	75
Table 4.8 Comparison of PSNRs (dB) of ℓ_0 -norm and ℓ_1 -norm based regularization methods for different compressive measurement scenarios and SNRs. Reconstruction results are given in the following SNR order: 20 dB, 30 dB, and infinite. For a given K and input SNR, methods with highest PSNR (within 0.1 dB margin) are given in bold numbers.	75
Table 4.9 Reconstruction times for different priors and input SNRs in seconds using ℓ_0 -norm based reconstruction method.	77
Table 4.10 PSNR(dB)/SSIM values of different datasets for different priors and different input SNRs.	77
Table 4.11 Different measurement plane selections normalized between f_{10} and f_1	87

LIST OF FIGURES

FIGURES

Figure 2.1	Schematic view of the diffractive lens based spectral imaging system	9
Figure 2.2	Measured intensities for 25 dB SNR at the first focal plane f_1 (a), at the second focal plane f_2 (e), and at the third focal plane f_3 (i), the underlying images of the first source at the first, second, and third focal planes (b)-(d), the underlying images of the second source at the first, second, and third focal planes (f)-(h), and the underlying images of the third source at the first, second, and third focal planes (j)-(l).	22
Figure 2.3	Sampled and zoomed point-spread functions of the system at the first focal plane for different wavelengths (a) λ_1 , (b) λ_2 , and (c) λ_3 , respectively.	23
Figure 2.4	Reconstructions of the first, second, and third sources at wavelengths λ_1 , λ_2 , and λ_3 (a), (c), (e) for 25 dB SNR and original diffraction-limited images of the sources (b), (d), (f), respectively.	24
Figure 2.5	Conditioning of the submatrices of \mathbf{H} for different number of point sources and different separation distances. Left to right: conditioning results when the point sources are placed at the first, second, and third spectral bands.	27
Figure 2.6	Demonstration of $5 \mu\text{m}$ resolution using point targets for 25 dB SNR. (a)-(c) Noisy measurements with 25 dB SNR at wavelengths λ_1 , λ_2 , and λ_3 , (d)-(f) reconstructed images from the noisy measurements, (g)-(i) diffraction-limited images, (j)-(l) ground truth images.	28

Figure 2.7	Reconstructed spectral images for different measurement SNRs when the FD measurement setting is used. Top to bottom: true spectral images, reconstructions with 60 dB, 40 dB, and 30 dB SNR.	29
Figure 3.1	Schematic view of the (a) PSSI (b) C-PSSI systems.	36
Figure 3.2	Reconstruction of EUV band images ($K = 2$) when input SNR is 30 dB. Left to right: Reference, Reconstruction when there is subsampling ($\Delta_x = \Delta_y = 2$), Reconstruction when there is no subsampling.	45
Figure 3.3	Reconstruction of visible band images ($K = 6$) when input SNR is 30 dB. Left to right: Reference, Reconstruction when there is subsampling ($\Delta_x = \Delta_y = 2$), Reconstruction when there is no subsampling.	46
Figure 3.4	Reconstruction of EUV band images ($K = 2$) when input SNR is 40 dB. Left to right: Reference, Reconstruction when there is severe subsampling ($\Delta_x = \Delta_y = 4$).	47
Figure 3.5	Reconstruction of visible band images ($K = 6$) when input SNR is 40 dB. Left to right: Reference, Reconstruction when there is severe subsampling ($\Delta_x = \Delta_y = 4$).	48
Figure 3.6	Reconstruction of visible band images ($K = 6$) when input SNR is 40 dB and $\Delta_x = \Delta_y = 4$. Left to right: Reference, Reconstruction when $L = 1$ (No coding-PSSI), $L = 2$, $L = 4$, $L = 8$, and $L = 16$	50
Figure 4.1	Illustration of the CSID system.	54
Figure 4.2	Demonstration of compressive measurements obtained with CSID. Left to right: Superimposed true image, sample mask pattern, sample compressive measurement.	62

Figure 4.3	Reconstructed spectral images (at 10 wavelengths in the range 530 – 620 nm with 10 nm spacing) from compressive measurements when input SNR is 30 dB. Left to right: true images, reconstructions with 50%, 60%, 70%, and 80% CR. Superimposed (summed) spectral cubes along the spectral dimension are shown at the bottom part.	64
Figure 4.4	Spectrum at three spatial positions P1, P2, and P3.	65
Figure 4.5	Reconstructed spectral images (at 10 wavelengths in the range 530 – 620 nm with 10 nm spacing) from compressive measurements using 3D TV prior when input SNR is 30 dB. Left to right: true images, reconstructions with 50%, 60%, 70%, and 80% CR.	67
Figure 4.6	Reconstructed spectral images (at 10 wavelengths in the range 530 – 620 nm with 10 nm spacing) from compressive measurements using 3D Full DCT prior when input SNR is 30 dB. Left to right: true images, reconstructions with 50%, 60%, 70%, and 80% CR.	68
Figure 4.7	Reconstructed spectral images (at 10 wavelengths in the range 530 – 620 nm with 10 nm spacing) from compressive measurements using 3D Patched DCT prior when input SNR is 30 dB. Left to right: true images, reconstructions with 50%, 60%, 70%, and 80% CR.	69
Figure 4.8	Reconstructed spectral images (at 10 wavelengths in the range 530 – 620 nm with 10 nm spacing) from compressive measurements using 2D Daub + 1D DCT prior when input SNR is 30 dB. Left to right: true images, reconstructions with 50%, 60%, 70%, and 80% CR.	70
Figure 4.9	(a) Reconstructed images from compressive measurements ($K = 2$). Top to bottom: true images, reconstructions with no mask, uncolored mask, colored mask. (b) PSNR versus K for the colored mask case	73
Figure 4.10	Spectral datasets with different spatial and spectral characteristics.	76

Figure 4.11	Reconstructed spectral images for dataset #1 when input SNR is 30 dB. Left to right: True images, 3D Patched DCT reconstruction, 3D Full DCT reconstruction.	78
Figure 4.12	Conditioning of the submatrices of HC for different number of point sources and different separation distances when CR is (a)-(d) 50%, 60%, 70%, and 80%, respectively. Left to right: conditioning results when the point sources are placed at the 1st, 5th, and 10th spectral bands.	80
Figure 4.13	Demonstration of 15 μm resolution using 16 point targets for 30 dB SNR. (a) Ground truth image , (b) diffraction-limited image, (c)-(f) reconstructed images from the noisy measurements when CR is 50%, 60%, 70%, and 80%.	82
Figure 4.14	Demonstration of 15 μm to 8 μm resolution using 16 point targets for 30 dB SNR when CR is 50%. (a)-(h) Reconstructed images from the noisy measurements when the separation distance is decreased from 15 μm to 8 μm with 1 μm steps.	83
Figure 4.15	Demonstration of 15 μm resolution using 16 point targets for different input SNRs when CR is 50%. (a)-(d) Reconstructed images from the noisy measurements when the input SNR is decreased from 30 dB to 0 dB with 10 dB steps.	84
Figure 4.16	Conditioning of the submatrices HC for 2 point sources placed at every $(i, i + 2)$ spectral pairs, $i = 1, \dots, 8$ when the CR values are 50%, 60%, 70%, and 80%, respectively.	85
Figure 4.17	Normalized 2500 largest singular values of HC matrix for the MP selections in Table 4.11. Zoomed-in version is given at right. . . .	87
Figure 4.18	(a) The ratio $\frac{\sigma_{min}}{\sigma_{max}}$ for different MP selections when input size is $32 \times 32 \times 10$. PSNRs for these MP selections when input SNR is 40 dB and input size is (b) $32 \times 32 \times 10$, (c) $64 \times 64 \times 10$, and (d) $256 \times 256 \times 10$, respectively.	89

LIST OF ABBREVIATIONS

1D	One Dimensional
2D	Two Dimensional
3D	Three Dimensional
ADMM	Alternating Direction Method of Multipliers
ALM	Augmented Lagrangian Method
CASSI	Coded Aperture Snapshot Spectral Imager
CCD	Charge-Coupled Device
CHISS	Compressive Hyperspectral Imaging by Separable and Spatial Operators
CS	Compressive Sensing
CMOS	Complementary Metal-Oxide-Semiconductor
CTIS	Computed Tomography Imaging Spectrometer
DCT	Discrete Cosine Transform
DDO	Discrete Derivative Operator
DFT	Discrete Fourier Transform
DMD	Digital Micro-Mirror Device
DOF	Depth of Focus
DWT	Discrete Wavelet Transform
EUV	Extreme Ultra-Violet
FFT	Fast Fourier Transform
FOV	Field of View
FPA	Focal Plane Array
IR	Infrared
LSI	Linear Shift Invariant

MAP	Maximum a Posteriori
NMSE	Normalized Mean Squared Error
OTF	Optical Transfer Function
PSF	Point Spread Function
PSNR	Peak Signal-to-Noise Ratio
PSSI	Photon Sieve Spectral Imaging
RGB	Red Green Blue
RMSE	Root Mean Squared Error
SLM	Spatial Light Modulator
SNR	Signal-to-Noise Ratio
SSIM	Structural Similarity Index Metric
TV	Total Variation
UV	Ultraviolet

CHAPTER 1

INTRODUCTION

Spectral imaging is a powerful diagnostic tool with application in diverse fields such as physics, chemistry, biology, medicine, astronomy, and remote sensing [1, 2]. The goal in spectral imaging is to form images of a scene as a function of wavelength. This requires simultaneous acquisition of three-dimensional (3D) data, $f(x, y, \lambda)$, for a two-dimensional (2D) scene, where λ is the spectral dimension and x and y are the spatial dimensions. Hence the spectral data cube contains the emitted spectrum for each spatial position.

However, capturing this 3D data with 2D detectors imposes inherent limitations on the spatio-spectral performance of the technique [3]. Conventional spectral imaging techniques rely on a scanning process to build up the 3D spectral cube from a series of 2D measurements. One approach uses a spectrometer with a long slit and scans the scene spatially. Hence, it records only a thin slice of the observed scene at a time. Another approach employs an imaging system with multiple spectral filters to scan the scene spectrally, which corresponds to imaging a single spectral band at a time.

One critical disadvantage of these techniques is that higher number of scans is needed with increased spatial and spectral resolutions [4]. This may lead to low light throughput, increased hardware complexity, and long acquisition times which cause temporal artifacts in dynamic scenes [5, 6]. Moreover, the temporal, spatial, and spectral resolutions are inherently limited as they are purely determined by the physical systems involved.

Computational spectral imaging is an effective approach to overcome these limitations by passing on some of the burden to an imaging algorithm. It enables to recon-

struct the entire spectral data cube from multiplexed measurements through computational techniques. One important theory exploited in computational spectral imaging is compressive sensing (CS) which relies on two principles: sparsity of the spectral images in some transform domain and incoherence of the measurements [7, 8]. It is widely known that spectral images exhibit both spatial and spectral correlations, which allow sparse representations. For the incoherence of the measurements, different optical configurations have been suggested [9, 10, 11, 12].

In this thesis, we develop novel computational spectral imaging techniques using CS theory and diffractive lenses. We focus on three important tasks in spectral imaging: fast and programmable multi-spectral imaging in Chapter 2, spatial super-resolution in Chapter 3, and compressive spectral imaging in Chapter 4. For each task, we first formulate the forward and inverse problems for the proposed imaging system. Then, we develop an alternating direction method of multipliers (ADMM) [13] based sparse recovery algorithm which enables fast and high quality reconstructions. Finally, the reconstruction performance is illustrated numerically for various settings. In all of the optical configurations, diffractive lenses are utilized.

For the fast and programmable multi-spectral imaging task, we first study a high-resolution computational imaging modality. This technique uses a diffractive lens such as a photon sieve for dispersing the optical field, and takes 2D measurements at different distances from the sieve using a moving detector. This system requires a mechanical component and is also undesirable in dynamic scenes. We present a modified version of this system which takes measurements at a fixed measurement plane by exploiting beam splitters or programmable spatial light modulators (SLM). We then develop an ADMM based fast sparse recovery method to solve the associated large-scale inverse problems for both modalities. Through simulations, we demonstrate that both modalities can be used interchangeably without sacrificing the reconstruction quality. Performance of the developed modalities are illustrated in extreme ultra-violet (EUV) and visible band. Moreover, we provide an analysis for the spatial resolution of the system using both theoretical and numerical tools.

We then turn our attention to the spatial super-resolution problem. Current spectral imaging systems, both computational imaging based and conventional ones, have

hardware and cost constraints which limit their spatial resolution. To overcome this limitation, we adopt a spatial super-resolution technique for the diffractive lens based spectral imaging system with a low-resolution detector. To reconstruct the spectral images with high spatial resolution from the subsampled measurements, we solve an inverse problem by developing an ADMM based reconstruction method. To achieve higher spatial super-resolution levels, we also extend this technique by adding a coded aperture to the imaging system. This aperture spatially modulates the optical field before dispersion to obtain more incoherent measurements, as dictated by CS theory. Multiple measurements with different spatial codes are captured to improve the measurement diversity. Effectiveness of the proposed super-resolution techniques is demonstrated numerically for different observation settings.

Lastly, we present a novel compressive spectral imaging technique named *compressive spectral imaging with diffractive lenses* (CSID). The CSID enables to reconstruct the entire spectral cube from a few multiplexed measurements via sparsity based reconstruction. It uses a coded aperture to spatially modulate the optical field from the scene and a diffractive lens such as a photon sieve for dispersion. Different than the spatial super-resolution setting, the coded aperture is fixed now, i.e. the same aperture is used for multiple measurements. Moreover, different than the earlier works that use diffractive lenses for spectral imaging [14, 15, 16], here we use them for the first time in a compressive modality. We develop sparse recovery methods with ℓ_1 -norm or ℓ_0 -norm based regularization to reconstruct the spectral cube from compressive measurements. We not only illustrate the imaging performance for various settings, but also investigate the effect of different sparsity priors on the reconstruction quality. In addition, a detailed analysis on the spatio-spectral resolution of the system and measurement optimization is provided using both analytical and numerical approaches.

The rest of this thesis is organized as follows. In Chapter 2, we present a modified version of a diffractive lens based computational multi-spectral imaging modality which offers fast, programmable, and high-resolution imaging. In Chapter 3, we apply spatial super-resolution to the imaging modality and extend its capability by adding a coded aperture to the system. In Chapter 4, we present a novel compressive spectral imaging modality using diffractive lenses, which reconstructs the entire data cube from few measurements. We provide the concluding remarks in Chapter 5.

CHAPTER 2

HIGH-RESOLUTION COMPUTATIONAL MULTI-SPECTRAL IMAGING USING DIFFRACTIVE LENSES

2.1 Introduction

Spectral imaging, the simultaneous imaging and spectroscopy of a radiating scene, is a fundamental diagnostic technique in the physical sciences with application in diverse fields such as physics, chemistry, biology, medicine, astronomy, and remote sensing. In this imaging modality, also known as imaging spectroscopy, multispectral or hyperspectral imaging, the intensity of the light radiated from each spatial point in the scene is sensed as a function of wavelength. The measured three-dimensional (3D) spectral data cube provides information for uniquely identifying the physical, chemical, and biological properties of targeted objects. This makes spectral imaging a useful diagnostic tool in various applications including remote sensing of astrophysical plasmas, environmental monitoring, resource management, biomedical diagnostics, industrial inspection, and surveillance, among many others.

Conventional spectral imaging techniques rely on a scanning process to build up the 3D spectral data cube from a series of 2D measurements that are acquired simultaneously, or sequentially. One important disadvantage of these conventional techniques is that the number of scans (hence measurements) proportionally increases with the desired spatial and spectral resolutions [4]. This disadvantage generally causes long acquisition times as well as hardware complexity. Resulting temporal artifacts in dy-

Some parts of this chapter have been recently presented in [17], and also submitted for publication [18].

dynamic scenes and low light throughput are other limitations [5, 6]. Moreover, since the conventional spectral imaging techniques purely rely on physical systems, there are inherent physical limitations on their performance such as temporal, spatial, and spectral resolutions.

To overcome these limitations, computational spectral imaging emerges as an effective approach by passing on some of the burden to a computational system. In these approaches, the 3D spectral cube is represented in terms of voxels and the voxel values are reconstructed from some indirect multiplexed measurements. The multiplexed measurements can be taken with different optical configurations. The added computational part provides flexibility to combine information from different measurements, as well as to incorporate the additional prior knowledge about the images of interest into the image formation process in the form of a regularization. This is achieved by solving an inverse problem for image reconstruction which takes into account both the image formation model and additional prior information.

Over the last decade, different techniques have been developed for computational spectral imaging. The most commonly known is coded aperture snapshot spectral imaging (CASSI) [10, 19, 20] which reconstructs the spectral cube by solving a computationally intensive inverse problem and also requires a bulky optical configuration involving a coded aperture, a prism, and lenses. Another method using the CASSI approach additionally performs mechanical translation to also encode temporal information [21]. Recently, diffractive lenses are also used to disperse the optical field in different configurations [22, 14, 15, 16]. Other techniques utilize a scattering medium [23] or an additional camera [24] to capture the multi-spectral data. A detailed review of these techniques are given in [25, 2].

Here we study a computational spectral imaging modality that uses a diffractive lens such as a photon sieve for dispersing the optical field. A photon sieve is a modification of a Fresnel zone plate in which open zones are replaced by a large number of circular holes. It has been proposed as a superior image forming device than the Fresnel zone plate [26], to be especially used at UV and x-ray wavelengths where refractive lenses are not available due to strong absorption of materials, and reflective mirrors are difficult to manufacture to achieve near diffraction-limited resolution. In fact, at

these shorter wavelengths, surface roughness and figure errors often limit resolution of reflective optics to a level that is significantly lower than the diffraction limit [27, 28, 29].

This computational spectral imaging modality was initially proposed in [22]. Because the focal length of a diffractive lens is wavelength-dependent, each measurement in this setting is the superposition of differently blurred spectral components. To achieve measurement diversity in this system, multiple measurements can be obtained in different ways. One possible approach is using a moving detector to capture measurements at different measurement planes, as in [22]. Alternatively, one can fix the measurement plane, i.e. the distance from the diffractive lens, and use different lens designs by exploiting beam splitters or programmable spatial light modulators (SLM). In both cases, each measurement consists of superimposed images of different wavelengths, with each spectral component being either in focus or out of focus. For incoherent illumination, we study the problem of recovering the individual spectral images from these superimposed and blurred data.

For this, we first formulate the discrete forward problem starting from the continuous image-formation model. The resulting inverse problem is an ill-posed multi-frame deconvolution problem requiring multiple images to be deblurred. This problem is formulated as a regularized least squares problem with sparsity prior. To solve the resulting problem, a fast reconstruction algorithm is developed using alternating direction method of multipliers (ADMM). Each update step in the algorithm has efficient computation, which enables significant savings on the computation time and memory.

In contrast to traditional multi-spectral imagers such as those employing wavelength filters, the proposed computational spectral imaging technique relies on a simple and low-cost optical system, but requires powerful image processing methods to form the spectral images computationally. In addition to the diffraction-limited high spatial resolution enabled by diffractive lenses in short wavelengths, this technique can also achieve higher spectral resolution than the conventional spectral imagers. This is because the proposed technique offers the possibility of separating nearby spectral components that would not otherwise be possible by using physical wavelength filters. These promising aspects are illustrated for EUV and visible bands through

numerical simulations. Finally, an analysis for spatial resolution is provided using both theoretical and numerical tools.

2.2 Forward Problem

2.2.1 Imaging System and Assumptions

The proposed spectral imaging system, illustrated in Fig. 2.1, obtains K different measurements. For the k th measurement, d_s and d_k respectively denote the distances from the object and measurement planes to the plane where the diffractive lens resides, where $k = 1, \dots, K$. To achieve measurement diversity in this system, multiple measurements can be obtained in different ways. One possible approach is using a moving detector to capture measurements at K different measurement planes. In this case, same diffractive lens can be used by only changing the distance d_k in each measurement. Alternatively, one can fix the measurement plane, i.e. the distance d_k , and use different diffractive lens designs by exploiting beam splitters or programmable spatial light modulators (SLMs) such as digital micromirror device (DMD). In this case, the focusing behavior of the diffractive lens can be changed in each measurement [17].

From the input object, we consider a polychromatic illumination consisting of P spatially incoherent monochromatic sources, each with a different wavelength λ_p where $p = 1, \dots, P$. These monochromatic sources are also assumed to be mutually incoherent [30]. In general, the diffractive lens can be used to form images either with spatially coherent or incoherent illumination [31]. In this work, we focus on the incoherent case where the diffractive lens produces images in intensity only, but the concepts readily generalize to the coherent or partially coherent case as well. The assumed illumination is typical in astrophysical imaging [29].

2.2.2 Continuous Image Formation Model

Our first goal is to mathematically relate the input spectral images, $f_{\lambda_p}(u, v)$, to the multiple measurements obtained. Each measurement is a superposition of differently

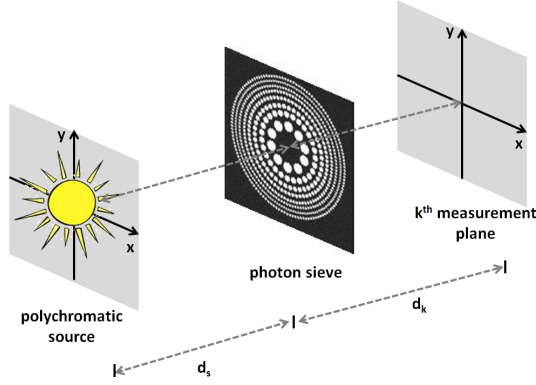


Figure 2.1: Schematic view of the diffractive lens based spectral imaging system

blurred spectral images. Mathematically, the intensity $t_k(u, v)$ of the k th measurement can be formulated [22] as

$$t_k(u, v) = \sum_{p=1}^P s_p(u, v) * g_{\lambda_p, k}(u, v), \quad (2.1)$$

where $*$ denotes the 2D continuous-time convolution operation. Here $s_p(u, v) = \frac{d_s^2}{d_k^2} f_{\lambda_p}(-\frac{d_s}{d_k}u, -\frac{d_s}{d_k}v)$ is a scaled version of the source intensity $f_{\lambda_p}(u, v)$ at the wavelength λ_p , and $g_{\lambda_p, k}(u, v)$ is the incoherent point-spread function (PSF) of the diffractive lens at wavelength λ_p for the k th measurement, given by [31]

$$g_{\lambda_p, k}(u, v) = \left| i \frac{\lambda_p}{\Delta_k} e^{-i\pi \frac{u^2+v^2}{\Delta_k \lambda_p d_k^2}} * A_k \left(\frac{u}{\lambda_p d_k}, \frac{v}{\lambda_p d_k} \right) \right|^2. \quad (2.2)$$

Here $\Delta_k = 1/d_s + 1/d_k$, and $A_k(u, v)$ is the Fourier transform of the aperture (transmittance) function of the diffractive lens used in the k th measurement. For classical diffractive lens designs with circular holes [26], $A_k(u, v)$ is sum of jinc functions corresponding to the Fourier transform of the circular functions representing each pinhole on the diffractive lens. It is defined as $\text{jinc}(u, v) = \frac{J_1(\pi\sqrt{u^2+v^2})}{2\sqrt{u^2+v^2}}$ where $J_1(u)$ is a Bessel function of the first kind.

An approximate, but a simpler model can also be used for the PSF in Eq. (2.2) when the number of zones in the diffractive lens design is large. This approximate PSF is

given as follows [31]:

$$g_{\lambda_p, k}(u, v) = \begin{cases} \left(\frac{1}{\pi} (\lambda_p d_k)^2 D_k^2 \text{jinc} \left(\frac{D_k}{\lambda_p d_k} u, \frac{D_k}{\lambda_p d_k} v \right) \right)^2, & \text{if } \epsilon_k = 0 \\ \left| \frac{1}{\pi} (\lambda_p d_k)^2 D_k^2 \text{jinc} \left(\frac{D_k}{\lambda_p d_k} u, \frac{D_k}{\lambda_p d_k} v \right) \right|^2, & \text{if } \epsilon_k \neq 0, \end{cases} \quad (2.3)$$

where D_k is the outer diameter of the diffractive lens, $f_1 = \frac{D_k w}{\lambda_p}$ is its first-order focal distance, w is the outer zone width of the diffractive lens, and $\epsilon_k = 1/d_k + 1/d_s - 1/f_1$ is a parameter related to the amount of defocusing. This approximate model provides easier computation as well as simpler analysis of the imaging system.

2.2.3 Discrete Model

In practice, only a finite number of discrete measurements is available through a digital sensor such as a CCD array. Since image reconstruction will be performed computationally on a digital computer, a discrete representation of the source intensities is also needed. Now, our goal is to obtain such a discrete-to-discrete model between the unknown spectral images and measurements.

For this, we exploit the band-limitedness of the continuous functions involved. First note that the PSF $g_{\lambda_p, k}$ is band-limited to a circle of diameter $2D_k/(\lambda_p d_k)$. This is because the argument inside the magnitude sign in (2.2) has a circular frequency support, whose diameter is $D_k/(\lambda_p d_k)$. The incoherent PSF is the magnitude square of this function, and hence the frequency support of this PSF is given by the convolution of this circular support with itself, resulting in a circular support of twice diameter [30]. The band-limitedness of the measurement t_k then directly follows from the band-limitedness of the PSF.

Secondly, note that high frequencies of the source images s_p that lie outside the frequency support of the PSF are not captured at the measurements, which is known as the inherent *diffraction-limit* [27]. As a result, the forward operator involving convolutions with these PSFs has a non-trivial nullspace. Here we restrict our attention to band-limited source images only, and aim for recovering the band-limited versions of

the source intensities s_p , which are given by

$$x_p(u, v) \equiv s_p(u, v) * \text{jinc} \left(\frac{2D_k}{\lambda_p d_k} u, \frac{2D_k}{\lambda_p d_k} v \right). \quad (2.4)$$

The forward model in (2.1) is still valid when the unknown source intensities, s_p , are replaced with their band-limited versions, x_p . Therefore, all functions in the continuous forward model can be assumed band-limited and represented using the conventional sinc basis [30].

Now by replacing each continuous band-limited function with its discrete representation with sinc basis, the continuous convolution operations in (2.1) reduce to discrete convolutions of the form [22]

$$t_k[m, n] = \sum_{p=1}^P x_p[m, n] * g_{\lambda_p, k}[m, n], \quad (2.5)$$

where $m, n = [0, \dots, N - 1]$. Here $t_k[m, n]$, $x_p[m, n]$, and $g_{\lambda_p, k}[m, n]$ are uniformly sampled versions of their continuous counterparts, e.g. $t_k[m, n] = t_k(m\Delta, n\Delta)$ for some Δ smaller than the Nyquist sampling interval (i.e. $\Delta < \frac{\lambda_p d_k}{2D_k}$). Here the uniformly sampled observations, $t_k[m, n]$, are assumed to be equal to the detector measurements, i.e. the averaged intensity over detector pixels of width Δ .

Let the PSF $g_{\lambda_p, k}[m, n]$ has $M \times M$ support, i.e. $g_{\lambda_p, k}[m, n] = 0$ for $m, n \notin [0, M - 1]$. We assume that the supports of the spectral images, $x_p[m, n]$, are limited to a slightly smaller region than the detector range as determined by N pixels in each direction, i.e. $x_p[m, n] = 0$ for $m, n \notin [0, N - M - 1]$. With this, the convolution in Eq. (2.5) can be replaced with a circular convolution of N points, which will be exploited in the development of the fast reconstruction method.

Due to the linearity of the circular convolution operator, the discrete model can be cast in matrix-vector form using appropriate lexicographic ordering:

$$\mathbf{t}_k = \sum_{p=1}^P \mathbf{H}_{k,p} \mathbf{x}_p \quad (2.6)$$

where $\mathbf{H}_{k,p}$ is an $N^2 \times N^2$ block circulant matrix with circular blocks corresponding to the circular convolution operation with the PSF $g_{\lambda_p, k}[m, n]$. Vectors \mathbf{t}_k and \mathbf{x}_p correspond to lexicographically ordered versions of observations, $t_k[m, n]$, and spectral images, $x_p[m, n]$, respectively. By combining all the measurement vectors into a

single vector, \mathbf{t} , we obtain

$$\mathbf{t} = \mathbf{H}\mathbf{x}, \quad (2.7)$$

$$\mathbf{H} = \begin{bmatrix} \mathbf{H}_{1,1} & \dots & \mathbf{H}_{1,P} \\ \vdots & & \vdots \\ \mathbf{H}_{K,1} & \dots & \mathbf{H}_{K,P} \end{bmatrix}, \quad (2.8)$$

where $\mathbf{t} = [\mathbf{t}_1^T | \dots | \mathbf{t}_K^T]^T$, $\mathbf{x} = [\mathbf{x}_1^T | \dots | \mathbf{x}_p^T]^T$, and \mathbf{H} is a $KN^2 \times PN^2$ matrix. In practice, the measurement \mathbf{t} is obtained in the presence of noise; hence the complete observation model can be expressed as

$$\mathbf{y} = \mathbf{t} + \mathbf{w} = \mathbf{H}\mathbf{x} + \mathbf{w} \quad (2.9)$$

where $\mathbf{w} = [\mathbf{w}_1^T | \dots | \mathbf{w}_K^T]^T$ is the additive noise vector. Here, white Gaussian noise is assumed, where $(\mathbf{w}_k)_i \sim N(0, \sigma_k^2)$ with σ_k representing the noise standard deviation for the k th measurement and uncorrelated across pixels i and different measurements k . This white Gaussian noise assumption is generally valid for many practical multi-spectral imaging scenarios of interest.

2.3 Inverse Problem

In the inverse problem, the goal is to recover the unknown spectral images, \mathbf{x} , from the measurements, \mathbf{y} , obtained with the spectral imaging system. This inverse problem can be considered as a multi-frame deconvolution problem that involves measurements of the superimposed blurred images. That is, each measurement is a superposition of focused or defocused versions of different spectral images. This deconvolution problem is inherently ill-posed, and as the PSFs, $g_{\lambda_p, k}[m, n]$, of different wavelengths and measurements become more similar (for example, as the distance between different measurement planes or different wavelengths decreases), the problem becomes more ill-conditioned due to the increased dependency between the columns of \mathbf{H} . Consequently, it becomes necessary to replace the original ill-posed problem with another inverse problem that has better conditioning.

There are a variety of approaches to solve ill-posed linear inverse problems. A systematic approach to regularization leads to the minimization of an appropriately for-

mulated cost function [32]. This approach generally derives from the use of prior knowledge about the unknown solution in a least squares setting. The prior information can be introduced in a deterministic way [33, 34, 35], or in a statistical setting [36], which is related to the Bayes paradigm [37].

A general formulation of the inverse problem can be expressed as

$$\min_{\mathbf{x}} \nu \|\mathbf{y} - \mathbf{H}\mathbf{x}\|_2^2 + \Phi(\mathbf{P}\mathbf{x}). \quad (2.10)$$

where the first term controls data fidelity, whereas the second term $\Phi(\mathbf{P}\mathbf{x})$ controls how well the reconstruction matches our prior knowledge of the solution, with the scalar parameter ν trading off between these two terms. \mathbf{P} is a matrix associated with an analysis (transform) operator. Equivalently, we can reformulate this problem as a constrained problem:

$$\min_{\mathbf{x}} \Phi(\mathbf{P}\mathbf{x}) \text{ subject to } \|\mathbf{y} - \mathbf{H}\mathbf{x}\|_2 \leq \epsilon, \quad (2.11)$$

where $\epsilon \geq 0$ is a parameter that depends on noise. We note that if the problem in Eq. (2.11) is feasible for some $\epsilon \geq 0$, then it is equivalent to Eq. (2.10) for some $\nu \geq 0$. An advantage of the formulation in Eq. (2.11) over Eq. (2.10) is the fact that the parameter ϵ is directly proportional to the noise standard deviation, hence it is much easier to choose than the parameter ν [38].

There are popular and powerful choices for the regularizer $\Phi(\cdot)$ [38, 39, 40]. One common choice is Tikhonov (quadratic) regularization [41], i.e. $\Phi(\mathbf{P}\mathbf{x}) = \|\mathbf{P}\mathbf{x}\|_2^2$ with an appropriately chosen regularization matrix \mathbf{P} (often a derivative operator), which leads to an optimization problem with a stable and closed-form solution. However, it generally results in a reconstruction that is globally smooth. This property is due to the fact that it treats all the structures of the image equally and to suppress noise, large gradients or edges are also penalized.

To avoid this and preserve sharp structures in reconstructions, quadratic regularization is often replaced with an ℓ_p -norm based regularization, i.e. $\Phi(\mathbf{P}\mathbf{x}) = \|\mathbf{P}\mathbf{x}\|_p^p$, with $1 \leq p < 2$. Unlike the quadratic case, when other norms are used, no closed-form solution exists and iterative methods are required. Of particular interest is the case when $p = 1$, leading to ℓ_1 -norm, which is convex but non-smooth (non-differentiable) in the origin, hence requires nonlinear optimization techniques. When a discrete approxi-

mation to the gradient operator is used for \mathbf{P} , the result is the well known anisotropic total variation (TV) regularization which has achieved significant popularity due to its superior results for reconstructing images with significant structure [42]. Another powerful choice is isotropic TV, i.e. $\Phi(\mathbf{P}\mathbf{x}) = \text{TV}(\mathbf{x})$ with $\mathbf{P} = \mathbf{I}$, defined as follows

$$\text{TV}(\mathbf{x}) = \sum_{m,n} \nabla(\mathbf{x})[m, n], \quad (2.12)$$

where

$$\nabla(\mathbf{x})[m, n] = \sqrt{(D_h(\mathbf{x}))^2 + (D_v(\mathbf{x}))^2}, \quad (2.13)$$

and

$$D_h(\mathbf{x}) = \mathbf{x}[m + 1, n] - \mathbf{x}[m, n], \quad (2.14)$$

$$D_v(\mathbf{x}) = \mathbf{x}[m, n + 1] - \mathbf{x}[m, n]. \quad (2.15)$$

This choice of regularization also preserves piecewise-constant characteristics of the image, but requires an iterative method for the solution [43].

2.4 Image Reconstruction Method

In this work, we develop a fast reconstruction algorithm using the ADMM framework to solve the resulting optimization problem in Eq. (2.11). ADMM is an algorithm used in many signal and image reconstruction problems [13, 44, 38, 45, 46]. It belongs to the family of augmented Lagrangian methods [47]. The algorithm provides a divide-and-conquer approach by splitting the minimization steps of the objective function in unconstrained multi-objective convex optimization problems. Its convergence has been guaranteed under mild conditions [13].

To solve the resulting problem, we first transform the problem in Eq. (2.11) to an unconstrained problem by adding the constraint to the objective as an indicator function:

$$\min_{\mathbf{x}} \Phi(\mathbf{P}\mathbf{x}) + \iota_{(\|\mathbf{y} - \mathbf{H}\mathbf{x}\|_2 \leq \epsilon)}(\mathbf{x}), \quad (2.16)$$

where the indicator function $\iota_{(\|\mathbf{y}-\mathbf{H}\mathbf{x}\|_2\leq\epsilon)}(\mathbf{x})$ is expressed as follows:

$$\iota_{(\|\mathbf{y}-\mathbf{H}\mathbf{x}\|_2\leq\epsilon)}(\mathbf{x}) = \begin{cases} 0, & \text{if } \|\mathbf{y} - \mathbf{H}\mathbf{x}\|_2 \leq \epsilon \\ +\infty, & \text{if } \|\mathbf{y} - \mathbf{H}\mathbf{x}\|_2 > \epsilon. \end{cases}$$

We then formulate our problem in ADMM form using variable-splitting:

$$\begin{aligned} & \underset{\mathbf{x}, \mathbf{u}, \mathbf{v}}{\text{minimize}} && \Phi(\mathbf{u}) + \iota_{(\|\mathbf{y}-\mathbf{v}\|_2\leq\epsilon)}(\mathbf{v}) \\ & \text{subject to} && \mathbf{u} = \mathbf{P}\mathbf{x}, \quad \mathbf{v} = \mathbf{H}\mathbf{x} \end{aligned} \quad (2.17)$$

where \mathbf{u} and \mathbf{v} are ADMM auxiliary variables. For the k th iteration, we have minimizations over \mathbf{x} , \mathbf{u} , and \mathbf{v} with the following ADMM update steps:

$$\mathbf{x}^{k+1} = \arg \min_{\mathbf{x}} \frac{\mu}{2} \left\| \begin{bmatrix} \mathbf{P} \\ \mathbf{H} \end{bmatrix} \mathbf{x} - \begin{bmatrix} \mathbf{u}^k \\ \mathbf{v}^k \end{bmatrix} - \begin{bmatrix} \mathbf{d}^k \\ \mathbf{f}^k \end{bmatrix} \right\|_2^2 \quad (2.18)$$

$$\mathbf{u}^{k+1} = \arg \min_{\mathbf{u}} \Phi(\mathbf{u}) + \frac{\mu}{2} \|\mathbf{u} - (\mathbf{P}\mathbf{x}^{k+1} - \mathbf{d}^k)\|_2^2 \quad (2.19)$$

$$\mathbf{v}^{k+1} = \arg \min_{\mathbf{v}} \iota_{(\|\mathbf{y}-\mathbf{v}\|_2\leq\epsilon)}(\mathbf{v}) + \frac{\mu}{2} \|\mathbf{v} - (\mathbf{H}\mathbf{x}^{k+1} - \mathbf{f}^k)\|_2^2 \quad (2.20)$$

where \mathbf{d} and \mathbf{f} are ADMM dual variables, and μ is a parameter related to the step size of the algorithm. We now explain how these update steps, referred as \mathbf{x} -update, \mathbf{u} -update, and \mathbf{v} -update, are performed.

In the \mathbf{x} -update step, we have a least squares problem, as given in Eq. (2.18), which has the following solution:

$$\mathbf{x}^{k+1} = (\mathbf{I} + \mathbf{H}^H\mathbf{H})^{-1}(\mathbf{P}^H(\mathbf{u}^k + \mathbf{d}^k) + \mathbf{H}^H(\mathbf{v}^k + \mathbf{f}^k)), \quad (2.21)$$

where we assume \mathbf{P} is a unitary transformation matrix satisfying $\mathbf{P}^H\mathbf{P} = \mathbf{I}$. Inversion of $(\mathbf{I} + \mathbf{H}^H\mathbf{H})$ can be pre-calculated and used throughout the iterations. However, since \mathbf{H} is a huge matrix, a direct inversion is not practical.

To overcome this issue, we develop an efficient technique to invert $\mathbf{A} \triangleq (\mathbf{I} + \mathbf{H}^H\mathbf{H})$ using ideas from [48]. Since each block of \mathbf{H} matrix, i.e. $\mathbf{H}_{k,p}$, is a block circulant matrix with circular blocks (BCCB), it is diagonalized by the discrete Fourier transform (DFT) matrix, \mathbf{F} . That is, $\mathbf{H}_{k,p} = \mathbf{F}^H \mathbf{\Lambda}_{k,p} \mathbf{F}$ where $\mathbf{\Lambda}_{k,p}$ is a diagonal matrix whose diagonal can be computed by taking the DFT of the first column of $\mathbf{H}_{k,p}$,

which corresponds to the PSF $g_{\lambda,p,k}[m, n]$. Let $\mathbf{\Lambda}$ be the matrix composed of $K \times P$ blocks with each block given by $\mathbf{\Lambda}_{k,p}$ for $k = 1, \dots, K$ and $p = 1, \dots, P$. Then \mathbf{A} is a matrix of $P \times P$ blocks with each block given by

$$\mathbf{A}_{p,q} = \sum_{k=1}^K \mathbf{H}_{k,p}^H \mathbf{H}_{k,p} + \delta_{p,q} \mathbf{I} = \mathbf{F}^H \mathbf{\Sigma}_{p,q} \mathbf{F}, \quad (2.22)$$

where $\mathbf{\Sigma}_{p,q} = \sum_{k=1}^K \mathbf{\Lambda}_{k,p}^H \mathbf{\Lambda}_{k,p} + \delta_{p,q} \mathbf{I}$ with $\delta_{p,q}$ being the Kronecker delta function and $p, q = 1, \dots, P$. Then \mathbf{A} can be written as $\mathbf{A} = \tilde{\mathbf{F}}^H \mathbf{\Sigma} \tilde{\mathbf{F}}$ where $\tilde{\mathbf{F}} = \mathbf{I}_P \otimes \mathbf{F}$, and \mathbf{I}_P is the $P \times P$ identity matrix. Here \otimes is the Kronecker product, and $\mathbf{\Sigma}$ is a matrix of $P \times P$ blocks with each block given by $\mathbf{\Sigma}_{p,q}$. Then the inverse of \mathbf{A} is given by $\tilde{\mathbf{F}}^H \mathbf{\Sigma}^{-1} \tilde{\mathbf{F}}$. Inserting this term in Eq. (2.21), we have the following solution for the \mathbf{x} -update step:

$$\mathbf{x}^{k+1} = \tilde{\mathbf{F}}^H \mathbf{\Sigma}^{-1} \tilde{\mathbf{F}} (\mathbf{P}^H (\mathbf{u}^k + \mathbf{d}^k) + \mathbf{H}^H (\mathbf{v}^k + \mathbf{f}^k)), \quad (2.23)$$

which can be rewritten as

$$\mathbf{x}^{k+1} = \tilde{\mathbf{F}}^H \mathbf{\Sigma}^{-1} (\tilde{\mathbf{F}} \mathbf{P}^H (\mathbf{u}^k + \mathbf{d}^k) + \mathbf{\Lambda}^H \tilde{\mathbf{F}} (\mathbf{v}^k + \mathbf{f}^k)). \quad (2.24)$$

Here we efficiently compute the terms $\tilde{\mathbf{F}} \mathbf{P}^H (\mathbf{u}^k + \mathbf{d}^k)$ and $\tilde{\mathbf{F}} (\mathbf{v}^k + \mathbf{f}^k)$ using the fast Fourier transform (FFT) since $\tilde{\mathbf{F}} (\mathbf{v}^k + \mathbf{f}^k) = [(\mathbf{F}(\mathbf{v}_1^k + \mathbf{f}_1^k))^T | \dots | (\mathbf{F}(\mathbf{v}_P^k + \mathbf{f}_P^k))^T]^T$ and a similar form for $\tilde{\mathbf{F}} \mathbf{P}^H (\mathbf{u}^k + \mathbf{d}^k)$.

For the efficient calculation of $\mathbf{\Sigma}^{-1}$, note that $\mathbf{\Sigma}$ is a block matrix of $P \times P$ blocks. Hence the inverse can be calculated efficiently through a recursive block matrix inversion approach [49]. For $P = 2$ case, this inverse becomes

$$\begin{bmatrix} \mathbf{\Sigma}_{1,1} & \mathbf{\Sigma}_{1,2} \\ \mathbf{\Sigma}_{2,1} & \mathbf{\Sigma}_{2,2} \end{bmatrix}^{-1} = \begin{bmatrix} \mathbf{C} & \mathbf{\Sigma}_{1,1}^{-1} \mathbf{\Sigma}_{1,2} \mathbf{K} \\ \mathbf{K} \mathbf{\Sigma}_{2,1} \mathbf{\Sigma}_{1,1}^{-1} & -\mathbf{K} \end{bmatrix} \quad (2.25)$$

where $\mathbf{K} = -(\mathbf{\Sigma}_{2,2} - \mathbf{\Sigma}_{2,1} \mathbf{\Sigma}_{1,1}^{-1} \mathbf{\Sigma}_{1,2})^{-1}$ and $\mathbf{C} = \mathbf{\Sigma}_{1,1}^{-1} - \mathbf{\Sigma}_{1,1}^{-1} \mathbf{\Sigma}_{1,2} \mathbf{K} \mathbf{\Sigma}_{2,1} \mathbf{\Sigma}_{1,1}^{-1}$. For $P > 2$ case, the overall matrix $\mathbf{\Sigma}$ is partitioned into 2×2 blocks and each block is inverted recursively using Eq. (2.25). Finally, we note that since each block in Eq. (2.25) is a diagonal matrix, this inversion requires only elementwise multiplication and division operations, which speeds up the computation significantly. Thus, it is not required to form any of the matrices involved. As mentioned before, $\mathbf{\Sigma}^{-1}$ is pre-calculated and used in all iterations for the \mathbf{x} -update step, as given in Eq. (2.24).

For the \mathbf{u} -update step, the minimization problem in Eq. (2.19) needs to be solved, which corresponds to a denoising problem of the form:

$$\Psi_f(\mathbf{u}) = \arg \min_{\mathbf{u}} f(\mathbf{u}) + \frac{1}{2} \|\mathbf{u} - \mathbf{z}\|_2^2, \quad (2.26)$$

where f is the regularization functional and \mathbf{z} is the noisy observation. The solution of this problem is defined as the Moreau proximal mapping [50] of the regularization function f evaluated at \mathbf{u} . Hence, the minimization in Eq. (2.19) is, by definition, the Moreau proximal mapping of $\Phi(\cdot)$ evaluated at $(\mathbf{P}\mathbf{x}^{k+1} - \mathbf{d}^k)$. We denote this proximal mapping as $\Psi_{\Phi}(\mathbf{P}\mathbf{x}^{k+1} - \mathbf{d}^k)$.

There are efficient calculations of $\Psi_{\Phi}(\mathbf{P}\mathbf{x}^{k+1} - \mathbf{d}^k)$ for different choices of $\Phi(\cdot)$ functional. For example, if ℓ_1 -norm is used, i.e. $\Phi(\mathbf{P}\mathbf{x}) = \|\mathbf{P}\mathbf{x}\|_1$, then $\Psi_{\Phi}(\mathbf{P}\mathbf{x}^{k+1} - \mathbf{d}^k)$ becomes soft-thresholding, i.e. $\Psi_{\ell_1} = \text{soft}(\mathbf{P}\mathbf{x}^{k+1} - \mathbf{d}^k, \tau)$, where τ is the thresholding parameter. The soft-thresholding, $\text{soft}(\mathbf{n}, \tau)$, is component-wise computed as $\mathbf{n}_l \rightarrow \text{sign}(\mathbf{n}_l) \max(|\mathbf{n}_l| - \tau, 0)$ for all l , with $\text{sign}(\mathbf{n}_l)$ taking value 1 if $\mathbf{n}_l > 0$ and -1 otherwise [38]. If $\Phi(\cdot)$ is chosen as isotropic TV operator, \mathbf{P} becomes the identity matrix, and the resulting proximal mapping, $\Psi_{\text{TV}}(\mathbf{x}^{k+1} - \mathbf{d}^k)$, has an efficient calculation for each spectral band using Chambolle's algorithm [43, 38]. Specifically, we separate the spectral bands and dual variables into P components, namely \mathbf{x}_p^{k+1} and \mathbf{d}_p^k , $p = 1, \dots, P$, and update each corresponding \mathbf{u}_p^{k+1} as follows:

$$\mathbf{u}_p^{k+1} = \Psi_{\text{TV}}(\mathbf{x}_p^{k+1} - \mathbf{d}_p^k), \quad p = 1, \dots, P. \quad (2.27)$$

Then, the overall vector \mathbf{u}^{k+1} is obtained by concatenating the \mathbf{u}_p^{k+1} vectors lexicographically.

For the \mathbf{v} -update step given in Eq. (2.20), similar to the \mathbf{u} -update, we have the proximal mapping of $\iota_{(\|\mathbf{y}-\mathbf{v}\|_2 \leq \epsilon)}(\cdot)$ evaluated at $(\mathbf{H}\mathbf{x}^{k+1} - \mathbf{f}^k)$, which we denote as $\Psi_{\iota_{(\|\mathbf{y}-\mathbf{v}\|_2 \leq \epsilon)}}(\mathbf{H}\mathbf{x}^{k+1} - \mathbf{f}^k)$. Calculation of this proximal mapping requires a projection of $\mathbf{s} \triangleq (\mathbf{H}\mathbf{x}^{k+1} - \mathbf{f}^k)$ onto ϵ -radius ball centered at \mathbf{y} . The solution has the following form [38]:

$$\Psi_{\iota_{(\|\mathbf{y}-\mathbf{v}\|_2 \leq \epsilon)}}(\mathbf{s}) = \begin{cases} \mathbf{y} + \epsilon \frac{\mathbf{s}-\mathbf{y}}{\|\mathbf{s}-\mathbf{y}\|_2}, & \text{if } \|\mathbf{s} - \mathbf{y}\|_2 > \epsilon \\ \mathbf{s}, & \text{if } \|\mathbf{s} - \mathbf{y}\|_2 \leq \epsilon. \end{cases} \quad (2.28)$$

Table 2.1: PSSI reconstruction algorithm

-
1. Set: $k = 0$
 Choose: $\mu > 0, \mathbf{u}^0, \mathbf{v}^0, \mathbf{d}^0, \mathbf{f}^0$
 2. **Repeat**
 3. $\mathbf{m}^k = \mathbf{P}^H(\mathbf{u}^k + \mathbf{d}^k) + \mathbf{H}^H(\mathbf{v}^k + \mathbf{f}^k)$
 4. $\mathbf{x}^{k+1} = (\mathbf{I} + \mathbf{H}^H\mathbf{H})^{-1}\mathbf{m}^k$
 5. $\mathbf{u}^{k+1} = \Psi_{\Phi}(\mathbf{P}\mathbf{x}^{k+1} - \mathbf{d}^k)$
 6. $\mathbf{v}_{k+1} = \Psi_{\iota_{(\|\mathbf{y}-\mathbf{v}\|_2 \leq \epsilon)}}(\mathbf{H}\mathbf{x}^{k+1} - \mathbf{f}^k)$
 7. $\mathbf{d}^{k+1} = \mathbf{d}^k - (\mathbf{P}\mathbf{x}^{k+1} - \mathbf{u}^{k+1})$
 8. $\mathbf{f}^{k+1} = \mathbf{f}^k - (\mathbf{H}\mathbf{x}^{k+1} - \mathbf{v}^{k+1})$
 9. $k \leftarrow k + 1$
 10. **Until:** some stopping criterion is satisfied.
-

Finally, ADMM dual variables, \mathbf{d} and \mathbf{f} , are updated as follows [13]:

$$\mathbf{d}^{k+1} = \mathbf{d}^k - (\mathbf{P}\mathbf{x}^{k+1} - \mathbf{u}^{k+1}) \quad (2.29)$$

$$\mathbf{f}^{k+1} = \mathbf{f}^k - (\mathbf{H}\mathbf{x}^{k+1} - \mathbf{v}^{k+1}) \quad (2.30)$$

The overall algorithm is summarized in Table 2.1 for a general \mathbf{P} and $\Phi(\cdot)$. In the numerical results, we choose $\Phi(\cdot)$ as the isotropic TV operator and step 5 is solved efficiently using Chambolle's algorithm [43] for each spectral band, as explained before.

2.4.1 Computational Complexity

The computational complexity of the algorithm is dominated by the \mathbf{x} -update, given in Steps 3 and 4 of Table 2.1. This requires $2P$ FFT and P inverse FFT computations. Thus, its computational complexity is $O(PN^2 \log(N))$ where N^2 is the size of a spectral image and P is the number of spectral bands. Proximal mapping in Step 5 and ADMM dual variable update in Step 7 have $O(N^2)$ complexity if \mathbf{P} is a diagonal matrix, or $O(PN^2 \log(N))$ if \mathbf{P} has a fast implementation such as with FFT. Step 6

and 8 require multiplication with \mathbf{H} , which costs $O(PN^2 \log(N))$. Thus, the overall complexity of the algorithm is $O(PN^2 \log(N))$. It is also worth noting that the complexity of the recursive inversion in Eq. (2.25) is $O(P^3 N^2)$. Since it is pre-calculated once, it does not affect the algorithm's overall complexity.

2.5 Numerical Results

Here we present numerical simulations to illustrate the high spatial and spectral resolution enabled by the proposed spectral imaging technique for an application in solar spectral imaging. For this, we consider a polychromatic input source generating three quasi-monochromatic waves at close (but different) EUV wavelengths: $\lambda_1 = 33.4$ nm, $\lambda_2 = 33.5$ nm and $\lambda_3 = 33.6$ nm (i.e., $P = 3$).

For the diffractive lens, a sample photon sieve design described in [29] for EUV solar imaging is considered, where the outer diameter of the sieve is 25 mm, and the diameter of the smallest hole is $5 \mu\text{m}$. This results in a photon sieve with the first-order focal lengths of $f_1 = 3.742$ m, $f_2 = 3.731$ m, and $f_3 = 3.720$ m at the corresponding wavelengths, and Abbe's diffraction resolution limit of $5 \mu\text{m}$ [27, 51]. The pixel size on the detector is then chosen as $2.5 \mu\text{m}$ to match the diffraction-limited resolution of the system with two pixels on the detector (which corresponds to Nyquist rate sampling).

For the imaging system, two different measurement settings are considered. In the *moving detector* (MD) case, the system records the intensities at three focal planes, f_1 , f_2 and f_3 , corresponding to wavelengths λ_1 , λ_2 and λ_3 (i.e., $K = 3$). Hence at the first focal plane, the measurement consists of a focused image of the first source overlapped with the defocused images of the second and the third sources, and vice versa at the other focal planes.

Alternatively, in the *fixed detector* (FD) case, we fix the measurement plane at the distance f_2 and obtain the measurements by changing the photon sieve diameter at each shot. This measurement setting obtains similar measurements with the MD setting without moving the detector in the axial direction, but at the expense of multiple photon sieve designs. In this case, the measurements can be obtained in real-time using a

spatial light modulator (SLM) to generate multiple photon sieves or beam-splitters.

For the FD setting, same photon sieve design is used by only changing the diameter to also focus λ_1 and λ_3 onto the distance f_2 . Because the measurement plane is fixed to $f_2 = 3.731$ m, the diameter is decreased by $77 \mu\text{m}$ for λ_1 and is increased by $72 \mu\text{m}$ for λ_3 . These modifications on the sieve design are within the limits of modern lithography techniques [52].

2.5.1 Reconstructions in EUV Band

Here we demonstrate the reconstructions of the solar spectral images under different imaging scenarios with MD and FD measurement settings. In the numerical experiments, solar EUV scenes of size 512×512 pixels are used as the inputs to the system. However, since the resolution of the existing solar spectral imagers are below the diffraction-limited resolution considered here, it is not possible to obtain a realistic (high-resolution) solar image for the simulations. Instead, we use these solar images as if they were images of some other sun-like object, and illustrate the diffraction-limited resolution for this case. Our goal with this experiment is to illustrate that diffraction-limited high spatial resolution can be achieved for imaging objects with similar characteristics.

Using the forward model in Eq. (2.9), we first simulate the measurements \mathbf{y} at the signal-to-noise ratio (SNR) of 25 dB for the MD setting. Figures 2.2 and 2.3 show the resulting measurements at the three focal planes together with the contributions from each source and the corresponding point-spread functions of the system, respectively. We obtain the reconstructions using the algorithm in Table 2.1 with isotropic TV regularization which is implemented in MATLAB. One reconstruction takes approximately 300 seconds on a computer with 16 GB of RAM and i7 7700K 4.20 GHz CPU.

The reconstructed images are shown in Fig. 2.4 for the three spectral sources, together with the diffraction-limited versions of the original scenes, for comparison. The reconstructed images suggest that the proposed system achieves near diffraction-limited resolution. The average peak SNR (PSNR) and SSIM values are 35.36 dB and 0.94,

respectively. Visual inspection shows that the characteristic features, such as solar flares, are successfully recovered from the noisy measurements.

In Table 2.2, we present the average PSNR and SSIM values for different SNRs of 15 dB to 40 dB with 5 dB steps, when MD and FD settings are used. The results demonstrate the successful and stable recovery under even noisy regimes. More specifically, the average PSNR is above 30 dB even when the input SNR is 15 dB. Furthermore, it increases significantly as the SNR level increases and surpasses 40 dB level for the highest SNR case. SSIM is 0.90 when input SNR is 20 dB, and increases up to 0.97 as the measurements become less noisy. Hence, the obtained PSNR and SSIM values clearly show the system’s powerful reconstruction capability over a wide range of noise levels, as required by various measurement scenarios.

Another critical observation in Table 2.2 is that MD and FD measurement settings almost provide the same reconstruction performance. For a given input SNR level, maximum differences in the reconstructions of the two settings are 0.18 dB for PSNR and 0.01 for SSIM metrics. This demonstrates that both measurement settings can be used interchangeably without sacrificing from the reconstruction performance. This opens up new possibilities for using both settings under different practical limitations.

To demonstrate the system performance for different number of multi-spectral bands, P , we also perform simulations for $P = 2$ and $P = 4$ cases as well while taking the number of measurements equal to the number of spectral bands (i.e. $K = P$). In the first setting, we consider two spectral bands at $\lambda_2 = 33.5$ nm, $\lambda_3 = 33.6$ nm with the measurements obtained at f_2 and f_3 . In the latter setting, we consider four spectral bands, namely $\lambda_0 = 33.3$ nm, $\lambda_1 = 33.4$ nm, $\lambda_2 = 33.5$ nm, $\lambda_3 = 33.6$ nm, and obtain four measurements at the corresponding focal planes, f_0 , f_1 , f_2 , and f_3 . Table 2.3 shows PSNR and SSIM values for these settings as well as $P = 3$ setting described before for comparison. The results demonstrate that the reconstruction quality degrades with increasing number of P values. This is expected as the inverse problem’s ill-posedness increases with the increase in the number of sources, P . Still, the system provides high quality reconstructions even for $P = 4$ case, with PSNR of 31.67 dB and SSIM of 0.90 for 25 dB input SNR.

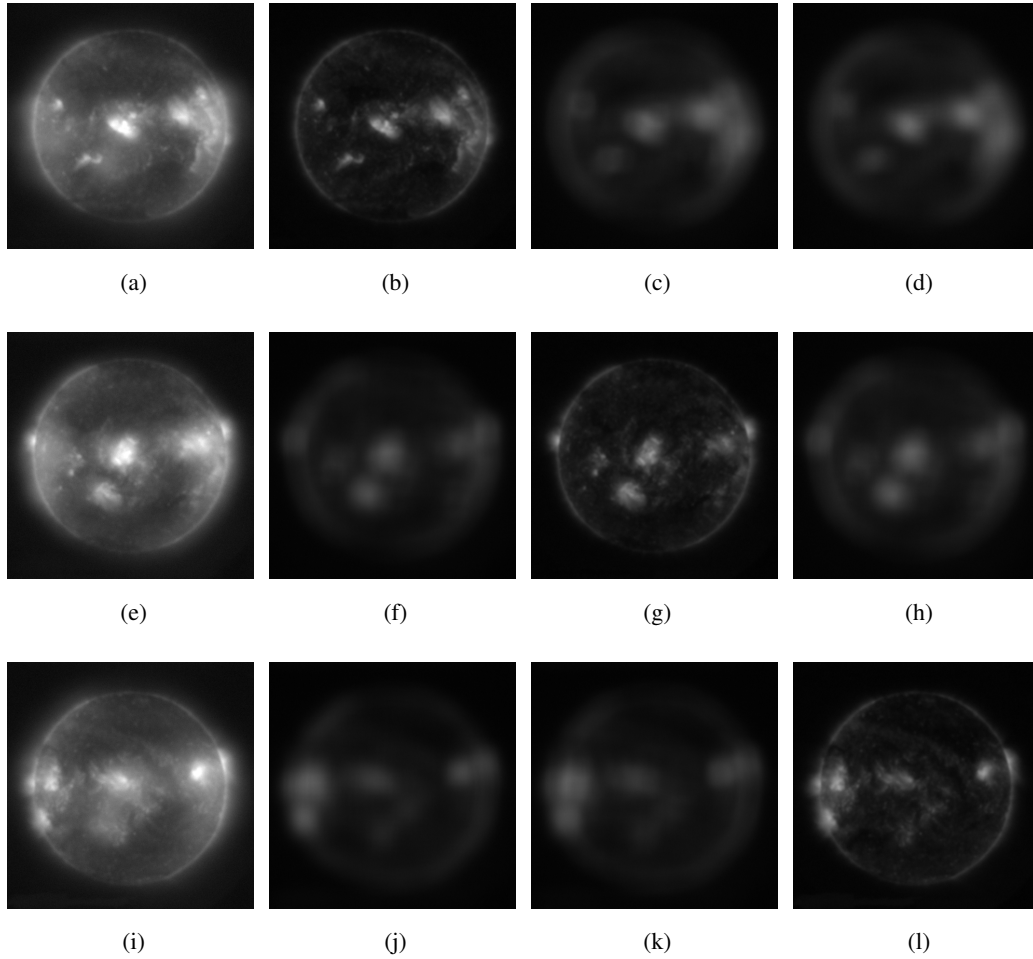
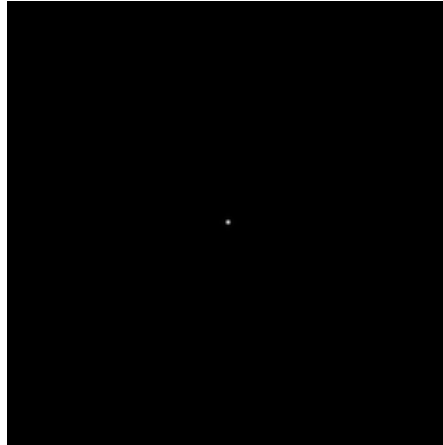
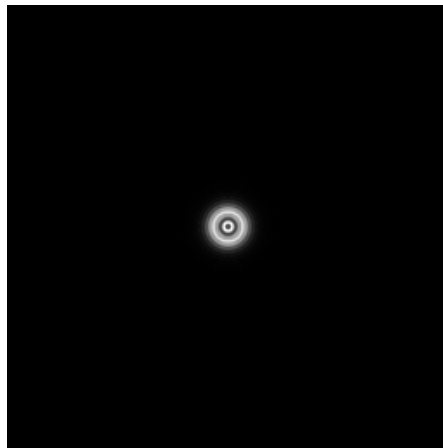


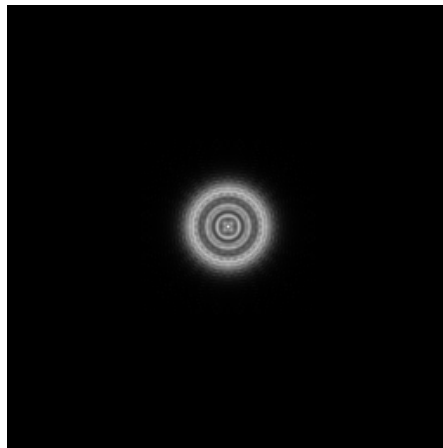
Figure 2.2: Measured intensities for 25 dB SNR at the first focal plane f_1 (a), at the second focal plane f_2 (e), and at the third focal plane f_3 (i), the underlying images of the first source at the first, second, and third focal planes (b)-(d), the underlying images of the second source at the first, second, and third focal planes (f)-(h), and the underlying images of the third source at the first, second, and third focal planes (j)-(l).



(a)



(b)



(c)

Figure 2.3: Sampled and zoomed point-spread functions of the system at the first focal plane for different wavelengths (a) λ_1 , (b) λ_2 , and (c) λ_3 , respectively.

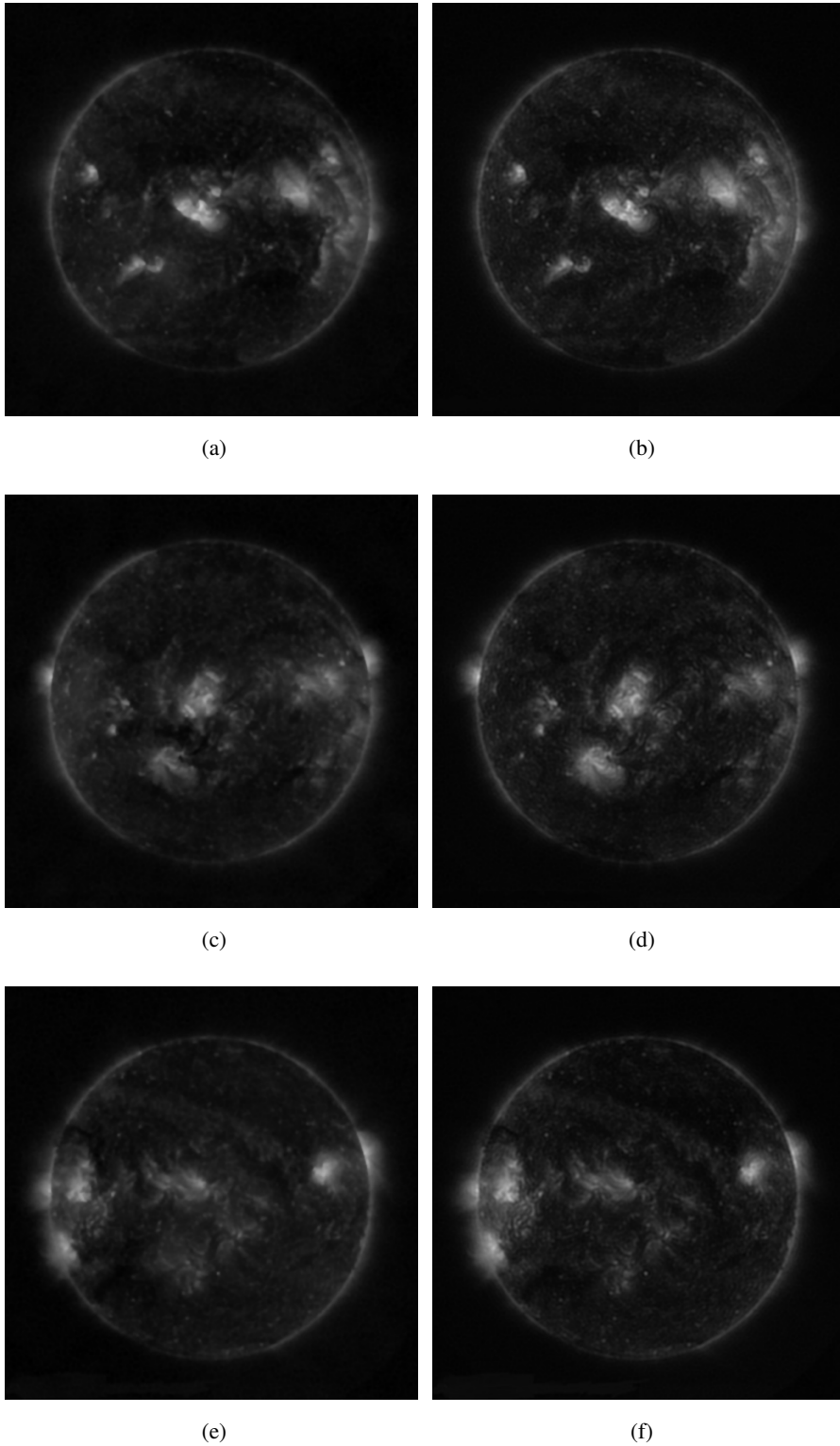


Figure 2.4: Reconstructions of the first, second, and third sources at wavelengths λ_1 , λ_2 , and λ_3 (a), (c), (e) for 25 dB SNR and original diffraction-limited images of the sources (b), (d), (f), respectively.

Table 2.2: PSNR (dB) and SSIM values for different input SNRs when *moving detector* (MD) and *fixed detector* (FD) measurement settings are used. SNR and PSNR values are reported in decibel (dB).

Input SNR	MD PSNR	FD PSNR	MD SSIM	FD SSIM
15	30.51	30.49	0.88	0.87
20	31.66	31.66	0.90	0.90
25	33.32	33.15	0.92	0.92
30	35.36	35.38	0.94	0.93
35	38.10	38.09	0.95	0.95
40	41.64	41.55	0.97	0.97

Table 2.3: PSNR (dB) and SSIM values for different number of sources (P) and measurements (K) for 25 dB SNR.

Setting	Average PSNR (dB)	Average SSIM
K=2, P=2	37.04	0.94
K=3, P=3	33.32	0.92
K=4, P=4	31.67	0.90

2.5.2 Resolution Analysis

In this section, we analyze the spatial resolution of the system both theoretically and numerically to understand its performance better. We first perform a conditioning-based analysis to demonstrate the resolution of the proposed system. Then, we reconstruct point sources with different separation distances from noisy measurements and

investigate whether they are in agreement with the conditioning-based analysis. Since this is not a conventional camera but a computational imaging system, two-point resolution may not reveal the system performance for more complex scenes. For this reason, in addition to two-point resolution, we also consider higher number of point sources.

For the theoretical analysis, similar to the analysis in [53], we investigate the stability of the forward model in Eq. (2.9). We consider different number of point sources with varying number of spacings between them. Since the measurements are corrupted by noise, conditioning of the columns of \mathbf{H} associated with the nonzero point sources will have a critical role on the reconstruction quality. Thus, by looking at the conditioning of the relevant submatrices of \mathbf{H} , we will gain an understanding about the resolving capability of the system. We suppose an oracle tells us the exact locations of the point sources on the 3D spectral data cube, which effectively corresponds to knowing the support of the cube a priori. Then, our job is to find only the values of the nonzero components. If this problem fails, the original problem of finding both nonzero locations and values will also fail. Hence calculating the conditioning of the relevant submatrices of \mathbf{H} provides insight for accurately solving the inverse problem of interest.

To perform this analysis, we consider point sources with 2, 4, 16, 36, and 64 elements placed in a square grid. We choose the pixel size on the detector as $1 \mu\text{m}$ for fine analysis of resolution. We change the spacing between the point sources from $1 \mu\text{m}$ to $20 \mu\text{m}$ with $1 \mu\text{m}$ steps. Then, we calculate the conditioning of corresponding submatrices for these point sources. The results are plotted in Fig. 2.5 when the point sources are located at the first, second and third spectral bands for $P = 3$ case in the MD measurement setting. As can be seen, conditioning is similar for all bands and becomes worse as the number of point sources increases, as expected. Moreover, as the point sources get closer, conditioning degrades which is also expected. This illustrates that the system is unable to resolve different point targets after a certain separation distance. An important observation is the rapid decrease in the condition number up to $5 \mu\text{m}$ separation distance which corresponds to the theoretical diffraction-limited resolution of the system for the monochromatic case. After this distance, the conditioning starts to change slowly for all cases.

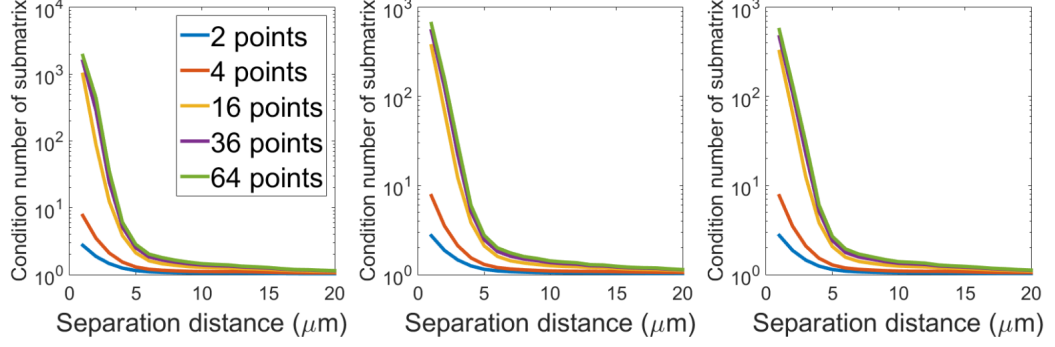


Figure 2.5: Conditioning of the submatrices of \mathbf{H} for different number of point sources and different separation distances. Left to right: conditioning results when the point sources are placed at the first, second, and third spectral bands.

For the numerical analysis of the system resolution, we consider 2, 4, and 16 point sources of size $1 \mu\text{m}$ placed at the first, second, and third spectral bands, respectively. The separation distance between the point sources are chosen as $5 \mu\text{m}$. The point sources are reconstructed from the measurements generated using the forward model in Eq. (2.9) for 25 dB SNR. Figure 2.6 shows the ground truth, diffraction-limited, and reconstructed point targets as well as the measured intensities. Visual inspection shows that the system successfully resolves points with $5 \mu\text{m}$ separation and reconstructs sharper images than the diffraction-limited images at this SNR level. We note that obtaining sharper reconstructions than the diffraction-limited images are also related with the choice of regularization, which is isotropic TV.

In another analysis, we observe that when the distance between the point sources are $5 \mu\text{m}$, we resolve them successfully even for 3 dB input SNR. This shows that the system resolution is robust for highly noisy measurements. Below this SNR level, reconstruction fails to separate the existing point sources. Moreover, resolving point sources with $4 \mu\text{m}$ spacing is also possible up to 5 dB input SNR. In other words, although it requires a higher SNR level than $5 \mu\text{m}$ case, the system is capable of providing $4 \mu\text{m}$ resolution for a wide range of SNR values. On the other hand, the system can not resolve the point sources when the distance becomes $3 \mu\text{m}$ even for high SNR levels. We expect that the system fails after a certain separation distance, as the conditioning degrades significantly below $5 \mu\text{m}$. Hence, these results are in

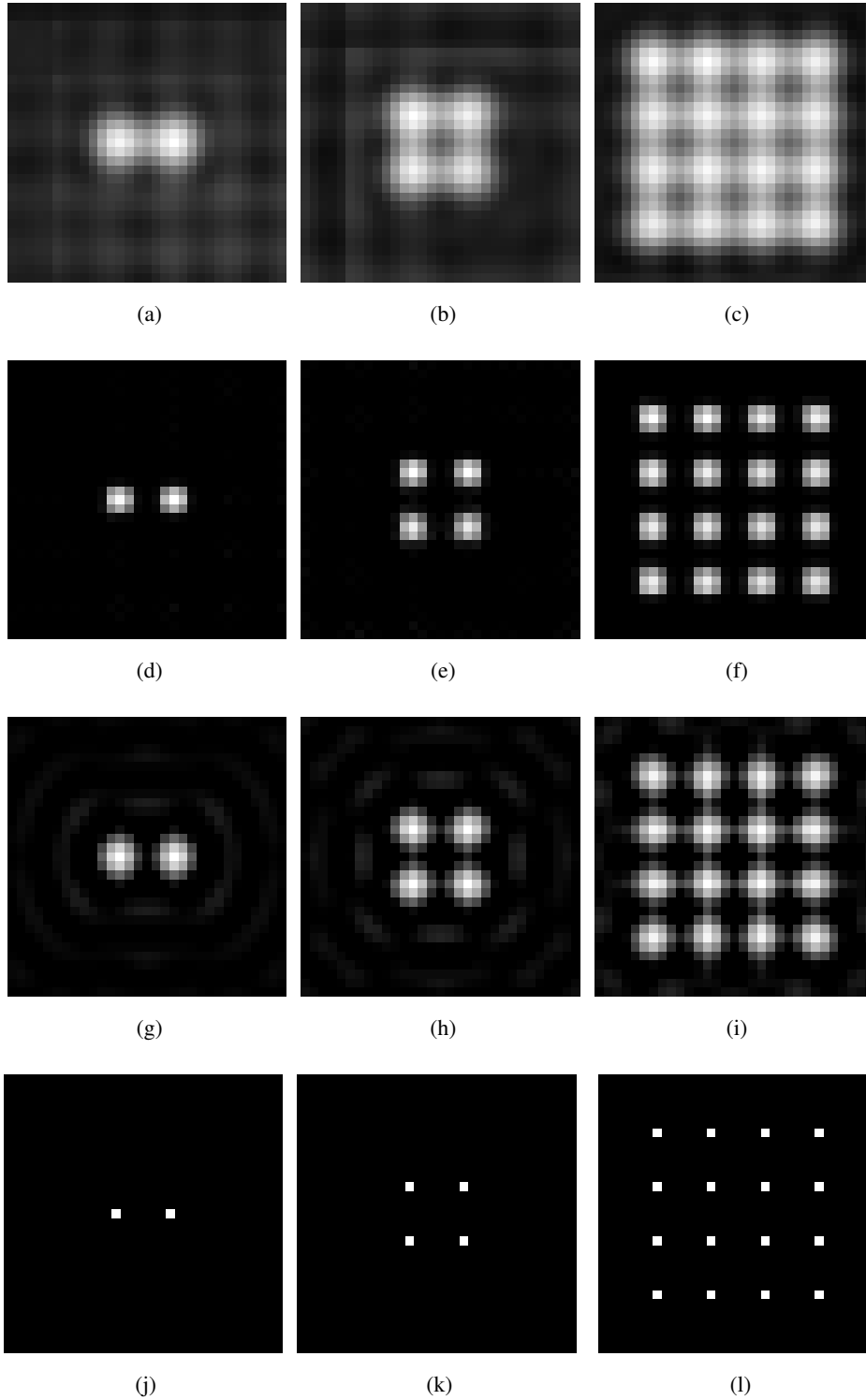


Figure 2.6: Demonstration of $5 \mu\text{m}$ resolution using point targets for 25 dB SNR. (a)-(c) Noisy measurements with 25 dB SNR at wavelengths λ_1 , λ_2 , and λ_3 , (d)-(f) reconstructed images from the noisy measurements, (g)-(i) diffraction-limited images, (j)-(l) ground truth images.

agreement with the conditioning plots shown in Fig. 2.5. Note that the intensity difference between the point sources would also affect their resolvability, which is not analyzed here.

2.5.3 Reconstructions in Visible Band

We now present numerical simulations to illustrate the performance of FD measurement setting in a visible band spectral imaging scenario. For this, we consider a dataset of size $256 \times 256 \times 10$ (10 wavelengths from 530–620 nm with 10 nm spacing) obtained from an online hyperspectral database at the University of Manchester [54]. For the photon sieve design, the smallest hole diameter is chosen as $\Delta = 15 \mu\text{m}$, which can be realized using an off-the-shelf digital micro-mirror device (DMD). The outer diameter of the sieve used for the k th measurement is selected as $D_k = \frac{f\lambda_k}{\Delta}$ [22] where the focal length f is fixed as 0.09 m. We simulate the measurements at the focal plane using the model in Eq. (2.9). The reconstruction algorithm is run on a computer with i7 7700K CPU and 16 GB RAM using MATLAB r2015a. Sparsity is enforced using a Kronecker basis $\mathbf{P} = \mathbf{P}_1 \otimes \mathbf{P}_2$, i.e. $\Phi(\mathbf{P}\mathbf{x}) = \|\mathbf{P}\mathbf{x}\|_1$ where \mathbf{P}_1 is the 2D Symmlet-8 basis and \mathbf{P}_2 is the 1D cosine basis [4]. This is a commonly used sparsity prior in computational spectral imaging.



Figure 2.7: Reconstructed spectral images for different measurement SNRs when the FD measurement setting is used. Top to bottom: true spectral images, reconstructions with 60 dB, 40 dB, and 30 dB SNR.

The number of measurements is chosen as $K = 10$ (i.e. non-compressive setting) and different SNR levels are considered. Table 2.4 shows the average PSNRs and SSIMs, and demonstrates successful reconstruction performance for moderate and high SNR cases. The reconstructed spectral images for 60 dB, 40 dB, and 30 dB SNR cases are shown in Fig. 2.7 together with the true images. The results illustrate that the visual quality and spectral characteristics are well preserved. Reconstruction times are approximately 200 seconds; thus the developed reconstruction method enables fast spectral imaging for higher number of spectral bands.

Table 2.4: Comparison of mean PSNRs (dB) and SSIMs for different SNR levels when the FD measurement setting is used.

Input SNR (dB)	20 dB	30 dB	40 dB	50 dB	60 dB	∞
Mean PSNR (dB) / SSIM	26.35/0.84	28.48/0.90	29.85/0.93	31.08/0.95	32.60/0.96	36.80/0.98

2.6 Conclusions

In this chapter, we have considered a diffractive lens based computational spectral imaging modality. This technique originally takes measurements at different distances from the sieve using a moving detector, which may be undesirable in dynamic scenes. To avoid this, we have proposed to take measurements at a fixed plane by using multiple photon sieves with beam splitters or programmable spatial light modulators (SLM). We have solved the resulting inverse problem by developing an ADMM based reconstruction technique. Efficient implementation of the proposed reconstruction technique has also been described, which requires no matrix formation and takes few minutes on a standard computer.

The presented results for EUV and visible band spectral imaging illustrate the possibility of achieving diffraction-limited spatial resolution and even beyond with the proposed computational spectral imaging technique. Another important advantage, which is slightly hidden in these experiments, is the higher spectral resolution achieved compared to the conventional spectral imagers with wavelength filters as pointed out in [22]. Note that the sources of interest in the EUV experiments have wavelengths

33.3 nm, 33.4 nm, 33.5 nm, and 33.6 nm, hence the proposed spectral imager can achieve a spectral resolution of 0.1 nm, which is less than 0.3% of the central wavelength of each source. Such a high spectral resolution is not possible to achieve with the state-of-the-art EUV wavelength filters, which can at best achieve a spectral resolution of 10% of the central wavelength [55]. This becomes an issue when this 10% spectral band contains more than one spectral line since in this case resolving each line is not possible.

Lastly, we have provided an analysis for the spatial resolution of the system both theoretically and numerically to understand its capability better. For this, we first performed a conditioning based analysis to understand the stability of the forward model. Then, we reconstructed point sources with different configurations and compared the results with the results of the conditioning analysis. The two results are in agreement and the system can provide the theoretically expected diffraction-limited spatial resolution and even beyond for a wide range of SNR levels. As a last remark, we note that these promising aspects of the technique can be improved further by taking more measurements than the unknown spectral bands (such as obtaining measurements at the intermediate planes), which will help to remedy the ill-posed nature of the encountered multi-frame deconvolution problem further.

CHAPTER 3

SPATIAL SUPER-RESOLUTION IN DIFFRACTIVE LENS BASED SPECTRAL IMAGING

3.1 Introduction

In this chapter, we consider the spatial super-resolution problem for spectral imaging systems with diffractive lenses. The spatial super-resolution problem aims to reconstruct the original high-resolution spectral images from low-resolution measurements. This problem is of interest in various practical imaging settings. Achieving high-spatial resolution is important for different spectral imaging applications involving space imagery, recognition and identification.

Current spectral imaging systems, both computational imaging based and conventional techniques, have hardware constraints which limit their spatial resolution. Although there is continuous interest and development in higher resolution focal plane arrays (FPAs) such as for infrared (IR) regime [56, 57], the associated costs still prohibit their use in low-cost applications [58]. To overcome these limitations, software-based (post-processing) approaches are proposed for spatial super-resolution problem [59, 60, 61, 62, 63, 64, 65, 66]. A better approach is to also modify the optical system based on the framework of computational imaging [58, 4, 67, 68]. Here, we develop spatial super-resolution techniques using both approaches for diffractive lens based spectral imaging. We utilize a photon sieve [22] as the diffractive lens, and call the resulting system photon sieve spectral imaging (PSSI).

Photon sieve is a modification of the Fresnel zone plate in which open zones are replaced by a large number of circular holes. It has superior performance in especially UV and x-ray wavelengths where refractive lenses are not available due to

strong absorption of materials, and reflective mirrors are difficult to manufacture to achieve diffraction-limited resolution [29]. It offers diffraction-limited imaging performance with relaxed manufacturing tolerances. However, because the focal length of the photon sieve is wavelength dependent (causing *chromatic aberration*), its use has been generally restricted to monochromatic sources[26, 69, 70]. The PSSI technique, however, takes advantage of chromatic aberration for multispectral imaging.

In the classical PSSI technique, as explained in Chapter 2, a moving detector is used to record the superimposed and differently blurred spectral images at different measurement planes (see Fig. 3.1). The spectral images are reconstructed from these measurements by solving a multi-frame deconvolution problem involving multiple objects. For super-resolution in PSSI, no hardware modification to the system is required. However, its super-resolution power is limited and the performance of the system degrades at higher subsampling levels. To overcome this issue, we also consider coded measurements by adding a coded aperture to the system and taking multiple shots with different coded masks. This system is called as Coded-PSSI (C-PSSI) (see Fig. 3.1).

Using the inverse problem framework, our aim is to reconstruct the original high-resolution spectral images from the measurements taken by a PSSI or C-PSSI system with a low-resolution detector. Although there are different algorithmic approaches for the spatial super-resolution problem in the literature, it is not possible to use them directly for the solution of our inverse problem. This is because our underlying problem involves blurry, superimposed and subsampled measurements. For this reason, we develop an algorithm to obtain fast and high quality reconstructions. The algorithm is based on alternating direction method of multipliers (ADMM) which is a frequently used optimization technique for linear inverse problems in imaging [38]. We analyze the performance of the algorithm for both PSSI and C-PSSI under different noise settings and obtain promising results in terms of reconstruction time and visual quality.

3.2 Forward Problem

Illustrations of PSSI and C-PSSI are given in Fig. 3.1. In PSSI, the optical field is directly passed through the photon sieve. On the other hand, in C-PSSI, the imaging lens forms the image of the scene on the plane of the coded aperture. The resulting coded field is then passed through the photon sieve. We consider PSSI and C-PSSI settings separately as the former has a limited super-resolution capability, but requires no hardware modification to the original system that takes measurements at different planes. The latter, on the other hand, utilizes a coded aperture and also takes multiple measurements at each plane with different codes to improve the performance. In both settings, we consider K different measurement planes. We discretize the original 3D spectral data cube into S spectral bands along the spectral dimension, and $N_x \times N_y$ pixels along the spatial dimensions. After this discretization, the spectral components have wavelengths $\lambda_1, \dots, \lambda_S$.

3.2.1 Photon Sieve Spectral Imaging (PSSI)

In PSSI, intensity measurements are recorded at K different measurement planes. In all K such measurement planes, we assume measurements are taken by a detector with a lower resolution than the expected theoretical resolution of the system. Here, d_s and d_k denote the distances from the source and k th measurement plane to the plane where the photon sieve resides, with $k = 1, \dots, K$. The relation between the k th measurement and the spectral images can be expressed as follows:

$$t_k[m, n] = \sum_{s=1}^S x_s[m, n] * h_{k,s}[m, n] \quad (3.1)$$

Here, the term $x_s[m, n]$ denotes the spectral image with wavelength λ_s . This spectral image at wavelength λ_s is convolved at distance d_k with the incoherent point-spread function (PSF), $h_{k,s}[m, n]$, of the photon sieve. This discretized PSF is obtained by uniformly sampling its continuous form, i.e. $g_{\lambda_s,k}[m, n] = g_{\lambda_s,k}(m\delta_x, n\delta_x)$ with δ_x denoting the spatial discretization distance. This sampling distance is chosen to match the diffraction-limited resolution of the system. Note that although the terms $x_s[m, n]$'s involve different scaling for different k 's, when d_s is much larger than d_k ,

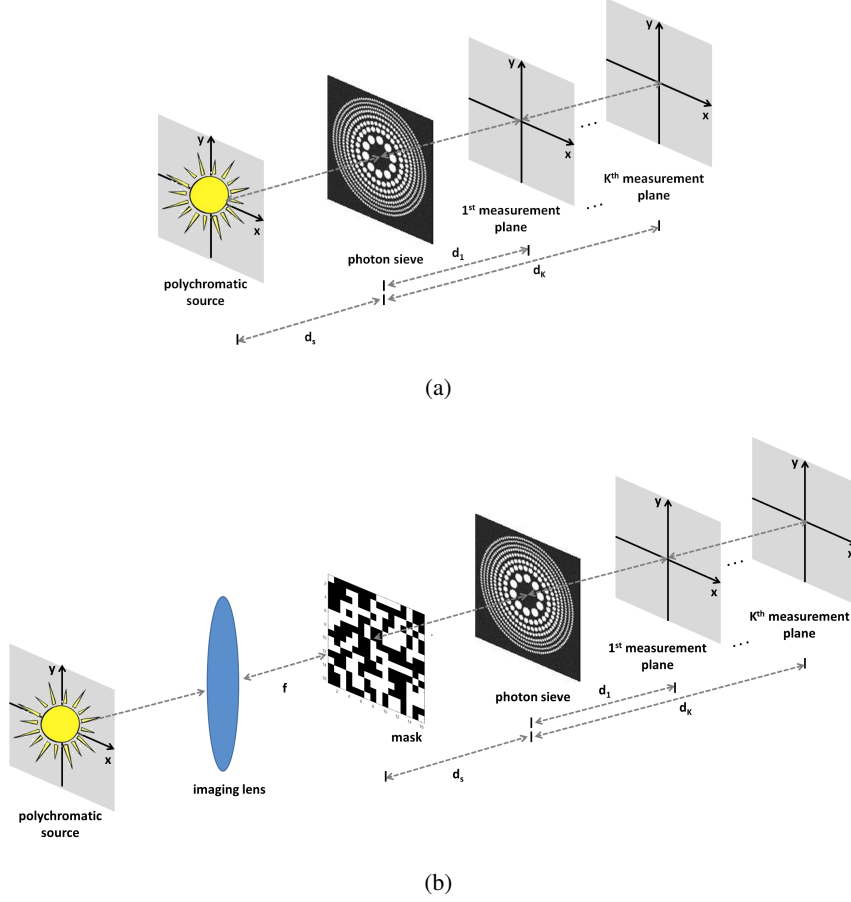


Figure 3.1: Schematic view of the (a) PSSI (b) C-PSSI systems.

this scaling can be effectively taken as the same. Hence, we assume all the spectral bands have the same scaling.

The continuous form of the PSF at wavelength λ_s and distance d_k has a closed-form expression given as [71]:

$$h_{k,s}(x, y) = i \frac{\lambda_s}{\gamma} e^{-i\pi \frac{x^2+y^2}{\Delta\lambda_s d_k^2}} * A\left(\frac{x}{\lambda_s d_k}, \frac{y}{\lambda_s d_k}\right), \quad (3.2)$$

where $\gamma = 1/d_s + 1/d_k$ and $A(f_x, f_y)$ is the Fourier transform of the aperture (transmission) function of the photon sieve. The aperture (transmission) function, $a(x, y)$, of the photon sieve is defined as the ratio of the transmitted field amplitude to the incident field amplitude at every point (x, y) on the photon sieve.

Because the detector has lower resolution than the resolution of the system, i.e. δ_x ,

the detector measurements are the subsampled versions of $t_k[m, n]$:

$$y_k[m, n] = \frac{1}{\Delta_x \Delta_y} \sum_{i_x=1}^{\Delta_x} \sum_{i_y=1}^{\Delta_y} t_k[(m-1)\Delta_x + i_x, (n-1)\Delta_y + i_y], \quad (3.3)$$

where $m = 1, \dots, N_x$ and $n = 1, \dots, N_y$ for an input image of size $N_x \times N_y$. Here, Δ_x and Δ_y denotes subsampling ratios along x and y dimensions, and $\Delta \triangleq \Delta_x \Delta_y$ is the overall subsampling ratio of the system. The measurement $y_k[m, n]$ is obtained at distance d_k over a detector with $N'_x \times N'_y$ pixels where $N'_x \triangleq \frac{N_x}{\Delta_x}$, $N'_y \triangleq \frac{N_y}{\Delta_y}$.

Here, we let the PSF $h_{k,s}[m, n]$ has $M \times M$ support, i.e. $h_{k,s}[m, n] = 0$ for $m, n \notin [1, M]$. We assume that the size of the input objects are limited to a slightly smaller region than the original image size, i.e. $x_s[m, n] = 0$ for $m \notin [M+1, N_x]$ and $n \notin [M+1, N_y]$. With this, the convolution in Eq. (3.1) can be replaced with a circular convolution of $N_x \times N_y$ points. This will be used later in the development of fast reconstruction algorithm.

We can rewrite the image formation model given in Eq. (3.3) in the following matrix-vector form:

$$\mathbf{y} = \mathbf{D}\mathbf{H}\mathbf{x} + \mathbf{w}, \quad (3.4)$$

$$\mathbf{y} = \begin{bmatrix} \mathbf{y}_1 \\ \vdots \\ \mathbf{y}_K \end{bmatrix}, \quad \mathbf{x} = \begin{bmatrix} \mathbf{x}_1 \\ \vdots \\ \mathbf{x}_S \end{bmatrix}, \quad \mathbf{H} = \begin{bmatrix} \mathbf{H}_{1,1} & \dots & \mathbf{H}_{1,S} \\ \vdots & & \vdots \\ \mathbf{H}_{K,1} & \dots & \mathbf{H}_{K,S} \end{bmatrix}.$$

Here, $\mathbf{y}_k \in R^{N'}$ represents the lexicographically ordered k th measurement vector, and $\mathbf{y} \in R^{KN'}$ is the overall measurement vector with $N' \triangleq N'_x N'_y$. Similarly, $\mathbf{x}_s \in R^N$ is the vector corresponding to the spectral image at wavelength λ_s , and $\mathbf{x} \in R^{SN}$ is the overall image vector with $N \triangleq N_x N_y$. The matrix $\mathbf{H}_{k,s} \in R^{N' \times N}$ is a block circulant matrix with circular blocks corresponding to circular convolution with $h_{k,s}[m, n]$, and $\mathbf{H} \in R^{KN' \times SN}$ is the overall system matrix. The matrix $\mathbf{D} \in R^{KN' \times KN}$ performs the averaging subsampling operation. It takes each $\Delta_x \times \Delta_y$ group and produces a single average for it. Using this matrix, integration of incoming light intensity over the low-resolution detector pixels is modeled [72]. Finally, the vector $\mathbf{w} = [w_1^T | \dots | w_K^T]^T$ is the additive white Gaussian noise with $(w_k)_i \sim N(0, \sigma_k^2)$.

3.2.2 Coded Photon Sieve Spectral Imaging (C-PSSI)

As illustrated in Fig. 3.1, C-PSSI system is similar to the PSSI system but there is an additional imaging lens and a coded aperture. The imaging lens forms the image of the scene on the plane of the coded aperture. We assume an ideal imaging lens with unit magnification. The resulting coded field is then passed through the photon sieve. These coded, superimposed and blurred measurements are captured using a low-resolution detector at different measurement planes. Similar to the PSSI, we assume d_s is much larger than d_k , hence different scaling ratios can be effectively taken as the same for all bands. We can take multiple measurements at each measurement plane by changing the code in the coded aperture (using a programmable spatial light modulator (SLM)) to obtain subpixel information about the spectral images. In this system, each different measurement can be expressed as follows:

$$t_{k,l}[m, n] = \sum_{s=1}^S (c_{l,s}[m, n] x_s[m, n]) * h_{k,s}[m, n], \quad (3.5)$$

where $c_{l,s}[m, n]$ denotes the l th coded aperture with entries 1 or 0 and modulates the s th spectral component. Each spectral component can be modulated differently, as in [73], using "colored" coded apertures. The other terms in the formulation is same with Eq. (3.1), and the same subsampling operation in Eq. (3.3) follows. Hence, we rewrite the given image-formation model in the matrix-vector form as follows:

$$\mathbf{y}_l = \mathbf{DHC}_l \mathbf{x} + \mathbf{w}_l, \quad (3.6)$$

where

$$\mathbf{C}_l = \begin{bmatrix} \text{diag}(c_{l,1}) & \dots & 0 \\ \vdots & \ddots & \vdots \\ 0 & \dots & \text{diag}(c_{l,s}) \end{bmatrix}$$

Here, different from Eq. (3.4), we have the diagonal matrix $\mathbf{C}_l \in R^{SN \times SN}$ corresponding to the l th coding operation for S different spectral components, and takes values 1 or 0 along its diagonal. If we consider taking L different measurements at each measurement plane with L different colored coded apertures, then the resulting relation becomes

$$\tilde{\mathbf{y}} = \tilde{\mathbf{D}}\tilde{\mathbf{H}}\tilde{\mathbf{C}}\mathbf{x} + \tilde{\mathbf{w}}, \quad (3.7)$$

where

$$\tilde{\mathbf{y}} = \begin{bmatrix} \mathbf{y}_1 \\ \vdots \\ \mathbf{y}_L \end{bmatrix}, \quad \tilde{\mathbf{D}} = \mathbf{D} \otimes \mathbf{I}_L, \quad \tilde{\mathbf{H}} = \mathbf{H} \otimes \mathbf{I}_L,$$

$$\tilde{\mathbf{C}} = \begin{bmatrix} \mathbf{C}_1 \\ \vdots \\ \mathbf{C}_L \end{bmatrix}, \quad \tilde{\mathbf{w}} = \begin{bmatrix} \mathbf{w}_1 \\ \vdots \\ \mathbf{w}_L \end{bmatrix}.$$

Here, $\tilde{\mathbf{y}} \in R^{LKN'}$ is the overall measurement vector, and $\tilde{\mathbf{C}} \in R^{LSN \times SN}$ represents the coding operation with L different colored coded apertures. The matrix \mathbf{I}_L is $L \times L$ identity matrix and \otimes denotes Kronecker product. The block diagonal matrices $\tilde{\mathbf{H}} \in R^{LKN \times LSN}$ and $\tilde{\mathbf{D}} \in R^{LKN' \times LKN}$ performs convolution and averaging subsampling operations for different colored coded apertures, respectively. Finally, $\tilde{\mathbf{w}} \in R^{LKN'}$ is the overall additive white Gaussian noise vector. We note that this formulation reduces to (3.4) if we set $L = 1$ and \mathbf{C} to identity matrix. Hence, from now on, we use the more general forward model in Eq. (3.7).

3.3 Inverse Problem

In the inverse problem, the goal is to reconstruct the unknown spectral images, \mathbf{x} , from their noisy, superimposed, blurred, coded, and subsampled measurements, $\tilde{\mathbf{y}}$. This problem is inherently ill-posed due to subsampling and blurring operations. Decreasing the detector resolution and distance between different measurement planes, and the different wavelengths further increase the ill-posedness of the problem.

There are a variety of approaches to solving such ill-posed linear inverse problems [74]. Here we consider using the prior knowledge of the unknown solution in a least squares setting. This results in the following regularized linear least squares problem:

$$\min_{\mathbf{x}} \nu \|\tilde{\mathbf{y}} - \tilde{\mathbf{D}}\tilde{\mathbf{H}}\tilde{\mathbf{C}}\mathbf{x}\|_2^2 + \mathcal{R}(\mathbf{x}). \quad (3.8)$$

Here the first term controls data fidelity, whereas the second term $\mathcal{R}(\mathbf{x})$ controls how well the reconstruction matches our prior knowledge of the solution, with the scalar

parameter ν trading off between these two terms. Equivalently, we can reformulate this problem as a constrained problem:

$$\min_{\mathbf{x}} \mathcal{R}(\mathbf{x}) \text{ subject to } \|\tilde{\mathbf{y}} - \tilde{\mathbf{D}}\tilde{\mathbf{H}}\tilde{\mathbf{C}}\mathbf{x}\|_2 \leq \epsilon, \quad (3.9)$$

where $\epsilon \geq 0$ is a parameter that depends on noise variance. We note that if problem (3.9) is feasible for some $\epsilon \geq 0$, then it is equivalent to (3.8) for some $\nu \geq 0$. An advantage of the formulation (3.9) over (3.8) is the fact that the parameter ϵ is directly proportional to the noise standard deviation, hence it is much easier to set than ν [38].

There are popular and powerful choices for the regularizer $\mathcal{R}(\cdot)$ such as those involving ℓ_1 -norm and total variation (TV) [38]. We choose $\mathcal{R}(\cdot)$ as anisotropic 3D TV operator when the spectrum has high correlation along the spectral dimension, i.e. slowly changing, to exploit the redundancy. If the spectrum has small correlation, i.e. fast changing, along the spectral dimension, then we use anisotropic 2D TV operator since redundancy in the spectral dimension is limited. Specifically,

$$\text{2D TV: } \mathcal{R}(\mathbf{x}) = \|\mathbf{T}_x\mathbf{x}\|_1 + \|\mathbf{T}_y\mathbf{x}\|_1 \triangleq TV_{2D}(\mathbf{x}) \quad (3.10)$$

$$\text{3D TV: } \mathcal{R}(\mathbf{x}) = TV_{2D}(\mathbf{x}) + \|\mathbf{T}_z\mathbf{x}\|_1 \triangleq TV_{3D}(\mathbf{x}) \quad (3.11)$$

Here $\mathbf{T}_x, \mathbf{T}_y, \mathbf{T}_z$ are $SN \times SN$ matrices performing the discrete derivative operation along x, y, and z dimensions.

3.4 Image Reconstruction Method

Similar to Chapter 2, we solve the resulting optimization problem in (3.9) by developing a fast reconstruction algorithm using ADMM framework. Again, we rewrite (3.9) in ADMM formulation. For this, we first convert the problem to an unconstrained problem by adding the constraint to the objective as an indicator function:

$$\min_{\mathbf{x}} \mathcal{R}(\mathbf{x}) + \iota_{(\|\tilde{\mathbf{y}} - \tilde{\mathbf{D}}\tilde{\mathbf{H}}\tilde{\mathbf{C}}\mathbf{x}\|_2 \leq \epsilon)}(\mathbf{x}), \quad (3.12)$$

where the indicator function $\iota_{(\|\tilde{\mathbf{y}} - \tilde{\mathbf{D}}\tilde{\mathbf{H}}\tilde{\mathbf{C}}\mathbf{x}\|_2 \leq \epsilon)}(\mathbf{x})$ has the following form:

$$\iota_{(\|\tilde{\mathbf{y}} - \tilde{\mathbf{D}}\tilde{\mathbf{H}}\tilde{\mathbf{C}}\mathbf{x}\|_2 \leq \epsilon)}(\mathbf{x}) = \begin{cases} 0, & \text{if } \|\tilde{\mathbf{y}} - \tilde{\mathbf{D}}\tilde{\mathbf{H}}\tilde{\mathbf{C}}\mathbf{x}\|_2 \leq \epsilon \\ +\infty, & \text{if } \|\tilde{\mathbf{y}} - \tilde{\mathbf{D}}\tilde{\mathbf{H}}\tilde{\mathbf{C}}\mathbf{x}\|_2 > \epsilon. \end{cases}$$

We then obtain the following formulation of the problem in ADMM form:

$$\begin{aligned} & \underset{\mathbf{x}, \mathbf{u}, \mathbf{v}}{\text{minimize}} && \mathcal{R}(\mathbf{u}) + \iota_{(\|\tilde{\mathbf{y}} - \mathbf{v}\|_2 \leq \epsilon)}(\mathbf{v}) \\ & \text{subject to} && \mathbf{u} = \mathbf{x}, \quad \mathbf{v} = \tilde{\mathbf{D}}\tilde{\mathbf{H}}\tilde{\mathbf{C}}\mathbf{x} \end{aligned} \quad (3.13)$$

where \mathbf{u} and \mathbf{v} are ADMM auxiliary variables. After this formulation, we minimize the variables \mathbf{x} , \mathbf{u} , and \mathbf{v} alternately, as explained below.

In \mathbf{x} -update step, we have a least squares problem which has the following normal equation:

$$(\mathbf{I} + \tilde{\mathbf{C}}^H \tilde{\mathbf{H}}^H \tilde{\mathbf{D}}^H \tilde{\mathbf{D}} \tilde{\mathbf{H}} \tilde{\mathbf{C}}) \mathbf{x}^{k+1} = (\mathbf{u}^k + \mathbf{d}^k) + \tilde{\mathbf{C}}^H \tilde{\mathbf{H}}^H \tilde{\mathbf{D}}^H (\mathbf{v}^k + \mathbf{f}^k) \quad (3.14)$$

where \mathbf{d} and \mathbf{f} are ADMM dual variables. We solve this normal equation for \mathbf{x}^{k+1} using a conjugate-gradient algorithm, which reaches convergence in a few iterations. For this iterative process, forming any of the matrices is not required, which provides significant savings for the memory as well as the computation time. Specifically, multiplications with matrices $\tilde{\mathbf{H}}$ and $\tilde{\mathbf{H}}^H$ correspond to summation of some convolutions. That is, for multiplication with $\tilde{\mathbf{H}}$ matrix, we can simply take 2D Fourier transforms of underlying PSFs $h_{k,1}[m, n], \dots, h_{k,S}[m, n]$ and the spectral images $x_1[m, n], \dots, x_S[m, n]$, multiplying them elementwise, and then summing all the results. For multiplication with $\tilde{\mathbf{H}}^H$ matrix, a similar operation is performed using $h_{1,s}[m, n], \dots, h_{K,s}[m, n]$. Multiplications with $\tilde{\mathbf{D}}$ and $\tilde{\mathbf{D}}^H$ can be carried out using averaging subsampling operator and zero-order hold interpolating operator, respectively. Former is computed by taking each $\Delta_x \times \Delta_y$ group and producing a single average for it. For the latter, each single entry of the image is repeated in a $\Delta_x \times \Delta_y$ block. Lastly, the required multiplications with $\tilde{\mathbf{C}}$ and $\tilde{\mathbf{C}}^H$ in the iterative process reduce to simple elementwise multiplications with coded aperture functions. Hence, forming these large matrices is also not required.

In \mathbf{u} -update, the following minimization problem is solved:

$$\mathbf{u}^{k+1} = \arg \min_{\mathbf{u}} \mathcal{R}(\mathbf{u}) + \frac{\mu}{2} \|\mathbf{u} - (\mathbf{x}^{k+1} - \mathbf{d}^k)\|_2^2 \quad (3.15)$$

We make a quadratic approximation to the ℓ_1 -norms in $\mathcal{R}(\mathbf{u})$ term using half-quadratic regularization for an overall quadratic formulation [75]. Although the underlying operators are different in anisotropic 2D and 3D TV cases, the solution is obtained for

both cases using the following normal equation:

$$\left(\frac{\mu}{2}\mathbf{I} + \mathbf{T}^T\mathbf{W}\mathbf{T}\right)\mathbf{u}^{k+1} = \frac{\mu}{2}(\mathbf{x}^{k+1} - \mathbf{d}^k) \quad (3.16)$$

Here, \mathbf{T} is the matrix performing TV_{2D} or TV_{3D} operations depending on the spectrum of interest. \mathbf{W} is a diagonal weighting matrix due to approximating ℓ_1 -norm using half-quadratic regularization [76, 75]. It has the following form:

$$\mathbf{W} = \text{diag}\left(\frac{0.5}{([\mathbf{T}\mathbf{u}]_i^2 + \beta)^{0.5}}\right), \quad (3.17)$$

where β is a small positive constant.

The given normal equation is solved for \mathbf{u}^{k+1} using a conjugate-gradient algorithm, which converges in a few iterations. Multiplication with \mathbf{T} matrix can be carried out performing convolutions with difference filter, i.e. $[1 \ -1 \ 0]$, along x , y , and z directions. Similarly, the flipped version of the difference filter can be used for multiplication with \mathbf{T}^H matrix. Hence, forming these matrices is not required as well.

Minimization of \mathbf{v} requires a projection of $\mathbf{s} \triangleq (\tilde{\mathbf{D}}\tilde{\mathbf{H}}\tilde{\mathbf{C}}\mathbf{x}^{k+1} - \mathbf{f}^k)$ onto ϵ -radius ball centered at $\tilde{\mathbf{y}}$. The solution has the following form:

$$\mathbf{v}^{k+1} = \begin{cases} \tilde{\mathbf{y}} + \epsilon \frac{\mathbf{s} - \tilde{\mathbf{y}}}{\|\mathbf{s} - \tilde{\mathbf{y}}\|_2}, & \text{if } \|\mathbf{s} - \tilde{\mathbf{y}}\|_2 > \epsilon \\ \mathbf{s}, & \text{if } \|\mathbf{s} - \tilde{\mathbf{y}}\|_2 \leq \epsilon. \end{cases} \quad (3.18)$$

Finally, we update ADMM dual variables as follows:

$$\mathbf{d}^{k+1} = \mathbf{d}^k - (\mathbf{x}^{k+1} - \mathbf{u}^{k+1}) \quad (3.19)$$

$$\mathbf{f}^{k+1} = \mathbf{f}^k - (\tilde{\mathbf{D}}\tilde{\mathbf{H}}\tilde{\mathbf{C}}\mathbf{x}^{k+1} - \mathbf{v}^{k+1}) \quad (3.20)$$

The overall algorithm is given in Table 3.1.

3.4.1 Computational Complexity

Dual variable updates in Steps 7 and 8 have $O(LSN)$ cost. $\tilde{\mathbf{D}}$, $\tilde{\mathbf{D}}^H$, $\tilde{\mathbf{C}}$, $\tilde{\mathbf{C}}^H$ operations and the Moreau proximal mappings in Steps 5-6 have cost $O(LSN)$ as well. Hence, the complexity of the overall algorithm is $O(LSN \log(N))$ due to FFT algorithm used for multiplications with $\tilde{\mathbf{H}}$ and $\tilde{\mathbf{H}}^H$.

Table 3.1: Spatial super-resolution in PSSI algorithm

1. Set: $k = 0$
 Choose: $\mu > 0$, \mathbf{u}_0 , \mathbf{v}_0 , \mathbf{d}_0 , \mathbf{f}_0 .
2. **Repeat**
3. Solve Eq. (3.14) for \mathbf{x}^{k+1} using conjugate-gradient algorithm.
4. Solve Eq. (4.8) for \mathbf{u}^{k+1} using conjugate-gradient algorithm.
5. Update \mathbf{v}^{k+1} using Eq. (3.18).
6. Update \mathbf{d}^{k+1} using Eq. (3.19).
7. Update \mathbf{f}^{k+1} using Eq. (3.20).
9. $k \leftarrow k + 1$
10. **Until:** some stopping criterion is satisfied.

3.5 Numerical Results

We analyze the performance of the proposed super-resolution algorithm under different imaging scenarios. For this, we present the results on PSSI and C-PSSI systems using spectral images in visible and EUV bands. All the experiments are run in MATLAB R2016a on a computer with i7 7700k 4.20 GHZ CPU and 16 GB of RAM.

3.5.1 PSSI

Here we present numerical results to show the performance of the proposed algorithm for EUV and visible bands in PSSI. In the first case, the object of interest is a polychromatic source emitting two quasi-monochromatic waves at wavelengths $\lambda_1 = 33.4$ nm and $\lambda_2 = 33.5$ nm. Simulation setting is same with the EUV band results of Chapter 2. Specifically, for the photon sieve, a sample design in [77] for EUV solar imaging is considered, with the outer diameter of the photon sieve as 25 mm, and the diameter of the smallest hole as $5 \mu\text{m}$. This results in a photon sieve with focal lengths $f_1 = 3.742$ m and $f_2 = 3.731$ m for the two wavelengths. We take measurements at the focal planes corresponding to these wavelengths ($K = 2$). We use solar EUV images of size 512×512 as inputs. We set subsampling factors $\Delta_x = \Delta_y = 2$, and compare the reconstructed images with reconstructions obtained

when there is no-subsampling. We use anisotropic 2D TV as regularizer since spectral correlation in the considered EUV application is limited. The algorithm converges in approximately 150 seconds for all input SNRs.

Figure 3.2 shows reconstructed images when input SNR is 30 dB. When there is subsampling and no-subsampling, the PSNR values are 33.0 dB and 33.5 dB, and SSIM values are 0.93 and 0.95, respectively. Thus, reconstruction quality is similar for both cases in terms of PSNR and SSIM metrics. Visual inspection of Fig. 3.2 is also in agreement with these metrics, showing that both reconstructions provide sharp images and preserve spectral features.

Table 3.2 shows the PSNR and SSIM values for different input SNRs. It can be seen that when there is 2×2 subsampling, the reconstruction performance is robust to noise, and provides slightly lower PSNR and SSIM values compared to the no-subsampling case under even low input SNRs.

In the second case, we consider a dataset of size $128 \times 128 \times 6$ (6 wavelengths from 540 - 590 nm with 10 nm spacing) in visible band that was obtained from an online hyperspectral image database [78]. This simulation setting is different from the visible band results given in Chapter 2. For the photon sieve, a sample design is used [79], with the outer diameter of the photon sieve as 3.36 mm and the diameter of the smallest hole as $15 \mu\text{m}$, resulting in a focal length of 9 cm at 560 nm. We take measurements at the focal planes corresponding to these wavelengths ($K = 6$). We set subsampling factors $\Delta_x = \Delta_y = 2$ again. We use anisotropic 3D TV as regularizer to exploit the spectral correlation in the visible regime. The algorithm converges in approximately 22 seconds for all input SNRs.

Figure 3.3 shows the reconstructed images when the input SNR is 30 dB. Similar to the results in EUV band, image features are well preserved both spatially and spectrally when there is 2×2 subsampling. For numerical evaluation, PSNR and SSIM values for different input SNRs are reported in Table 3.3. From these results, it can be seen that PSNR and SSIM values are lower than the EUV band results for both subsampling and no-subsampling cases. This is an expected result since the number of bands we reconstruct increases from 2 to 6, which increases the ill-posedness of the inverse problem.

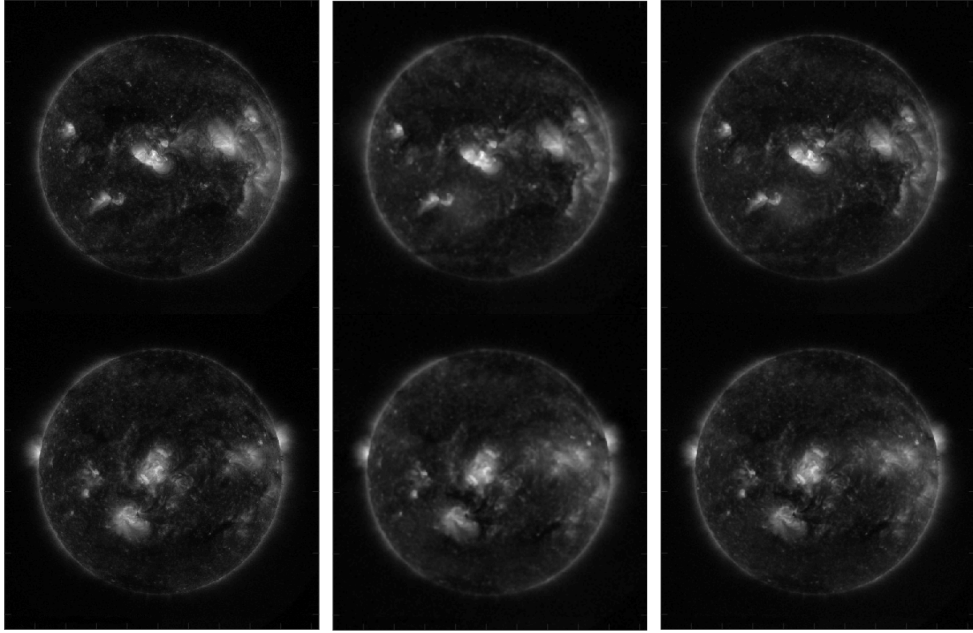


Figure 3.2: Reconstruction of EUV band images ($K = 2$) when input SNR is 30 dB. Left to right: Reference, Reconstruction when there is subsampling ($\Delta_x = \Delta_y = 2$), Reconstruction when there is no subsampling.

Table 3.2: PSNR(dB)/SSIM values for EUV band images ($K = 2$).

Input SNR (dB)	Subsampling ($\Delta_x = \Delta_y = 2$)	No-subsampling
Infinite	39.1/0.95	44.6/0.99
40	35.7/0.94	36.0/0.98
30	33.0/0.93	33.5/0.95
20	30.9/0.89	31.4/0.92

Table 3.3: PSNR(dB)/SSIM values for visible band images ($K = 6$).

Input SNR (dB)	Subsampling ($\Delta_x = \Delta_y = 2$)	No-subsampling
Infinite	35.2/0.97	44.7/0.99
40	32.2/0.94	34.8/0.97
30	30.8/0.91	32.2/0.95
20	27.7/0.83	29.8/0.89

Finally, we test the performance of the reconstruction method when there is severe subsampling. We set $\Delta_x = \Delta_y = 4$, and reconstruct both EUV band and visible

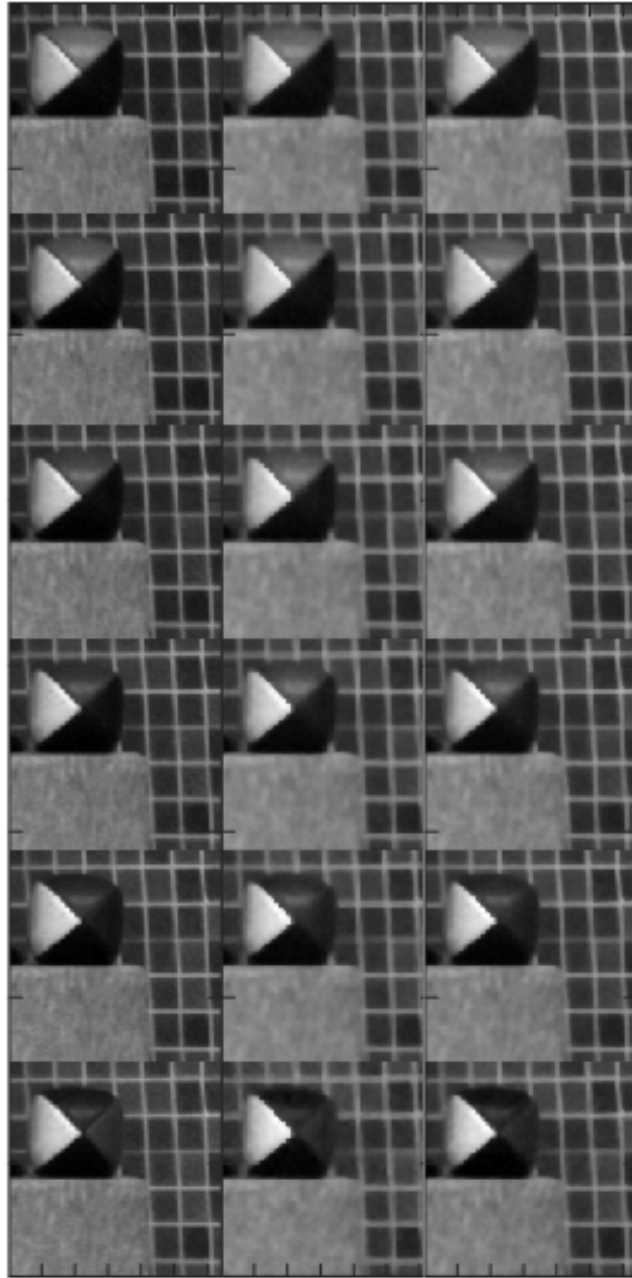


Figure 3.3: Reconstruction of visible band images ($K = 6$) when input SNR is 30 dB. Left to right: Reference, Reconstruction when there is subsampling ($\Delta_x = \Delta_y = 2$), Reconstruction when there is no subsampling.

band data cubes given before when input SNR is 40 dB. For EUV band, PSNR and SSIM values are 33.9 dB and 0.91, respectively. These values are 26.8 and 0.79 for visible band, showing that the effect of subsampling increases as the number of spectral band increases, as expected. Figures 3.4 and 3.5 show the reconstructed images with reference images. As can be seen, both reconstruction involves blur and noise artifacts. Moreover, although the EUV band reconstruction preserves the spectral features, spectral information in some parts is lost in the visible case (for example, see the color change at the right side of the box).

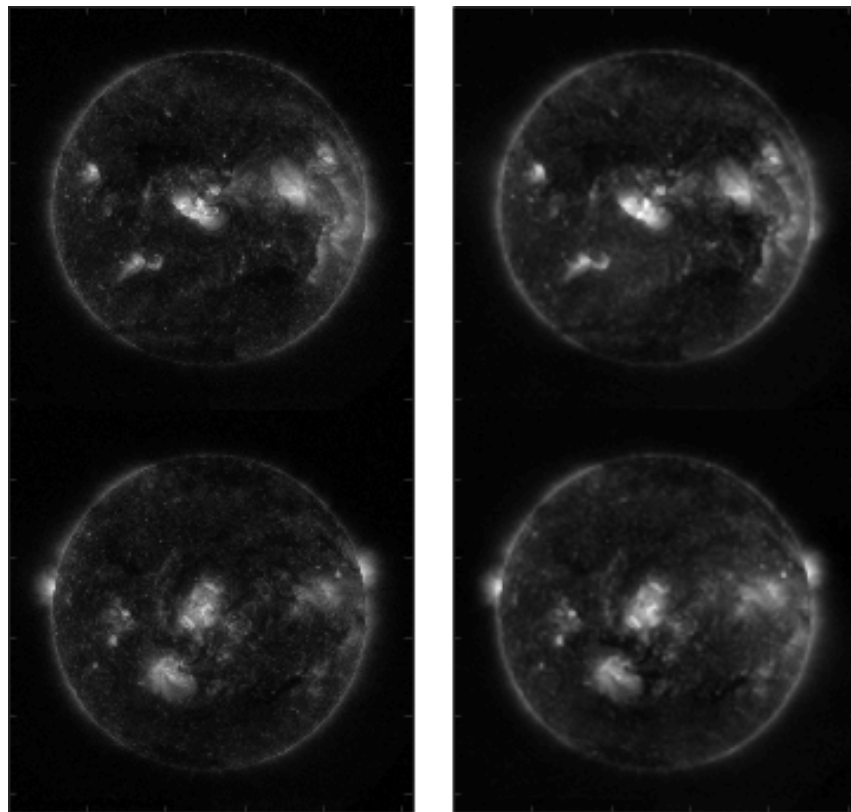


Figure 3.4: Reconstruction of EUV band images ($K = 2$) when input SNR is 40 dB. Left to right: Reference, Reconstruction when there is severe subsampling ($\Delta_x = \Delta_y = 4$).

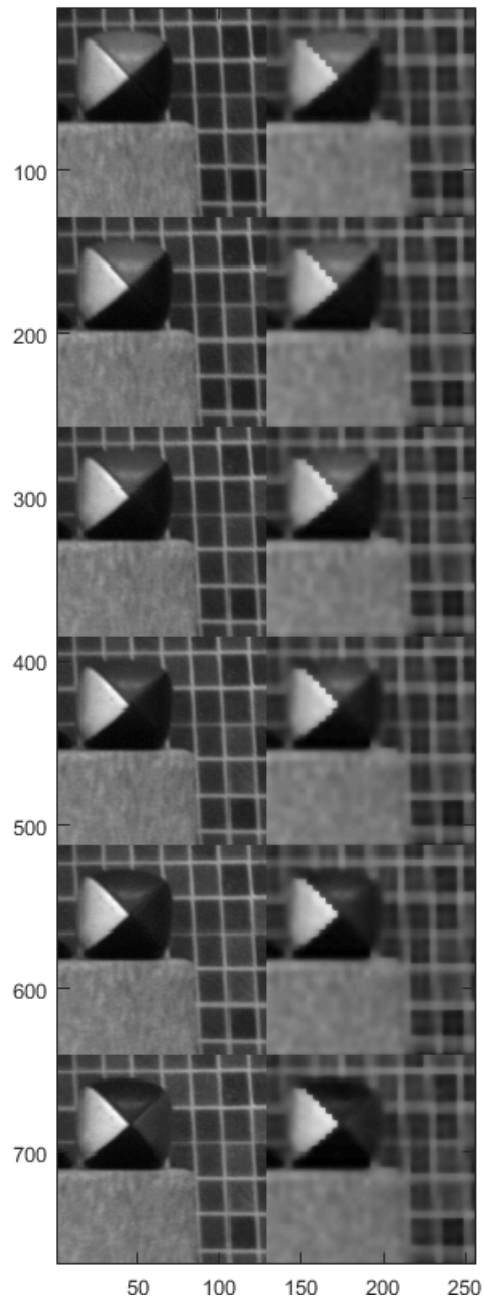


Figure 3.5: Reconstruction of visible band images ($K = 6$) when input SNR is 40 dB. Left to right: Reference, Reconstruction when there is severe subsampling ($\Delta_x = \Delta_y = 4$).

3.5.2 C-PSSI

For C-PSSI, we consider a dataset of size $256 \times 256 \times 6$ (6 wavelengths from 550 - 600 nm with 10 nm spacing) in visible band that was obtained from [78]. For the photon sieve, a slightly new design is used, with the outer diameter of the photon sieve as 3.45 mm and the diameter of the smallest hole as $15 \mu\text{m}$, resulting in a focal length of 9 cm at the wavelength of 575 nm. We take measurements at the focal planes of each wavelength in the dataset ($K = 6$) again. In each measurement, the system applies the masking operation on the individual spectral bands using a colored coded aperture. The entries of these apertures are drawn from a Bernoulli distribution such that 50% of the coded mask pixels is transmissive. For different shots, i.e. l values, different colored coded apertures are used. We set $\Delta_x = \Delta_y = 4$ and $L = 16, 8, 4, 2$ and compare with the $L = 1$ case, i.e. PSSI setting with no coding. We set input SNR levels to 20 dB, 30 dB, 40 dB, and infinite. Each reconstruction takes approximately 30 minutes. Here the results are only presented for the visible case, but not for the EUV case because C-PSSI observation setting is not very practical for the considered EUV application.

Reconstructions for different L values are given in Fig. 3.6 when the input SNR is 40 dB. As can be seen from the figure, reconstruction quality improves both spatially and spectrally as the number of shots, i.e. L , increases. PSNR and SSIM values for different input SNRs are given in Table 3.4. From the reported PSNR and SSIM values, it can be seen that using C-PSSI with multiple shots improves the reconstruction quality compared to the PSSI reconstruction with no coding. Hence, C-PSSI provides better reconstructions than the PSSI as the detector resolution decreases.

Table 3.4: PSNR(dB)/SSIM values for visible band images ($K = 6$) at different L and input SNR values.

SNR \ L	L				
	1 (No Coding-PSSI)	2	4	8	16
20 dB	25.29/0.78	25.84/0.80	26.45/0.82	27.13/0.84	27.84/0.86
30 dB	26.77/0.84	27.60/0.86	28.36/0.87	29.34/0.89	30.46/0.90
40 dB	27.52/0.87	29.40/0.89	30.85/0.91	32.51/0.92	34.21/0.94
∞	32.09/0.92	35.41/0.94	37.85/0.96	51.98/1.00	53.37/1.00

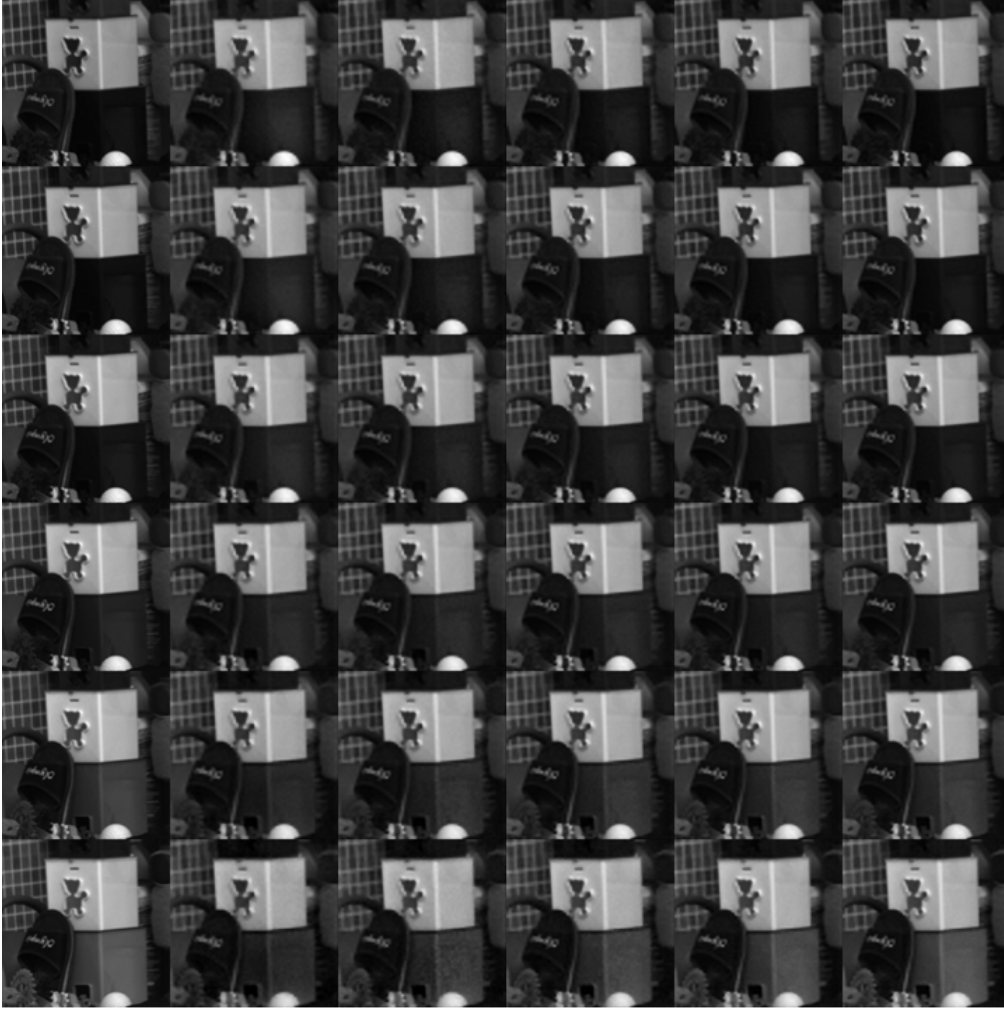


Figure 3.6: Reconstruction of visible band images ($K = 6$) when input SNR is 40 dB and $\Delta_x = \Delta_y = 4$. Left to right: Reference, Reconstruction when $L = 1$ (No coding-PSSI), $L = 2$, $L = 4$, $L = 8$, and $L = 16$.

3.6 Conclusions

In this chapter, we have considered spatial super-resolution problem in photon sieve spectral imaging. We have developed a fast reconstruction method to achieve spatial super-resolution in PSSI system. We have then extended this method to C-PSSI where different colored coded apertures are used to improve the reconstruction performance by taking more measurements. Our method is based on ADMM algorithm and utilizes anisotropic 2D-TV and 3D-TV regularizers for different spectrum characteristics. We have illustrated the performance of the proposed technique using simulations for various scenarios at EUV and visible regimes. The algorithm we propose

offers promising performance in terms of both reconstruction time and quality, and is robust to noise.

For super-resolution in PSSI, no hardware modification is required. We have showed that this system can provide 2×2 super-resolution successfully based on PSNR, SSIM, and visual quality. However, performance of the system degrades at higher subsampling levels. In such cases, C-PSSI with multiple shots should be used to improve the reconstruction quality. We have showed that for 4×4 super-resolution, taking 4 or 8 shots with C-PSSI at each measurement plane provides successful reconstruction performance in terms of PSNR, SSIM, and visual quality. We note that multiple shots can be taken using off-the-shelf spatial light modulators, which provides frame rates up to 1 kHz. Hence, C-PSSI can work in dynamic scenes as well.

CHAPTER 4

COMPRESSIVE SPECTRAL IMAGING WITH DIFFRACTIVE LENSES

4.1 Introduction

As mentioned before, conventional spectral imaging techniques rely on a scanning process to build up the 3D spectral cube from a series of 2D measurements [82]. One important disadvantage is that higher number of scans is needed with increased spatial and spectral resolutions [4]. This generally leads to low light throughput, increased hardware complexity, and long acquisition times, resulting in temporal artifacts in dynamic scenes [5]. Moreover, the temporal, spatial, and spectral resolutions are inherently limited as they are purely determined by the physical elements involved.

Compressive spectral imaging provides an effective way to overcome these limitations by passing on some of the burden to a computational system. It enables to reconstruct the entire spectral cube from a few multiplexed measurements via sparsity-based reconstruction. This is made possible by compressive sensing (CS) which relies on two principles: sparsity of the spectral images in some transform domain and incoherence of the measurements. It is widely known that spectral images exhibit both spatial and spectral correlations, which allow sparse representations [4]. For the incoherence of the measurements, different compressive spectral imaging techniques have been proposed such as coded aperture snapshot spectral imaging (CASSI) [4, 83, 84] and compressive hyperspectral imaging by separable spectral and spatial operators (CHISS) [11].

Some parts of this chapter have been presented in [79, 80], and also submitted for publication [81].

In this chapter, we develop a novel compressive spectral imaging technique named *compressive spectral imaging with diffractive lenses* (CSID). CSID uses a coded aperture to spatially modulate the optical field from the scene and a diffractive lens such as a photon sieve [22, 70] for dispersion. The coded field is first passed through the diffractive lens and then measured at a few planes using a moving detector. A fast sparse recovery method is also developed to reconstruct the spectral cube from these compressive measurements. The performance is illustrated numerically for various settings. Different than the earlier works that use diffractive lenses for spectral imaging [22, 14, 15, 16], here we utilize them for the first time in a compressive modality.

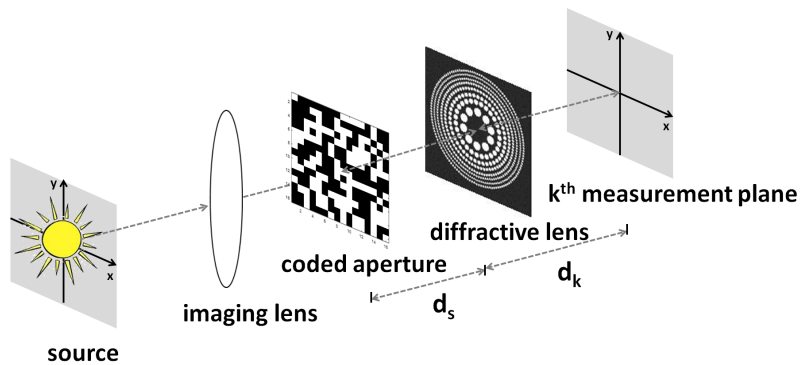


Figure 4.1: Illustration of the CSID system.

Figure 4.1 illustrates the CSID system, which has a simple optical configuration consisting of (1) an imaging lens, (2) a coded mask, (3) a diffractive lens (such as a photon sieve [22, 70]), and (4) a monochrome detector [79]. First the image of the scene is formed on the plane of the coded mask. Then the coded field is passed through the diffractive lens. Since the diffractive lens has a wavelength-dependent focal length, each spectral component is exposed to a different amount of focus. As a result, each measurement is a superposition of differently blurred and coded spectral bands. Using a moving detector, a total of K such measurements can be recorded at different distances from the diffractive lens.

4.2 Forward Problem

The measurements obtained with the CSID system can be related to the intensity of each spectral component as follows:

$$y_k(u, v) = \int (f_\lambda(u, v) * h_{d_k, \lambda}(u, v)) b(\lambda) d\lambda. \quad (4.1)$$

Here $y_k(u, v)$ represents the k th measurement obtained at distance d_k , $f_\lambda(u, v) = x_\lambda \left(-\frac{d_s}{d_k} u, -\frac{d_s}{d_k} v \right) c_\lambda \left(-\frac{d_s}{d_k} u, -\frac{d_s}{d_k} v \right)$ is the coded and scaled intensity of the spectral field $s_\lambda(u, v)$ with the coded aperture $c_\lambda(u, v)$. Assuming an ideal imaging lens with unit magnification, the coded and scaled intensity $f_\lambda(u, v)$ is convolved with the incoherent point-spread function (PSF) of the diffractive lens, $h_{d_k, \lambda}(u, v)$, which has a closed-form expression given elsewhere [31]. Lastly, $b(\lambda)$ denotes the spectral response of the detector. Note that although the terms $x_\lambda \left(-\frac{d_s}{d_k} u, -\frac{d_s}{d_k} v \right)$'s involve different scaling for different k 's, when d_s is much larger than d_k , this scaling can be effectively taken as the same.

We discretize the spectral field into S spectral bands, and $x_s(u, v)$ represents the intensity of the s th band with central wavelength λ_s . This spectral component is modulated with the coded mask which has pattern $c_s(u, v)$ at wavelength λ_s . The patterns $c_s(u, v)$ are the same for all wavelengths ($s = 1, \dots, S$) if an uncolored (traditional block-unblock) mask is used; however, the mask patterns will be different if a colored coded aperture [85] is used instead. The coded aperture $c_s(u, v) = \sum_{m, n} c_s[m, n] \text{rect} \left(\frac{u}{\Delta_c} - m, \frac{v}{\Delta_c} - n \right)$ is a pixelated array with a pixel size of Δ_c , and $c_s[m, n]$ denotes the value of the coded aperture at pixel (m, n) .

After discretizing the spectral field along the spectral dimension, discretization along the spatial dimensions is also needed to arrive at a discrete model. By replacing each spatially continuous function with its discretized version, we can obtain the following discrete forward model:

$$y_k[m, n] = \sum_{s=1}^S (x_s[m, n] c_s[m, n]) * h_{d_k, \lambda_s}[m, n] b_s. \quad (4.2)$$

Here, $y_k[m, n]$ denotes the k th measurement obtained over $N_x \times N_y$ detector pixels, and corresponds to the samples of $y_k(u, v)$, i.e. $y_k[m, n] = y_k(m\Delta, n\Delta)$. The sampling interval Δ corresponds to the pixel size of the detector. The coded aperture

pixel size can be chosen as an integer multiple of Δ to avoid the need for subpixel positioning accuracy. Here, we choose $\Delta_c = \Delta$ for simplicity. Moreover, $x_s[m, n]$ and $h_{d_k, \lambda_s}[m, n]$ are the uniformly sampled versions of their continuous counterparts with the same sampling interval Δ . Lastly, b_s represents the coefficient resulting from the response of the detector at the central wavelength λ_s .

The above discrete forward model can be expressed in matrix-vector form as follows:

$$\mathbf{y} = \mathbf{H}\mathbf{C}\mathbf{x} + \mathbf{w}, \quad (4.3)$$

where $\mathbf{y} = [\mathbf{y}_1^T, \dots, \mathbf{y}_K^T]^T \in R^{KN}$ is vertically concatenated measurement vector with $N \triangleq N_x N_y$ where $\mathbf{y}_k \in R^N$ represents the k th measurement vector. Similarly, $\mathbf{x}_s \in R^N$ is the vector corresponding to the spectral image with wavelength λ_s , and $\mathbf{x} = [\mathbf{x}_1^T, \dots, \mathbf{x}_S^T]^T \in R^{SN}$ is the concatenated image vector. The $KN \times SN$ matrix \mathbf{H} consists of $N \times N$ convolution matrices representing the convolutions with PSFs $h_{d_k, \lambda_s}[m, n]$. The diagonal matrix $\mathbf{C} \in R^{SN \times SN}$ represents the overall coding operation, and has values 0 or 1 along its diagonal. Finally, the vector $\mathbf{w} = [n_1^T, \dots, n_K^T]^T$ denotes the measurement noise, which is often white Gaussian. In our setting, the number of measurements (K) is smaller than the number of spectral bands (S), which results in an under-determined system of equations.

4.3 Image Reconstruction Method

In the inverse problem, the goal is to reconstruct the unknown spectral images, \mathbf{x} , from their compressive superimposed measurements, \mathbf{y} , which correspond to their coded and blurred versions. This problem is inherently ill-posed. There are a variety of approaches to solve such ill-posed linear inverse problems. Here, to exploit the sparsity of the spectral images after some transformation Φ , we present two different image reconstruction approaches using ℓ_1 -norm based and ℓ_0 -norm based regularization. We first formulate each associated inverse problem and then solve it efficiently by developing a fast sparse recovery algorithm.

4.3.1 ℓ_1 -norm Based Regularization

In the first reconstruction approach, we formulate the inverse problem as the following constrained optimization problem:

$$\min_{\mathbf{x}} \|\Phi\mathbf{x}\|_1 \text{ subject to } \|\mathbf{y} - \mathbf{HC}\mathbf{x}\|_2 \leq \epsilon, \quad (4.4)$$

where $\epsilon \geq 0$ is a parameter that depends on noise variance. Here the ℓ_1 -norm enforces the sparsity of the spectral cube after transformation with Φ , as motivated by the CS theory [86].

To solve the resulting optimization problem, we convert our constrained problem to an unconstrained problem by adding the constraint to the objective function as a penalty function:

$$\min_{\mathbf{x}} \|\Phi\mathbf{x}\|_1 + \iota_{(\|\mathbf{y}-\mathbf{HC}\mathbf{x}\|_2 \leq \epsilon)}(\mathbf{x}), \quad (4.5)$$

where the indicator function $\iota_{(\|\mathbf{y}-\mathbf{HC}\mathbf{x}\|_2 \leq \epsilon)}(\mathbf{x})$ takes value 0 if the constraint is satisfied, and $+\infty$ otherwise. We solve this problem by developing a fast reconstruction algorithm that is based on alternating direction method of multipliers (ADMM) [38].

After variable-splitting, this results in the following problem:

$$\begin{aligned} & \underset{\mathbf{x}, \mathbf{z}^{(1)}, \mathbf{z}^{(2)}}{\text{minimize}} && \|\Phi\mathbf{z}^{(1)}\|_1 + \iota_{(\|\mathbf{y}-\mathbf{z}^{(2)}\|_2 \leq \epsilon)}(\mathbf{z}^{(2)}) \\ & \text{subject to} && \mathbf{z}^{(1)} = \mathbf{x}, \quad \mathbf{z}^{(2)} = \mathbf{HC}\mathbf{x} \end{aligned} \quad (4.6)$$

where $\mathbf{z}^{(1)}, \mathbf{z}^{(2)}$ are the auxiliary variables in the ADMM framework. After expressing the problem in Eq. 4.6 in augmented Lagrangian form [38], minimization over $\mathbf{x}, \mathbf{z}^{(1)}$, and $\mathbf{z}^{(2)}$ is needed. Here, we minimize them in an alternating fashion.

For minimization over \mathbf{x} , we face a least-squares problem which has the following normal equation:

$$(\mathbf{I} + \mathbf{CH}^H\mathbf{HC})\mathbf{x}_{k+1} = (\mathbf{z}^{(1)} + \mathbf{d}^{(1)} + \mathbf{CH}^H(\mathbf{z}^{(2)} + \mathbf{d}^{(2)})) \quad (4.7)$$

with \mathbf{d} denoting the dual variable in the ADMM framework. A direct matrix inversion approach for solving the linear system in Eq. (4.7) is not feasible for large-scale spectral cubes. Here, we solve this iteratively using the conjugate-gradient method. For this iterative process, forming any of the matrices is not required, which provides huge savings for the memory as well as the computation time. Specifically,

multiplications with matrices \mathbf{H} and \mathbf{H}^H correspond to summation of some convolutions. That is, for multiplication with \mathbf{H} matrix, we can simply take 2D Fourier transforms of underlying PSFs $h_{d_k, \lambda_1}[m, n], \dots, h_{d_k, \lambda_S}[m, n]$ and the spectral images $x_1[m, n], \dots, x_S[m, n]$, multiplying them elementwise, and then summing all the results. For multiplication with \mathbf{H}^H matrix, a similar operation is performed using the PSFs $h_{d_1, \lambda_s}[m, n], \dots, h_{d_K, \lambda_s}[m, n]$. Lastly, the required multiplications with \mathbf{C} in the iterative process reduce to simple elementwise multiplications with coded aperture functions $c_s[m, n]$.

For minimization over $\mathbf{z}^{(1)}$, we need to perform the following operation involving soft-thresholding:

$$\mathbf{z}_{k+1}^{(1)} = \Phi^{-1}(\text{soft}(\Phi(\mathbf{x}_{k+1} - \mathbf{d}_k^{(1)}), \frac{1}{\mu})), \quad (4.8)$$

Here, $\text{soft}(\mathbf{w}, \tau)$ denotes the soft-thresholding operation and is component-wise computed as $w_i \rightarrow \text{sign}(w_i) \max(|w_i| - \tau, 0)$ for all i , with $\text{sign}(w_i)$ taking value 1 if $w_i > 0$ and -1 otherwise [38]. That is, the solution in (4.8) can be obtained by first transformation with Φ , followed by soft-thresholding with parameter $1/\mu$, and inverse transformation operation Φ^{-1} .

For minimization over $\mathbf{z}^{(2)}$, a projection of $\mathbf{s} \triangleq (\mathbf{H}\mathbf{C}\mathbf{x}_{k+1} - \mathbf{d}_k^{(2)})$ onto ϵ -radius hypersphere centered at \mathbf{y} is required [38]. This projection has the following form:

$$\mathbf{z}_{k+1}^{(2)} = \begin{cases} \mathbf{y} + \epsilon \frac{\mathbf{s} - \mathbf{y}}{\|\mathbf{s} - \mathbf{y}\|_2}, & \text{if } \|\mathbf{s} - \mathbf{y}\|_2 > \epsilon \\ \mathbf{s}, & \text{if } \|\mathbf{s} - \mathbf{y}\|_2 \leq \epsilon. \end{cases} \quad (4.9)$$

As a result, we have three update steps resulting from the ADMM formulation, i.e. \mathbf{x} -update, $\mathbf{z}^{(1)}$ -update, and $\mathbf{z}^{(2)}$ -update. The overall algorithm is summarized in Table 4.1.

Table 4.1: ℓ_1 -norm based reconstruction algorithm for CSID

Input: Compressive measurements \mathbf{y} obtained using (4.3).

Initialization: Initialize iteration count $k = 0$, choose $\mu > 0$, ϵ , $\mathbf{z}_0^{(1)}$, $\mathbf{z}_0^{(2)}$, $\mathbf{d}_0^{(1)}$, $\mathbf{d}_0^{(2)}$.

Main Iteration: Increment k by 1 and repeat the following steps until some stopping criterion is satisfied.

1. Calculate spectral images \mathbf{x}_{k+1} by solving (4.7) using conjugate-gradient algorithm.
2. Calculate $\mathbf{z}_{k+1}^{(1)}$ using soft-thresholding in (4.8).
3. Calculate $\mathbf{z}_{k+1}^{(2)}$ using projection in (4.9).
4. Update $\mathbf{d}_{k+1}^{(1)}$ as $\mathbf{d}_{k+1}^{(1)} = \mathbf{d}_k^{(1)} - (\mathbf{x}_{k+1} - \mathbf{z}_{k+1}^{(1)})$.
5. Update $\mathbf{d}_{k+1}^{(2)}$ as $\mathbf{d}_{k+1}^{(2)} = \mathbf{d}_k^{(2)} - (\mathbf{H}\mathbf{C}\mathbf{x}_{k+1} - \mathbf{z}_{k+1}^{(2)})$.

Output: Spectral images \mathbf{x} .

4.3.2 ℓ_0 -norm Based Regularization

To enforce sparsity, we can also formulate the inverse problem as follows:

$$\min_{\mathbf{x}, \mathbf{b}} \nu \|\mathbf{y} - \mathbf{H}\mathbf{C}\mathbf{x}\|^2 + \sum_{j=1}^{SN} \|\mathbf{W}\mathbf{P}_j\mathbf{x} - \mathbf{b}_j\|_2^2 \quad s.t. \quad \|\mathbf{b}\|_0 \leq \beta \quad (4.10)$$

Here we extract 3D patches of size $n_1 \times n_1 \times n_2$ from the data cube using $\mathbf{P}_j \in R^{L \times SN}$ operator ($L = n_1^2 n_2$). Then we promote sparsity of these patches in the 3D discrete cosine transform (DCT) domain. This is done by transforming each patch to this transform domain using the 3D DCT operator $\mathbf{W} \in R^{L \times L}$. Vector $\mathbf{b}_j \in R^L$ is the sparse code vector of the j th patch, and $\mathbf{b} \in R^{LSN}$ is obtained by concatenating \mathbf{b}_j sparse code vectors. Finally, ν controls the weight between the two terms in the objective function while β is the sparsity parameter.

To solve the resulting optimization problem, we develop a fast alternating minimization approach which *alternately* minimizes the objective term in Eq. (4.10) over the spectral images \mathbf{x} and sparse codes \mathbf{b} .

In the sparse coding step, the objective is minimized over \mathbf{b} while \mathbf{x} is kept fixed;

the optimal solution is obtained by assigning the largest β elements of all patches $\{\mathbf{W}\mathbf{P}_j\mathbf{x}\}_{j=1}^{SN}$ to \mathbf{b} , and zeroing the others.

In the spectral cube update step, the minimization problem over \mathbf{x} is solved while \mathbf{b} is kept fixed. This is a least-squares problem whose *linear* normal equation has the following form:

$$(\nu\mathbf{C}\mathbf{H}^H\mathbf{H}\mathbf{C} + \mathbf{G})\mathbf{x} = (\nu\mathbf{C}\mathbf{H}^H\mathbf{y} + \mathbf{z}) \quad (4.11)$$

where $\mathbf{G} = \sum_{j=1}^{SN} \mathbf{P}_j^T \mathbf{W}^H \mathbf{W} \mathbf{P}_j = \mathbf{I}_{SN}$ and $\mathbf{z} = \sum_{j=1}^{SN} \mathbf{P}_j^T \mathbf{W}^H \mathbf{x}$ with \mathbf{I}_{SN} denoting the $SN \times SN$ identity matrix. We solve this normal equation using a conjugate-gradient algorithm. Multiplication with \mathbf{H} matrix is efficiently calculated using FFT, as explained before. The overall algorithm is summarized in Table 4.2.

Table 4.2: ℓ_0 -norm based reconstruction algorithm for CSID

Input: Compressive measurements \mathbf{y} obtained using (4.3).

Initialization: Initialize iteration count $k = 0$, choose $\nu > 0, \beta > 0$, \mathbf{x} .

Main Iteration: Increment k by 1 and repeat the following steps until some stopping criterion is satisfied.

1. Calculate spectral images \mathbf{x}_{k+1} by solving Eq. (4.11) using conjugate-gradient algorithm.
2. Calculate \mathbf{b}_{k+1} by assigning the largest β elements of $\{\mathbf{W}\mathbf{P}_j\mathbf{x}\}_{j=1}^{SN}$ to \mathbf{b} , and zeroing the others.

Output: Spectral images \mathbf{x} .

4.3.3 Computational Complexity

For the ℓ_1 -norm based regularization method, similar to Chapter 2, dual variable updates and Moreau proximal mappings have $O(SN)$ cost. The complexity of the overall algorithm is $O(SN \log(N))$ due to the FFT algorithm used in multiplications with \mathbf{H} and \mathbf{H}^H .

For the ℓ_0 -norm based regularization method, complexity is dominated by $\mathbf{W}\mathbf{P}_j\mathbf{x}$

operation in the sparse coding step [48]. Its computational complexity is $O(L^2SN^2)$. The spectral cube update step requires multiplications with \mathbf{H} and \mathbf{H}^H . Its complexity is $O(SN \log(N))$. Thus, the complexity of the overall algorithm is $O(L^2SN^2)$.

4.4 Numerical Results

4.4.1 ℓ_1 -norm Based Regularization

We now present numerical simulations to illustrate the performance of the developed imaging technique. We consider a spectral scene of size $256 \times 256 \times 10$ (10 wavelengths from the range 530 – 620 nm with 10 nm interval), which was taken from an online hyperspectral database [54]. For the diffractive lens, the same design with the C-PSSI setting at visible regime is used, as explained in Section 3.5.2. Specifically, we consider a photon sieve design with an outer diameter of 3.45 mm and the smallest hole diameter of $\delta = 15 \mu\text{m}$. This results in a focal length of $f_0 = 9 \text{ cm}$ at the central wavelength $\lambda_0 = 575 \text{ nm}$ and Abbe’s spatial resolution of $15 \mu\text{m}$. The pixel size of the detector, Δ , is chosen as $7.5 \mu\text{m}$ to match the expected spatial resolution. Moreover, the expected spectral resolution is $4\delta^2/f_0 = 10 \text{ nm}$, as given by the spectral bandwidth of the diffractive lens [27][Chap. 9]. Note that this expected spectral resolution matches the chosen spectral sampling interval, i.e. 10 nm.

The compressive measurements are simulated using the model in Eq. (4.3) with additive Gaussian noise. In each measurement, the system applies the masking operation on individual spectral bands using colored coded apertures. The entries of these apertures are drawn from a Bernoulli distribution. A sample mask pattern is shown in Fig. 4.2. After the coded field passes through the photon sieve, we capture measurements at different planes. A sample compressive measurement is shown in Fig. 4.2 together with the true spectral cube superimposed (integrated) along the spectral dimension. As seen, the measurements involve not only the superposition of all spectral images but also a significant amount of blur and degradation.

We consider different compressive scenarios with 2, 3, 4, and 5 measurements taken at different planes with equidistant points from the central focal plane. These cor-

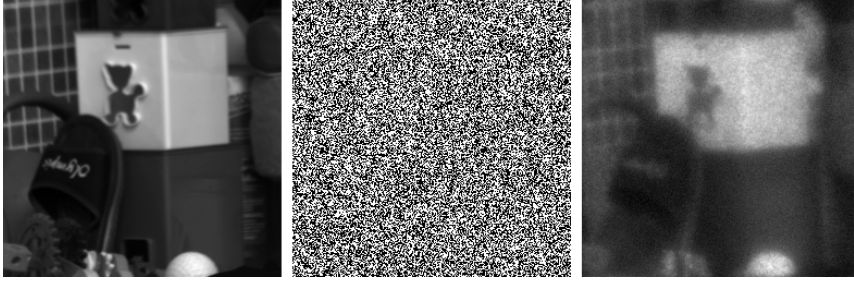


Figure 4.2: Demonstration of compressive measurements obtained with CSID. Left to right: Superimposed true image, sample mask pattern, sample compressive measurement.

respond to compression ratios (CRs), $100 \times (1 - K/S)$, of 80%, 70%, 60%, and 50%, respectively. Different measurement SNRs of 20, 30, and 40 dB are also considered for the additive noise. Reconstructions are obtained from these compressive and noisy measurements using the algorithm in Table 4.1. Similar to previous compressive spectral imaging approaches [4], we enforce sparsity in a Kronecker basis $\Phi = \Phi_1 \otimes \Phi_2$ where Φ_1 is the basis for 2D Symmlet-8 wavelet and Φ_2 is the 1D discrete cosine (DCT) basis. This transformation with Φ is computed by first taking the 2D Symmlet-8 transform of each spectral image and then the 1D DCT along the spectral dimension. One reconstruction takes approximately 35 seconds on a computer with 16 GB of RAM and i7 7700K 4.20 GHz CPU.

Table 4.3 shows the average PSNRs for the considered measurement scenarios. It can be seen that PSNR is above 30 dB at 70% compression ratio and 30 dB input SNR, which demonstrates the high-quality reconstruction of the spectral cube in practical imaging scenarios. In addition, the performance degrades gracefully with decreasing input SNR and increasing compression ratio. That is, the imaging performance is also robust to high noise and compression levels.

To visually evaluate the results, we present in Fig. 4.3 the reconstructed spectral images at 30 dB input SNR and different compression ratios, together with the true spectral images. We can see that the image details and edges, as well as the spectral variations, are well preserved in the reconstructions. In the bottom of the figure, superimposed reconstructions along the spectral dimension are also shown, which

are indistinguishable from the true one. Hence, the results demonstrate the successful reconstruction of the spectral image cube from compressive measurements with compression ratios of as high as 80%.

To further demonstrate the successful recovery along the spectral dimension, we select three representative spatial points with different spectral characteristics. These points P1, P2, and P3 are shown in Fig. 4.3. The reconstructed spectra at these points are plotted in Fig. 4.4, together with the ground truth. It can be seen that the spectrum is recovered almost perfectly in all compression ratios for P1. At points P2 and P3, the reconstruction with 80% compression ratio slightly deviates from the ground truth, while other compression ratios provide good reconstructions.

To also numerically evaluate the spectrum recovery performance, the normalized mean squared error (NMSE) for the spectrum is computed at these selected points, using $\|\mathbf{x} - \mathbf{x}^*\|_2^2 / \|\mathbf{x}\|_2^2$ where \mathbf{x} is the ground truth and \mathbf{x}^* is the reconstructed spectrum. The resulting NMSE values are given in Table 4.4. These values also support the successful recovery of the spectrum with a typical NMSE value of less than 1%.

Table 4.3: Comparison of average PSNRs (dB) for different compressive measurement scenarios and SNRs.

SNR (dB)	80% CR	70% CR	60% CR	50% CR
20	25.34	27.43	28.11	28.54
30	27.65	31.52	32.61	33.07
40	29.14	34.56	36.29	37.00



Figure 4.3: Reconstructed spectral images (at 10 wavelengths in the range 530 – 620 nm with 10 nm spacing) from compressive measurements when input SNR is 30 dB. Left to right: true images, reconstructions with 50%, 60%, 70%, and 80% CR. Superimposed (summed) spectral cubes along the spectral dimension are shown at the bottom part.

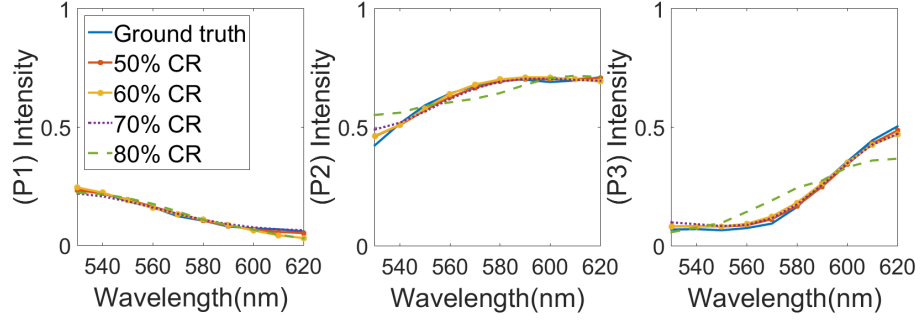


Figure 4.4: Spectrum at three spatial positions P1, P2, and P3.

Table 4.4: NMSE of the spectrum at the selected points.

Point #	80% CR	70% CR	60% CR	50% CR
1	1.14%	0.33%	0.86%	0.18%
2	0.67%	0.15%	0.06%	0.06%
3	6.92%	0.55%	0.52%	0.26%

4.4.1.1 Effect of Different Transform Choices

Here we obtain reconstructions using the same measurement settings with different priors to investigate the effect of prior selection on the reconstruction quality. For this, we choose Φ as 3D TV, 3D Full DCT (which takes 3D DCT of the full spectral cube), 3D Patched DCT (which takes 3D DCT of $16 \times 16 \times 4$ patches of the spectral cube with a stride of 3), Kronecker product of 2D Daubechies Wavelet and 1D DCT (2D Daub + 1D DCT), and Kronecker product of 2D Symmlet-8 Wavelet and 1D DCT (2D Symm + 1D DCT). PSNRs for these priors are given in Table 4.5 for different CRs and input SNRs. From these results, it can be seen that 3D Full DCT performs best at lower input SNRs while 3D Patched DCT provides the highest PSNR as the input SNR increases. On the other hand, wavelet-based priors, i.e. 2D

Daub + 1D DCT and 2D Symm + 1D DCT, have comparable performance with 3D Full DCT at lower input SNRs, and better than 3D Patched DCT. Finally, in all of the measurement settings, 3D TV performs the worst. This is because while the 3D TV prior is successful in preserving spatial features, it causes over-smoothing in the spectral direction, which limits its reconstruction capability. 3D DCT based priors, on the other hand, capture the spectral changes across different bands successfully. However, their reconstructions involve noisy artifacts, which degrades spatial performance. Finally, utilizing 2D wavelet-based priors along spatial dimensions and 1D DCT along spectral dimension offers the best performance.

To understand the effect of different sparsity priors on the spectrum, NMSE of the reconstructed spectrum at points P1, P2, and P3 are given in Table 4.6 for different CRs for SNR=30 dB case. From the NMSE results, it can be seen that 2D Daub + 1D DCT and 2D Symm + 1D DCT recover the spectrum much better than the other priors for all cases. However, since the PSNR of 2D Symm + 1D DCT is better than the 2D Daub + 1D DCT prior, especially at high input SNR levels, we conclude that it provides the best reconstruction performance among all these priors. Reconstructions using this prior were given in Fig. 4.3. For comparison, we also present reconstructions using other priors in Figure 4.5, 4.6, 4.7, and 4.8 when input SNR is 30 dB. Visual inspection shows that 2D Symm + 1D DCT reconstruction preserves spatial image features as well as spectral changes while other reconstructions lose spectral information in some regions and exhibit noisy artifacts.

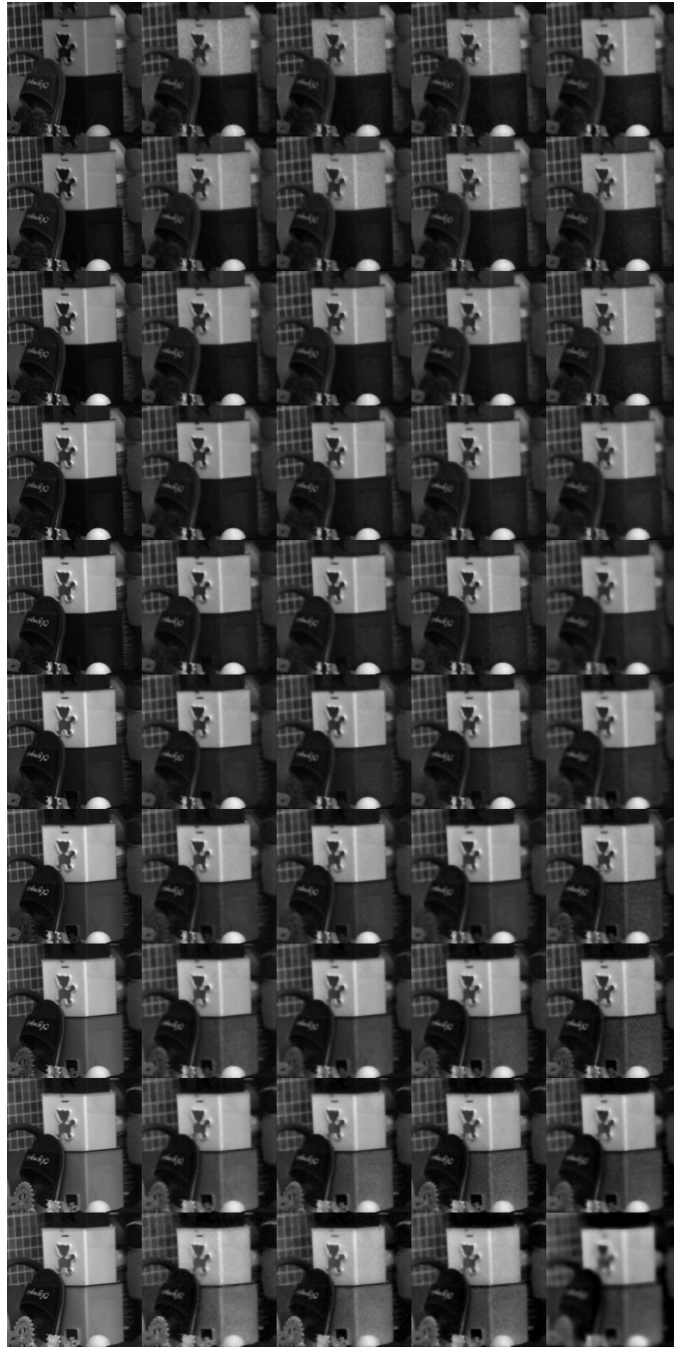


Figure 4.5: Reconstructed spectral images (at 10 wavelengths in the range 530 – 620 nm with 10 nm spacing) from compressive measurements using 3D TV prior when input SNR is 30 dB. Left to right: true images, reconstructions with 50%, 60%, 70%, and 80% CR.



Figure 4.6: Reconstructed spectral images (at 10 wavelengths in the range 530 – 620 nm with 10 nm spacing) from compressive measurements using 3D Full DCT prior when input SNR is 30 dB. Left to right: true images, reconstructions with 50%, 60%, 70%, and 80% CR.



Figure 4.7: Reconstructed spectral images (at 10 wavelengths in the range 530 – 620 nm with 10 nm spacing) from compressive measurements using 3D Patched DCT prior when input SNR is 30 dB. Left to right: true images, reconstructions with 50%, 60%, 70%, and 80% CR.



Figure 4.8: Reconstructed spectral images (at 10 wavelengths in the range 530 – 620 nm with 10 nm spacing) from compressive measurements using 2D Daub + 1D DCT prior when input SNR is 30 dB. Left to right: true images, reconstructions with 50%, 60%, 70%, and 80% CR.

Table 4.5: Comparison of average PSNRs (dB) for different priors, different compressive measurement scenarios, and SNRs. Prior results are given in the following SNR order: 20 dB, 30 dB, 40 dB. For a given CR and input SNR, priors with highest PSNR (within 0.1 dB margin) are given in bold numbers.

Prior	80% CR	70% CR	60% CR	50% CR
3D TV	23.33/25.10/27.19	24.28/26.99/30.36	25.11/28.65/32.28	25.53/29.32/33.06
3D Full DCT	25.72/27.80/29.69	27.65/32.08/35.32	28.60/33.19/36.92	29.10/33.58/37.59
3D Patched DCT	24.49/27.05/ 30.24	26.64/31.85/ 35.77	27.83/ 33.29/37.32	28.20/ 33.76/37.83
2D Daub + 1D DCT	25.37/27.56/29.11	27.26/31.16/33.82	27.80/32.17/35.35	28.29/32.60/35.87
2D Symm + 1D DCT	25.34/27.65/29.14	27.43/31.52/34.56	28.11/32.61/36.29	28.54/33.07/37.00

Table 4.6: Comparison of NMSE of the spectrum (in %) at the selected points for different priors and different compressive measurement scenarios when the input SNR is 30 dB. Prior results are given in the following point order: P1, P2, and P3. For a given CR and point, priors with lowest NMSE (within 0.1 % margin) are given in bold numbers.

Prior	80% CR	70% CR	60% CR	50% CR
3D TV	3.44/1.33/20.42	2.36/1.11/7.87	2.75/0.72/3.90	1.95/0.98/3.67
3D Full DCT	2.53/0.80/8.04	1.41/ 0.17 /1.02	1.15/ 0.06 /1.15	0.80/ 0.05 /0.50
3D Patched DCT	3.91/0.97/9.02	2.06/ 0.18 /1.04	0.77/ 0.08 /1.08	0.54/ 0.08 /0.71
2D Daub + 1D DCT	1.16/0.58/6.37	0.32/0.22/0.53	0.27/0.10/0.31	0.36/ 0.04/0.31
2D Symm + 1D DCT	1.14/0.67/6.92	0.33/0.15/0.55	0.86/ 0.06 /0.52	0.18/0.06/0.26

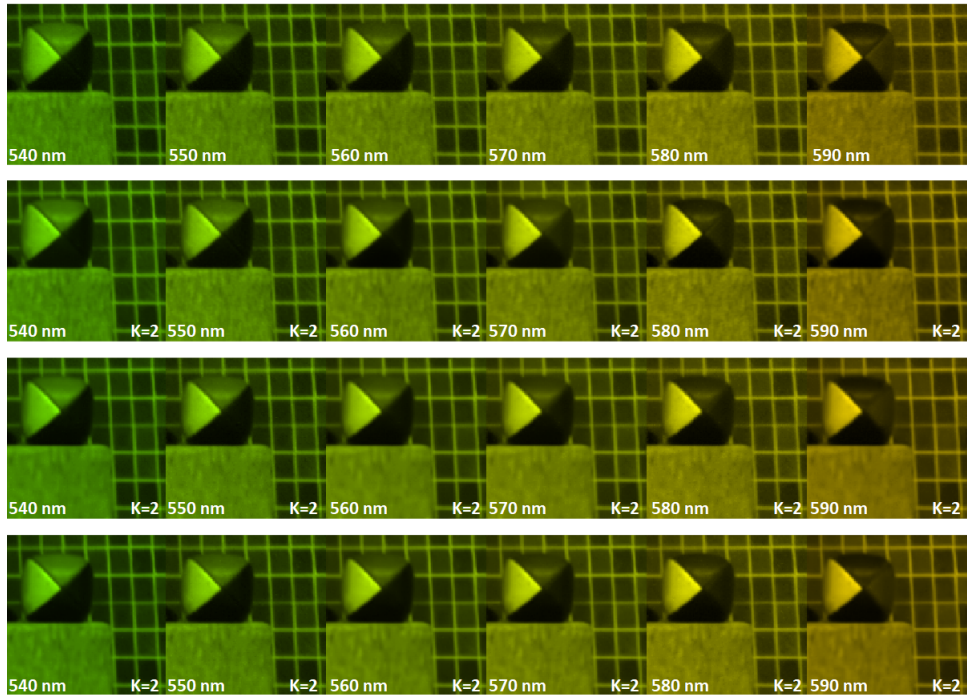
4.4.2 ℓ_0 -norm Based Regularization

Here we present numerical simulations to illustrate the performance using ℓ_0 -norm based regularization. We consider a dataset of size $128 \times 128 \times 6$ (6 wavelengths from 540 – 590 nm with 10 nm spacing), which was obtained from an online hyper-spectral image database at the University of Manchester. For the diffractive lens, the same design with the PSSI setting at visible regime is used, which is explained in Section 3.5.1. For this, the outer diameter is selected as 3.36 mm and the diameter of the smallest hole as $15 \mu\text{m}$, resulting in a focal length of 9 cm at 560 nm. The measurements are simulated using the model in (4.3) with randomly generated colored or uncolored coded masks.

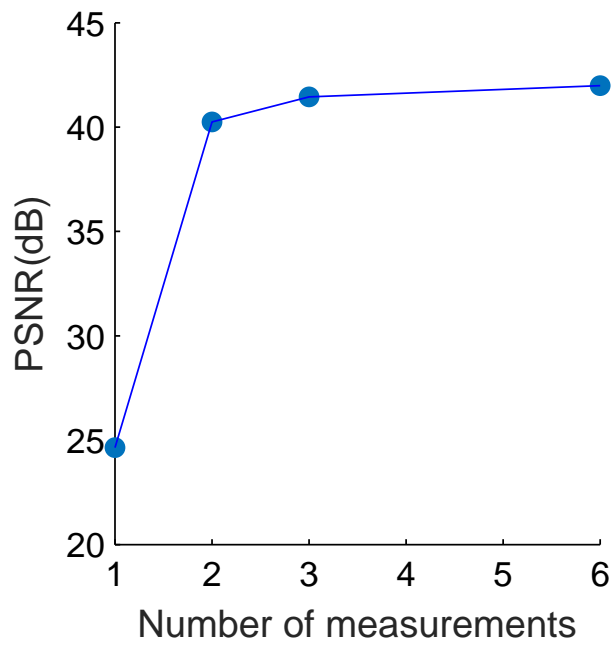
In the first analysis, 2 noiseless measurements are taken at the focal planes of the second and fifth spectral components by using no mask, uncolored and colored coded apertures. Reconstructed images for these three cases are given in Fig. 4.9a together with the true images. The results demonstrate the successful reconstruction of the spectral cube from compressive measurements with a PSNR of more than 40 dB when either uncolored or colored masks are used.

For the second analysis, the above experiment is repeated for $K = 1, 3,$ and 6 cases, with the 3 measurements taken at the midpoints of successive wavelength sources in the two extreme ends, and one in the center. Fig. 4.9b shows the reconstruction performance for different compression ratios for the colored mask case. This suggests that compression ratios of up to 33% allows almost perfect recovery. In the third analysis, the effect of noise is explored by generating noisy measurements with different SNRs. Table 4.7 shows the PSNRs for the $K = 2$ and $K = 3$ cases with a colored mask, and demonstrates that the reconstruction performance degrades gracefully at noisy regimes.

For comparison, we also obtain reconstructions from compressive measurements using ℓ_1 -norm based regularization which is explained in Section 4.3.1. We note that ℓ_0 -norm based reconstruction is not feasible for the earlier data set used for ℓ_1 -norm based reconstruction because it takes hours to reconstruct $256 \times 256 \times 10$ spectral cube. For this reason, here we provide the results of both reconstruction methods on



(a)



(b)

Figure 4.9: (a) Reconstructed images from compressive measurements ($K = 2$). Top to bottom: true images, reconstructions with no mask, uncolored mask, colored mask. (b) PSNR versus K for the colored mask case

$128 \times 128 \times 6$ spectral cube given here. For ℓ_1 -norm based reconstruction, we use 3D TV, 3D Full DCT, 3D Patched DCT, and 2D Symm + 1D DCT priors, which are explained in Section 4.4.1.1. PSNRs for these priors and ℓ_0 -norm based reconstruction are given in Table 4.8. It can be seen that 3D Patched DCT and 3D Full DCT priors in ℓ_1 -norm based regularization have similar PSNRs with ℓ_0 -norm based reconstruction using 3D Patched DCT prior. On the other hand, the ℓ_1 -norm based regularization utilizing ADMM converges much faster, around 30 seconds, while ℓ_0 -norm based regularization requires approximately 800 seconds.

Table 4.7: Comparison of average PSNRs (dB) for different compressive measurement scenarios and SNRs.

SNR (dB)	80% CR	70% CR	60% CR	50% CR
20	25.34	27.43	28.11	28.54
30	27.65	31.52	32.61	33.07
40	29.14	34.56	36.29	37.00

Table 4.8: Comparison of PSNRs (dB) of ℓ_0 -norm and ℓ_1 -norm based regularization methods for different compressive measurement scenarios and SNRs. Reconstruction results are given in the following SNR order: 20 dB, 30 dB, and infinite. For a given K and input SNR, methods with highest PSNR (within 0.1 dB margin) are given in bold numbers.

Method	K=2 (67% compression)	K=3 (50% compression)
(ℓ_1) 3D TV	28.50/31.06/35.30	29.20/32.60/37.64
(ℓ_1) 3D Full DCT	30.17/ 33.87 /38.25	31.11/ 35.53 /40.39
(ℓ_1) 3D Patched DCT	30.71/33.86/41.00	31.39/35.30/42.44
(ℓ_1) 2D Symm + 1D DCT	29.06/31.82/36.11	30.00/33.68/38.94
(ℓ_0) 3D Patched DCT	30.69/32.92/40.25	33.97/34.98/44.45

4.4.2.1 Effect of Different Transform Choices

Here we consider the effect of different sparsity priors on the performance of ℓ_0 -norm based reconstruction. For this, we solve the problem in Eq. (4.10) by changing the patch 3D DCT operator with full 3D DCT operator. In other words, instead of sparsifying the patches in the data cube separately, we apply 3D DCT transformation

to the full spectral cube at once. Then the related sparse code update step is applied for $\mathbf{W}\mathbf{x}$ where \mathbf{W} is the 3D DCT operator. Similarly, the matrix \mathbf{G} in Eq. (4.11) becomes the identity matrix, \mathbf{I} . We denote these two priors as *3D Patched DCT* and *3D Full DCT*, respectively.

We compare the performance of these priors when the input SNR is 20 dB and 30 dB. We set $K = 3$ and reconstruct 6 spectral bands of size 128×128 from 6 different spectral dataset. Spectral images with different characteristics are taken from [54] and their superimposed versions are illustrated in Fig. 4.10. We use the same photon sieve design parameters with the previous setting. Reconstruction times are given in Table 4.9 and demonstrate longer reconstruction times for 3D Patched DCT prior, as expected.

Table 4.10 shows average PSNR and SSIM values for different datasets and SNR levels. The results demonstrate that 3D Patched DCT prior provides higher PSNR and SSIM values in almost all cases. To visually evaluate the results, reconstructed images with both priors are given with the reference images for dataset #1 when SNR=30 dB. As can be seen, 3D Patched DCT prior preserves spatial and spectral properties while 3D Full DCT causes noisy artifacts. The results show that 3D Patched DCT is superior to 3D Full DCT in terms of reconstruction quality, while it requires a longer reconstruction time.

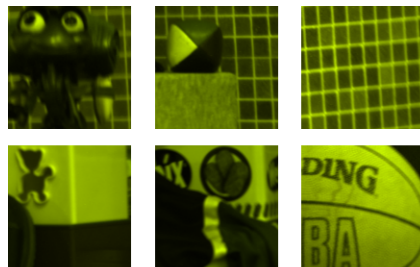


Figure 4.10: Spectral datasets with different spatial and spectral characteristics.

Table 4.9: Reconstruction times for different priors and input SNRs in seconds using ℓ_0 -norm based reconstruction method.

SNR (dB)	3D Full DCT	3D Patched DCT
20	697 s	1038 s
30	773 s	1449 s

Table 4.10: PSNR(dB)/SSIM values of different datasets for different priors and different input SNRs.

Dataset #	SNR (dB)	3D Full DCT	3D Patched DCT
1	20	25.5/0.63	33.2/0.93
	30	32.9/0.85	35.1/0.96
2	20	27.1/0.67	31.7/0.90
	30	30.9/0.83	34.4/0.95
3	20	29.9/0.89	29.2/0.94
	30	33.0/0.95	31.8/0.97
4	20	24.3/0.39	27.1/0.83
	30	30.5/0.74	31.4/0.89
5	20	27.1/0.59	33.2/0.92
	30	32.1/0.83	35.0/0.95
6	20	26.3/0.65	21.7/0.84
	30	28.2/0.77	31.4/0.91

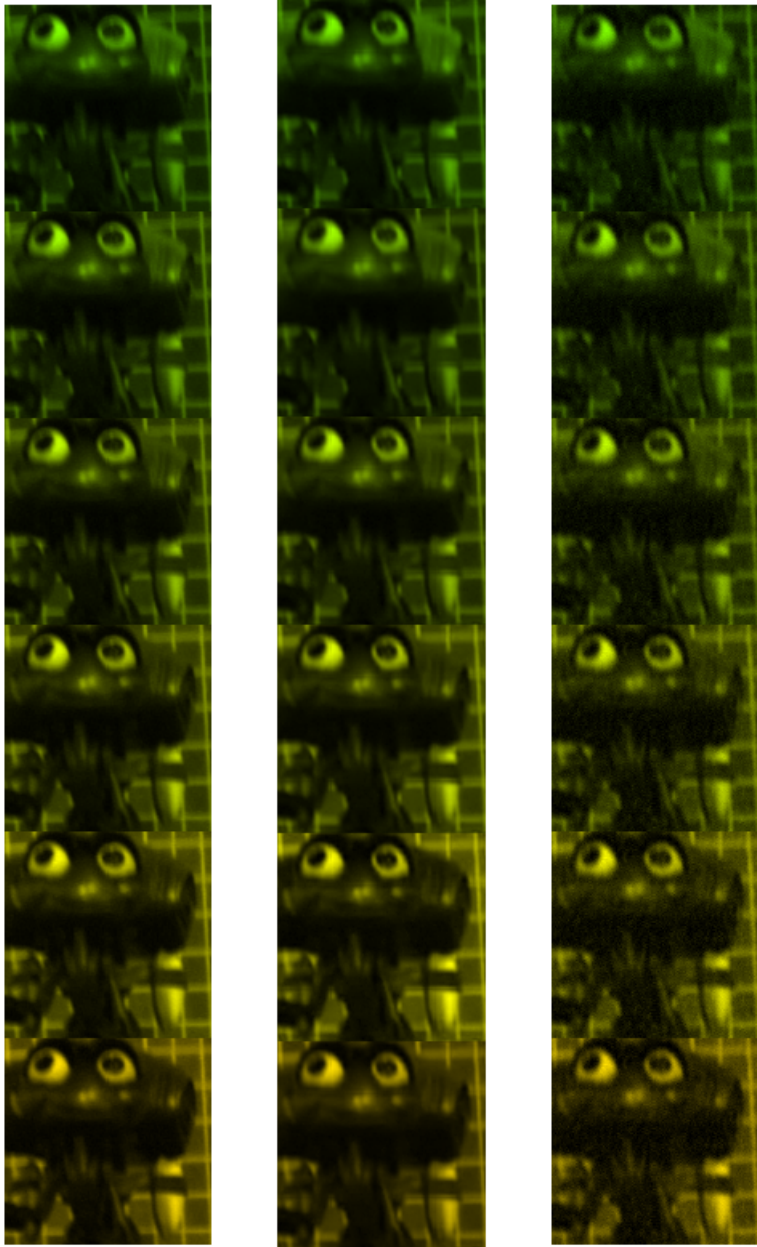


Figure 4.11: Reconstructed spectral images for dataset #1 when input SNR is 30 dB. Left to right: True images, 3D Patched DCT reconstruction, 3D Full DCT reconstruction.

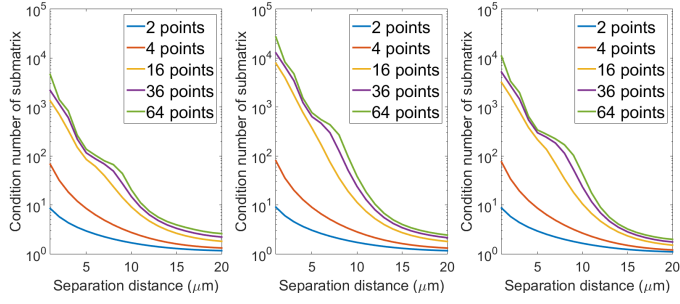
4.5 System Analysis

In this section, we analyze the compressive spectral imaging system described in Section 4.4.1 from different aspects. Specifically, we investigate its spatial and spectral resolution numerically and theoretically. Then, we provide a relation between the conditioning of system matrix and reconstruction quality as we change the measurement planes, which can be used as a tool for system optimization.

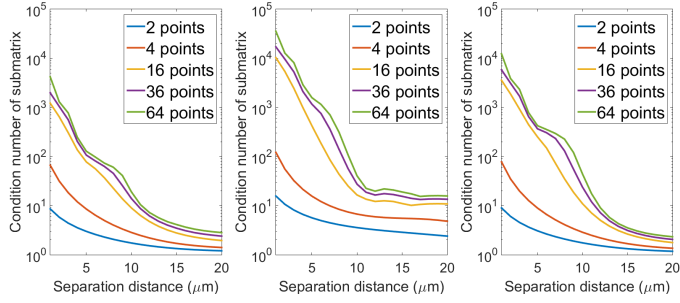
4.5.1 Spatial Resolution

Here we first perform a conditioning-based analysis to investigate the resolution of the proposed system. For this analysis, we investigate the stability of the forward model. Similar to Section 2.5.2, we consider point sources with 2, 4, 16, 36, and 64 elements placed in a square grid with varying separation distances. We choose the pixel size on the detector as $1\ \mu\text{m}$ for fine analysis. Separation distance between the point sources is changed from $1\ \mu\text{m}$ to $20\ \mu\text{m}$ with $1\ \mu\text{m}$ steps. Since we have 10 spectral bands, we place the point sources at the 1st, 5th, and 10th bands to observe the general behavior of the system. We then calculate the conditioning of the relevant submatrices of the system matrix \mathbf{HC} associated with the nonzero locations.

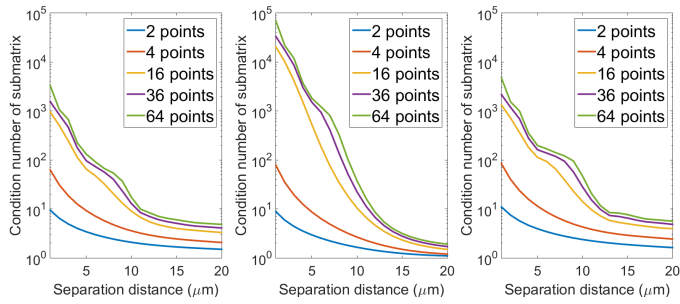
The results are plotted in Figures 4.12 when the CR values are 50%, 60%, 70%, and 80%, respectively. We note that the expected theoretical diffraction-limited spatial resolution is $15\ \mu\text{m}$. From the given plots, it can be seen that the conditioning is similar for all three bands and becomes worse as the number of point sources increases, which is an expected result. In addition, when the separation distance between the point sources decreases, conditioning of the system increases, which indicates that the system's resolving power degrades. A critical observation is the sharp decrease in the condition number until $15\ \mu\text{m}$, which then starts to change slowly for all cases. Although this trend is similar for all CR values, as CR increases, conditioning has higher values for a given separation distance. This observation is also in agreement with the fact that the system becomes more ill-posed as the CR increases. This illustrates that the resolution of the system becomes worse as the number of measurements decreases.



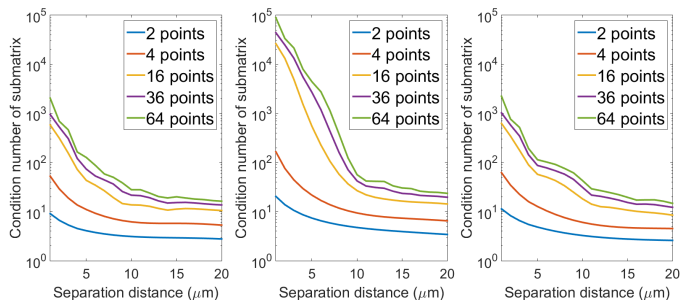
(a)



(b)



(c)



(d)

Figure 4.12: Conditioning of the submatrices of \mathbf{HC} for different number of point sources and different separation distances when CR is (a)-(d) 50%, 60%, 70%, and 80%, respectively. Left to right: conditioning results when the point sources are placed at the 1st, 5th, and 10th spectral bands.

To visually demonstrate the system resolution, we consider 16 point sources of size $1 \mu\text{m}$ placed at the first spectral band. The separation distance between the point sources is chosen as $15 \mu\text{m}$, and reconstructions are obtained for 30 dB input SNR when the CR values are 50%, 60%, 70%, and 80%, respectively. Figure 4.13 shows the ground truth, diffraction-limited, and reconstructed images at different CR values. As can be seen, the system resolves points with a separation of $15 \mu\text{m}$ successfully up to 70% CR. When CR is 80%, points at the outermost part are barely resolvable, showing that resolution degrades as the CR increases. The results also show that the proposed system provides sharper reconstructions than the diffraction-limited images.

To better understand the true resolution offered by the system, the separation distance between 16 point sources of size $1 \mu\text{m}$ is decreased from $15 \mu\text{m}$ to $8 \mu\text{m}$ with $1 \mu\text{m}$ steps. Reconstructions obtained for these point sources are given in Fig. 4.14 when CR is 50% and input SNR is 30 dB. The results demonstrate that the points are resolvable until the separation distance is decreased to $8 \mu\text{m}$, which indicates that the system can surpass the expected theoretical resolution of $15 \mu\text{m}$ at this CR and SNR level.

Finally, to observe the effect of input SNR on the resolution, we obtain reconstructions of 16 point sources of size $1 \mu\text{m}$ and separation $15 \mu\text{m}$ at different input SNRs. Fig. 4.15 shows reconstructions when CR is 50% and input SNR is decreased from 30 dB to 0 dB with 10 dB steps. The results show that the points are resolvable until 10 dB input SNR at this CR level, hence the system is robust to noise for a wide range of SNR levels.

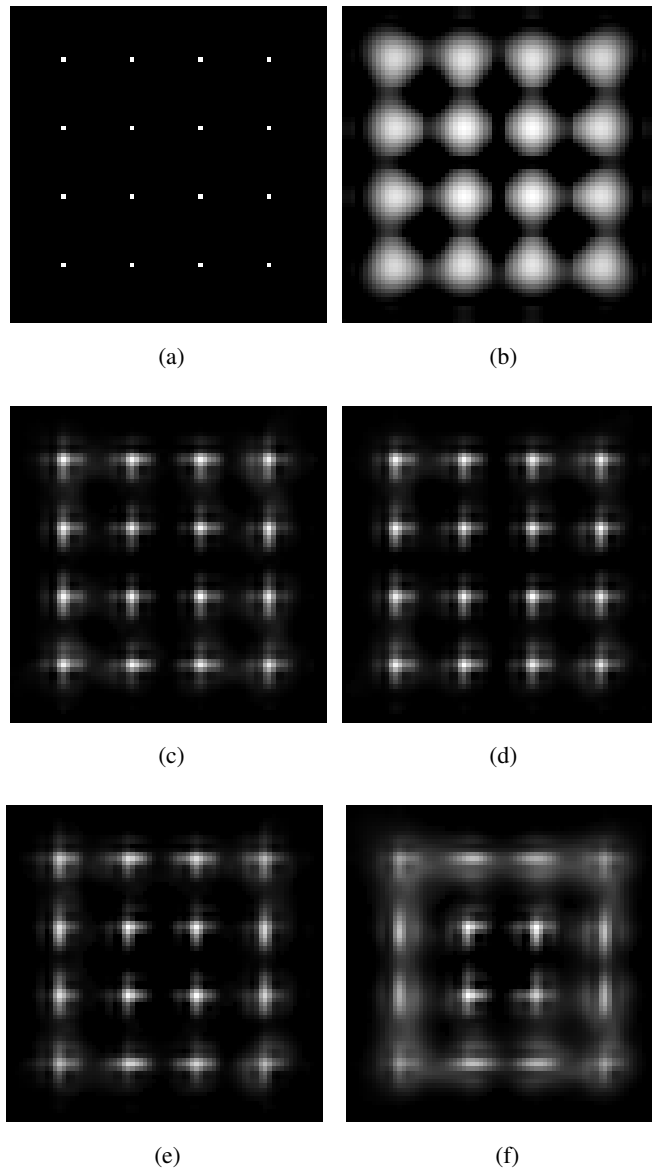


Figure 4.13: Demonstration of $15 \mu\text{m}$ resolution using 16 point targets for 30 dB SNR. (a) Ground truth image, (b) diffraction-limited image, (c)-(f) reconstructed images from the noisy measurements when CR is 50%, 60%, 70%, and 80%.

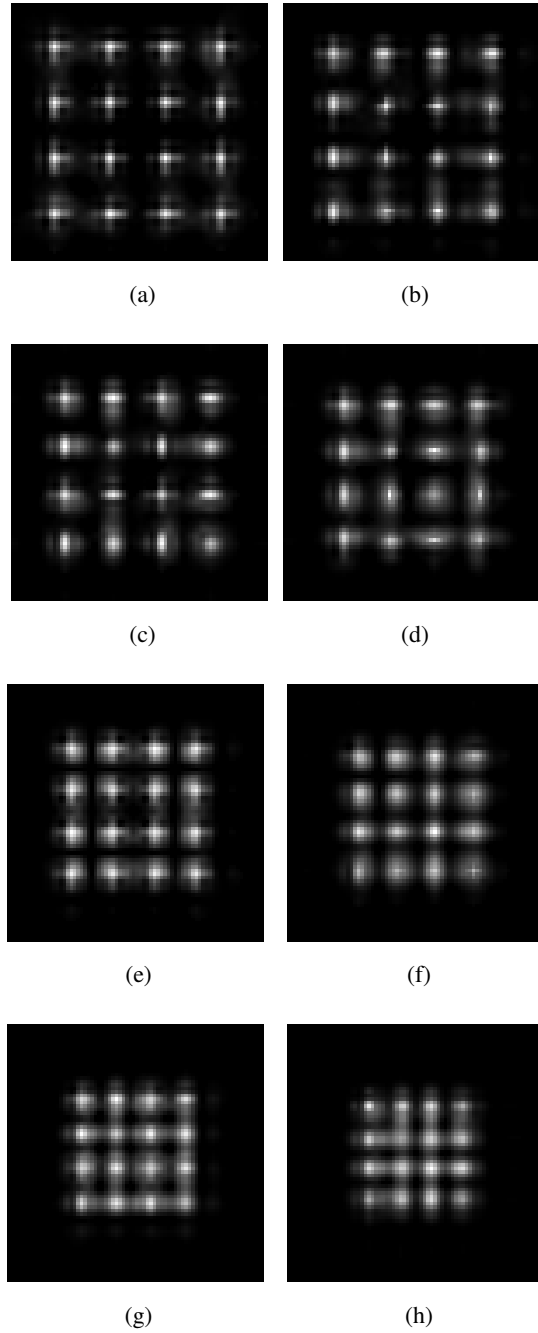


Figure 4.14: Demonstration of $15 \mu\text{m}$ to $8 \mu\text{m}$ resolution using 16 point targets for 30 dB SNR when CR is 50%. (a)-(h) Reconstructed images from the noisy measurements when the separation distance is decreased from $15 \mu\text{m}$ to $8 \mu\text{m}$ with $1 \mu\text{m}$ steps.

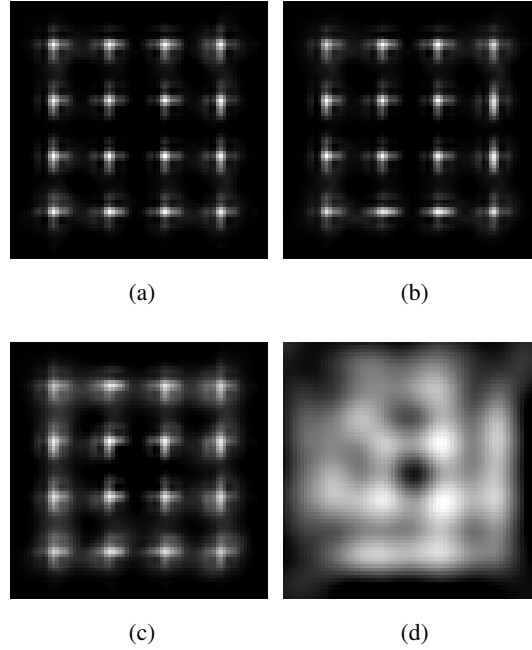


Figure 4.15: Demonstration of $15 \mu\text{m}$ resolution using 16 point targets for different input SNRs when CR is 50%. (a)-(d) Reconstructed images from the noisy measurements when the input SNR is decreased from 30 dB to 0 dB with 10 dB steps.

4.5.2 Spectral Resolution

Similar to spatial resolution, we perform a conditioning-based analysis for spectral resolution. For this analysis, we place point sources with 20 nm separation along spectral direction. In other words, point sources are located at $(i, i + 2)$ spectral pairs for $i = 1, \dots, 8$. We then calculate the conditioning of the relevant submatrices of the system matrix \mathbf{HC} associated with the nonzero locations. The results are plotted in Figures 4.16 when the CR values are 50%, 60%, 70%, and 80%, respectively. From these plots, it can be seen that conditioning is similar for all spectral band pairs and get worse as the CR increases. In other words, it becomes harder to resolve different spectral points when the number of measurements decreases. However, verifying these results through reconstructions is harder than the spatial resolution case. This is because we exploit the fact that the spectral cube exhibits correlation along the spectral dimension, and formulate the inverse problem using this correlation. As a

result, the reconstruction will inevitably fail for the point sources along the spectral dimension. Instead of this, calculating NMSE of the reconstructed spectrum at various points in the spectral cube provides more insight about the spectral resolution of the system, as we have done in Section 4.4.1.

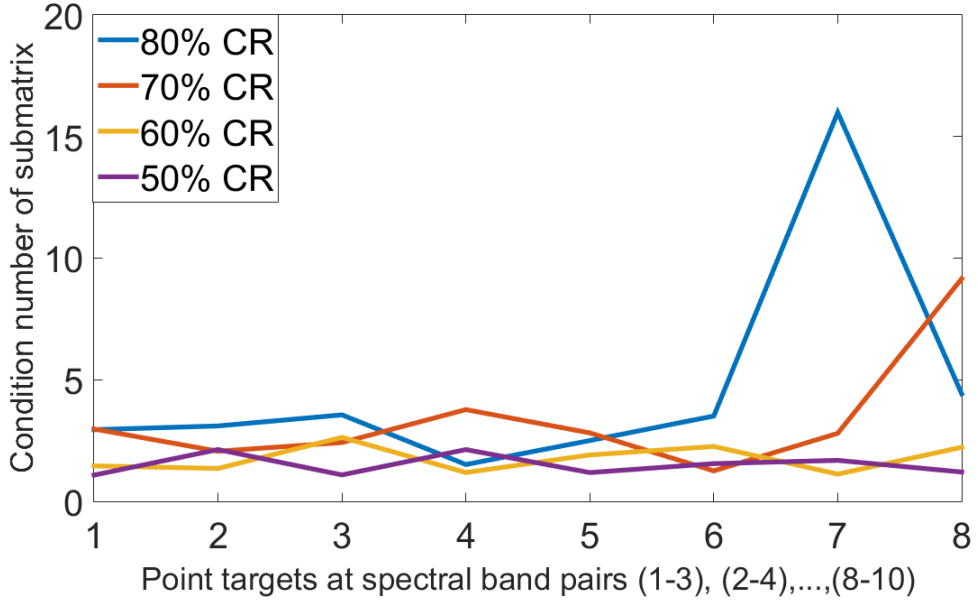


Figure 4.16: Conditioning of the submatrices \mathbf{HC} for 2 point sources placed at every $(i, i + 2)$ spectral pairs, $i = 1, \dots, 8$ when the CR values are 50%, 60%, 70%, and 80%, respectively.

4.5.3 Measurement Plane Optimization

The choice of measurement planes (MP) correctly has a crucial role in the successful reconstruction of the spectral data cube from compressive measurements. Here we present a conditioning-based analysis based on the conditioning of the overall system matrix \mathbf{HC} for different measurement plane choices. The main goal is to find a design optimality metric that is independent of SNR, unknown spectral cube characteristics, and reconstruction choices. The analysis is performed in a lower-dimensional grid than the original dimension of the problem because forming the larger matrices and computing their singular values are not practical. Here we show that performing the conditioning-based analysis for a significantly smaller problem still provides impor-

tant information about measurement plane optimization.

For this analysis, we consider a data cube of size $32 \times 32 \times 10$ and form the overall system matrix \mathbf{HC} for this input size. Then we calculate the first 2500 singular values of the system matrix using an iterative solver [87] for 10 different measurement plane selections when the CR is 50%. These selections are reported in Table 4.11 in a normalized grid, $(0.0, 1.0)$. Specifically, the focal distance of the largest wavelength λ_{10} , i.e. f_{10} , is denoted as 0.0 while the focal distance of the shortest wavelength λ_1 , i.e. f_1 , is denoted as 1.0. After this, all the measurement plane locations are chosen between $(0.0, 1.0)$. Note that MP-10 in Table 4.11 corresponds to the measurement planes used in the previous results for 50% CR. Normalized 2500 largest singular values of the matrix \mathbf{HC} for these MP choices are given in Fig. 4.17 together with their zoomed-in versions. From the given singular value plots, it can be seen that the singular values of MP-8 setting decay faster than other MPs while MP-6 has the slowest decay.

Intuitively, we expect that spreading the measurement locations between 0.0 and 1.0 should provide a better conditioning. This is in agreement with the singular value plots of MP-1, MP-2, MP-3, MP-4, MP-5, and MP-10. All of these MP choices have similar spreads confined in a narrow region. Conversely, MP-7 and MP-8 obtain measurements only from the half portion of the overall range, which results in a quick decay in the singular value distribution, as expected. Finally, MP-9 focuses on the central portion of the overall range and does not contain both extreme ends, which also results in a fast decaying singular value distribution.

Table 4.11: Different measurement plane selections normalized between f_{10} and f_1 .

Measurement Plane No	Normalized Locations of 5 measurement planes
MP-1	[0.20 0.40 0.60 0.80 1.00]
MP-2	[0.10 0.30 0.50 0.70 0.90]
MP-3	[0.00 0.20 0.40 0.60 0.80]
MP-4	[0.00 0.30 0.50 0.70 1.00]
MP-5	[0.00 0.20 0.50 0.80 1.00]
MP-6	[0.05 0.25 0.50 0.75 0.95]
MP-7	[0.00 0.10 0.20 0.30 0.40]
MP-8	[0.60 0.70 0.80 0.90 1.00]
MP-9	[0.30 0.40 0.50 0.60 0.70]
MP-10	[0.00 0.25 0.50 0.75 1.00]

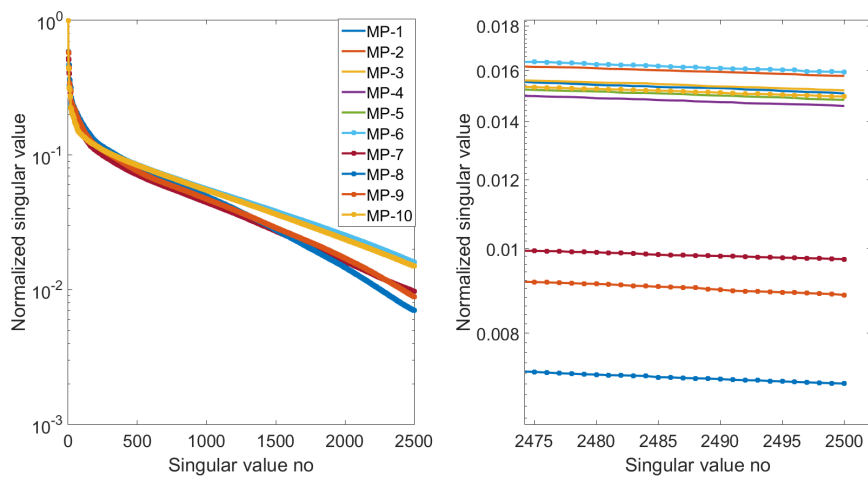


Figure 4.17: Normalized 2500 largest singular values of HC matrix for the MP selections in Table 4.11. Zoomed-in version is given at right.

Now we investigate the relation between the singular value distribution and the reconstruction quality. For this, we reconstruct data cubes of size $32 \times 32 \times 10$, $64 \times 64 \times 10$, and $256 \times 256 \times 10$ using these 10 different MP choices for 40 dB input SNR. In all of the MP selections we calculate the ratio $\frac{\sigma_{min}}{\sigma_{max}}$ where σ_{min} is the smallest singular value and σ_{max} is the largest singular value. We expect the ratio $\frac{\sigma_{min}}{\sigma_{max}}$ to be related to the reconstruction quality, which we evaluate using the PSNR metric. The results are plotted in Fig. 4.18 and are in agreement with our expectations. Specifically, both the ratio $\frac{\sigma_{min}}{\sigma_{max}}$ and PSNR are the highest for MP-6 and the lowest for MP-8. Moreover, although the ratio $\frac{\sigma_{min}}{\sigma_{max}}$ is calculated for $32 \times 32 \times 10$ data cube size, the results are still consistent with the reconstructions of higher dimensional inputs of size $64 \times 64 \times 10$ and $256 \times 256 \times 10$. This suggests that the optimization of the measurement plane locations can be done by calculating the singular values in a lower-dimensional setting than the original problem size, which is more memory-efficient.

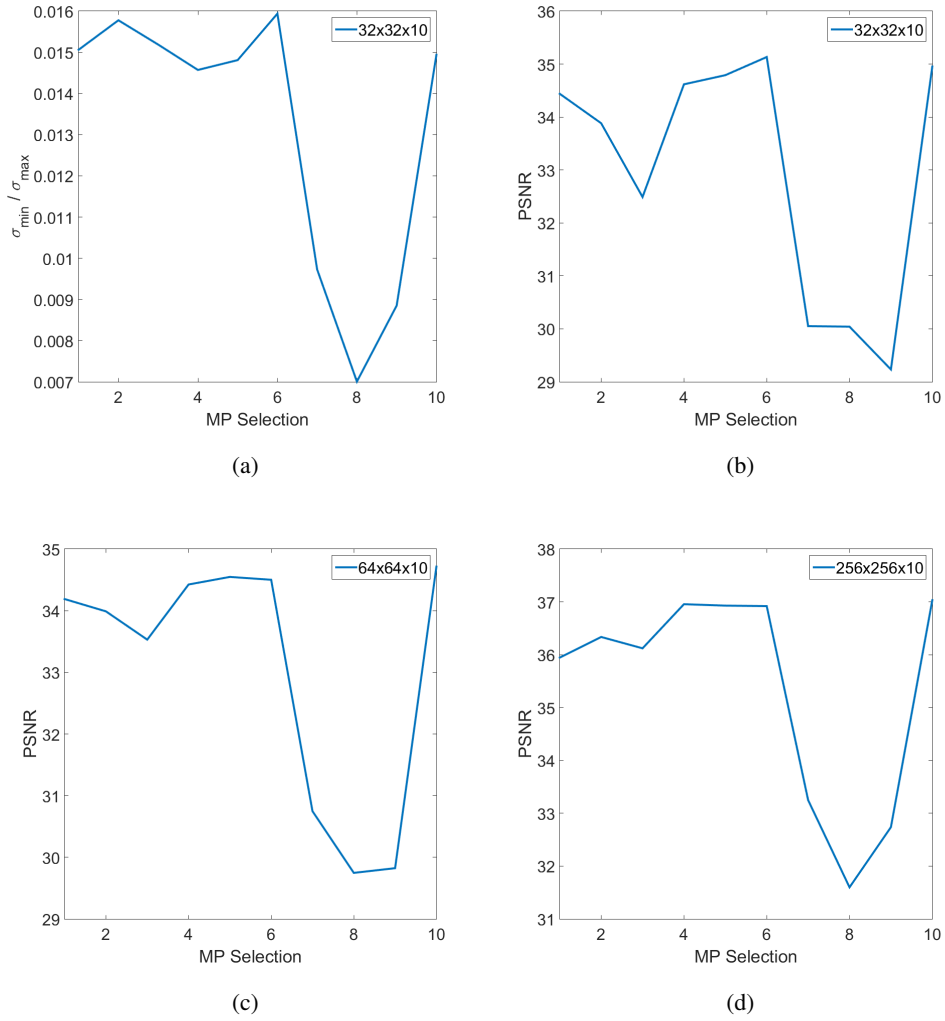


Figure 4.18: (a) The ratio $\frac{\sigma_{\min}}{\sigma_{\max}}$ for different MP selections when input size is $32 \times 32 \times 10$. PSNRs for these MP selections when input SNR is 40 dB and input size is (b) $32 \times 32 \times 10$, (c) $64 \times 64 \times 10$, and (d) $256 \times 256 \times 10$, respectively.

4.6 Conclusions

Compressive spectral imaging enables to reconstruct the entire three-dimensional (3D) spectral cube from a few multiplexed images. In this chapter, we have developed a novel compressive spectral imaging technique using diffractive lenses. Our technique uses a coded aperture to spatially modulate the optical field from the scene

and a diffractive lens such as a photon sieve for dispersion. The coded field is passed through the diffractive lens and then measured at a few planes using a monochrome detector. The 3D spectral cube is then reconstructed from these highly compressed measurements through sparse recovery. For this, we have developed two fast sparse recovery methods, namely ℓ_1 -norm based regularization and ℓ_0 -norm based regularization, to solve this large-scale inverse problem. The imaging performance is illustrated at the visible regime for various scenarios with different compression ratios through numerical simulations. The results demonstrate that promising reconstruction performance can be achieved with as little as two measurements. Finally, we have provided an analysis for the spatio-spectral resolution of the system and measurement plane optimization using both numerical and theoretical tools.

Since the system takes compressive measurements along the spectral dimension, successful reconstructions can be achieved for spectrally-correlated scenes at the visible and infrared regimes. Different than the earlier compressive spectral imaging techniques that rely on prisms or gratings to disperse the optical field and many lenses to form images, here a single diffractive lens is used for both purposes. Calibration of the system also appears to be simpler because the imaging system is shift-invariant and measuring the PSFs is sufficient, instead of the system response for each voxel. Hence the presented work opens up new possibilities for high-resolution spectral imaging with low-cost and simple designs.

In the presented results, the pixel size of the detector, as well as the reconstruction grid, are chosen to match the expected spatial resolution of the diffractive lens. Because the developed imaging modality is a computational imaging technique and the compression is performed along the spectral direction, the effective spectral resolution not only depends on the spectral bandwidth of the diffractive lens but also on the scene content (mainly, its spectral correlation). Although the imaging performance appears to be robust to higher compression levels and noise, clearly increasing the number of measurements improves the reconstructions. However, this comes with the cost of increased acquisition time, which may be undesirable for dynamic scenes. The reconstructions can be further improved with the optimization of coded apertures and learning-based recovery.

CHAPTER 5

CONCLUSIONS

In this thesis, we have focused on three important tasks in spectral imaging: fast and programmable multi-spectral imaging in Chapter 2, spatial super-resolution in Chapter 3, and compressive spectral imaging in Chapter 4. For each task, we have developed novel imaging modalities that utilize diffractive lenses. Then, we have presented novel reconstruction methods to solve the resulting inverse problems. The methods are based on the alternating direction method of multipliers (ADMM) which is a state of the art technique in signal recovery problems. Finally, we have numerically illustrated the reconstruction performance for various settings.

For the fast and programmable multi-spectral imaging task, we have first studied a high-resolution computational imaging modality. This technique uses a diffractive lens such as a photon sieve for dispersing the optical field and takes measurements at different distances from the sieve using a moving detector, which may be undesirable in dynamic scenes. To avoid this, we have proposed to take measurements at a fixed plane by using multiple photon sieves with beam splitters or programmable spatial light modulators (SLM). We have developed an ADMM based fast sparse recovery method to solve the associated large-scale inverse problems for both modalities. We have also presented an efficient implementation of the proposed method, which requires no matrix formation and takes a few minutes on a standard computer.

We have investigated the performance of the proposed system in EUV and visible band spectral imaging for a different number of sources and input SNRs. We have obtained promising results in terms of PSNR, SSIM, and visual quality. We have also demonstrated that the proposed system has almost the same performance as the original one. Thus, they can be used interchangeably without sacrificing the reconstruction

quality. After this, we have provided an analysis of the spatial resolution of the system using both theoretical and numerical tools. To do this, first, a conditioning-based analysis has been performed to understand the stability of the forward model. Then, we have reconstructed point sources with different configurations and compared the results with the theoretical findings. We have shown that the numerical results are in agreement with the theoretical expectations, and the system provides the expected theoretical diffraction-limited spatial resolution and even beyond for a wide range of SNR levels. Also, the system enables high spectral resolution in the EUV regime that is not possible with the state of the art EUV wavelength filters.

In the next chapter, we have dealt with the spatial super-resolution problem. Current spectral imaging systems, both computational imaging based and conventional ones, have hardware constraints which limit their spatial resolution. To overcome this limitation, we have proposed a spatial super-resolution technique for the diffractive lens based spectral imaging system with a low-resolution detector. We have developed an ADMM based reconstruction method which utilizes anisotropic 2D-TV and 3D-TV regularizers for different spectrum characteristics. We have illustrated the performance of the proposed technique using simulations for various scenarios at EUV and visible regimes. We have shown that this system can provide 2×2 super-resolution successfully based on PSNR, SSIM, and visual quality. However, the performance of the system degrades at higher super-resolution levels.

To achieve higher super-resolution levels, we have extended this technique by adding a coded aperture to the imaging system. This aperture spatially modulates the optical field before dispersion to obtain more incoherent measurements, as dictated by the CS theory. We have shown that this system enables 4×4 super-resolution by taking 4 or 8 shots. The system can also be used in dynamic scenes by utilizing off-the-shelf SLMs, which provides frame rates up to 1 kHz.

Lastly, we have presented a novel compressive spectral imaging technique using diffractive lenses. This technique uses a fixed coded aperture to spatially modulate the optical field from the scene and a diffractive lens such as photon sieve for dispersion. The coded field is passed through the diffractive lens and then measured at a few planes using a monochrome detector. The 3D spectral cube is then reconstructed

from these highly compressed measurements through sparse recovery. We have developed two fast sparse recovery methods, namely ℓ_1 -norm based regularization and ℓ_0 -norm based regularization, to solve this large-scale inverse problem.

We have illustrated the compressive spectral imaging performance at the visible regime for various scenarios with different compression ratios. The results demonstrate that promising reconstruction performance can be achieved with few measurements. Next, we have compared both recovery methods in terms of reconstruction time and quality. While their performances based on PSNR and SSIM are similar, the first method is significantly faster than the latter. After this, we have presented an analysis of the spatio-spectral resolution of the system using conditioning, as we have done in Chapter 2. We have found that the proposed system provides high spatial and spectral resolution that is robust to noise and in agreement with the theoretical expectations. Finally, we have shown that the optimization of measurement plane locations can be done by calculating singular values in a lower-dimensional setting than the original problem size, which is more memory-efficient.

As future work, in all of the above imaging modalities, the reconstructions can be further improved with the use of adaptive sparsity priors and learning-based recovery. Another critical part is the optimization of coded apertures for spatial super-resolution and compressive spectral imaging tasks, which will enable better system matrices satisfying CS requirements.

REFERENCES

- [1] G. G. Shepherd, *Spectral imaging of the atmosphere*, vol. 82. Academic Press, 2002.
- [2] F. S. Oktem, L. Gao, and F. Kamalabadi, “Computational spectral and ultrafast imaging via convex optimization,” in *Handbook of Convex Optimization Methods in Imaging Science*, pp. 105–127, Springer, 2017.
- [3] Q. Li, X. He, Y. Wang, H. Liu, D. Xu, and F. Guo, “Review of spectral imaging technology in biomedical engineering: achievements and challenges,” *Journal of Biomedical Optics*, vol. 18, no. 10, p. 100901, 2013.
- [4] G. Arce, D. Brady, L. Carin, H. Arguello, and D. Kittle, “Compressive coded aperture spectral imaging: An introduction,” *IEEE Signal Processing Magazine*, vol. 31, no. 1, pp. 105–115, 2014.
- [5] R. Willett, M. Duarte, M. Davenport, and R. Baraniuk, “Sparsity and structure in hyperspectral imaging: Sensing, reconstruction, and target detection,” *IEEE Signal Processing Magazine*, vol. 31, no. 1, pp. 116–126, 2014.
- [6] F. S. Oktem, F. Kamalabadi, and J. M. Davila, “A parametric estimation approach to instantaneous spectral imaging,” *IEEE Transactions on Image Processing*, vol. 23, no. 12, pp. 5707–5721, 2014.
- [7] R. G. Baraniuk, “Compressive sensing,” *IEEE Signal Processing Magazine*, vol. 24, no. 4, 2007.
- [8] E. J. Candès and M. B. Wakin, “An introduction to compressive sampling,” *IEEE Signal Processing Magazine*, vol. 25, no. 2, pp. 21–30, 2008.
- [9] M. E. Gehm, R. John, D. J. Brady, R. M. Willett, and T. J. Schulz, “Single-shot compressive spectral imaging with a dual-disperser architecture,” *Optics Express*, vol. 15, no. 21, pp. 14013–14027, 2007.

- [10] A. Wagadarikar, R. John, R. Willett, and D. Brady, “Single disperser design for coded aperture snapshot spectral imaging,” *Applied Optics*, vol. 47, no. 10, pp. B44–B51, 2008.
- [11] Y. August, C. Vachman, Y. Rivenson, and A. Stern, “Compressive hyperspectral imaging by random separable projections in both the spatial and the spectral domains,” *Applied Optics*, vol. 52, no. 10, pp. D46–D54, 2013.
- [12] X. Lin, G. Wetzstein, Y. Liu, and Q. Dai, “Dual-coded compressive hyperspectral imaging,” *Optics Letters*, vol. 39, no. 7, pp. 2044–2047, 2014.
- [13] S. Boyd, N. Parikh, E. Chu, B. Peleato, J. Eckstein, *et al.*, “Distributed optimization and statistical learning via the alternating direction method of multipliers,” *Foundations and Trends in Machine Learning*, vol. 3, no. 1, pp. 1–122, 2011.
- [14] P. Wang and R. Menon, “Computational multispectral video imaging,” *JOSA A*, vol. 35, no. 1, pp. 189–199, 2018.
- [15] F. D. Hallada, A. L. Franz, and M. R. Hawks, “Fresnel zone plate light field spectral imaging,” *Optical Engineering*, vol. 56, no. 8, p. 081811, 2017.
- [16] M. Nimmer, G. Steidl, R. Riesenberger, and A. Wuttig, “Spectral imaging based on 2d diffraction patterns and a regularization model,” *Optics Express*, vol. 26, no. 22, pp. 28335–28348, 2018.
- [17] O. F. Kar and F. S. Oktem, “Fast computational spectral imaging with a programmable diffractive lens,” in *Computational Optical Sensing and Imaging*, Optical Society of America, 2019.
- [18] F. S. Oktem, O. F. Kar, and F. Kamalabadi, “High-resolution computational multi-spectral imaging using diffractive lenses,” submitted.
- [19] H. Rueda, D. Lau, and G. R. Arce, “Multi-spectral compressive snapshot imaging using rgb image sensors,” *Optics Express*, vol. 23, no. 9, pp. 12207–12221, 2015.
- [20] H. Arguello and G. R. Arce, “Colored coded aperture design by concentration of measure in compressive spectral imaging,” *IEEE Transactions on Image Processing*, vol. 23, no. 4, pp. 1896–1908, 2014.

- [21] T.-H. Tsai, P. Llull, X. Yuan, L. Carin, and D. J. Brady, “Spectral-temporal compressive imaging,” *Optics Letters*, vol. 40, no. 17, pp. 4054–4057, 2015.
- [22] F. S. Oktem, F. Kamalabadi, and J. M. Davila, “High-resolution computational spectral imaging with photon sieves,” in *IEEE Int. Conf. on Image Processing (ICIP)*, pp. 5122–5126, IEEE, 2014.
- [23] S. K. Sahoo, D. Tang, and C. Dang, “Single-shot multispectral imaging with a monochromatic camera,” *Optica*, vol. 4, no. 10, pp. 1209–1213, 2017.
- [24] C. Ma, X. Cao, X. Tong, Q. Dai, and S. Lin, “Acquisition of high spatial and spectral resolution video with a hybrid camera system,” *International Journal of Computer Vision*, vol. 110, no. 2, pp. 141–155, 2014.
- [25] X. Cao, T. Yue, X. Lin, S. Lin, X. Yuan, Q. Dai, L. Carin, and D. J. Brady, “Computational snapshot multispectral cameras: toward dynamic capture of the spectral world,” *IEEE Signal Processing Magazine*, vol. 33, no. 5, pp. 95–108, 2016.
- [26] L. Kipp, M. Skibowski, R. Johnson, R. Berndt, R. Adelung, S. Harm, and R. Seemann, “Sharper images by focusing soft x-rays with photon sieves,” *Nature*, vol. 414, no. 6860, pp. 184–188, 2001.
- [27] D. Attwood, *Soft x-rays and extreme ultraviolet radiation: principles and applications*. Cambridge University Press, Cambridge, 2000.
- [28] P. Gorenstein, J. D. Phillips, and R. D. Reasenberg, “Refractive/diffractive telescope with very high angular resolution for X-ray astronomy,” in *Proc. SPIE*, vol. 5900, pp. 590018–590018, 2005.
- [29] J. Davila, “High-resolution solar imaging with a photon sieve,” in *SPIE Optical Engineering+ Applications*, pp. 81480O–81480O, International Society for Optics and Photonics, 2011.
- [30] R. E. Blahut, *Theory of remote image formation*. Cambridge University Press, Cambridge, 2004.
- [31] F. S. Oktem, F. Kamalabadi, and J. M. Davila, “Analytical fresnel imaging models for photon sieves,” *Optics Express*, vol. 26, no. 24, pp. 32259–32279, 2018.

- [32] P. C. Hansen, *Discrete Inverse Problems: Insight and Algorithms*, vol. 7. SIAM, 2010.
- [33] A. N. Tikhonov and V. I. Arsenin, *Solutions of ill-posed problems*, vol. 14. Vh Winston, 1977.
- [34] H. W. Engl, M. Hanke, and A. Neubauer, *Regularization of inverse problems*, vol. 375. Springer Science & Business Media, 1996.
- [35] M. Bertero and P. Boccacci, *Introduction to inverse problems in imaging*. CRC press, 1998.
- [36] J. Kaipio and E. Somersalo, *Statistical and computational inverse problems*, vol. 160. Springer Science & Business Media, 2006.
- [37] S. Geman and D. Geman, “Stochastic relaxation, gibbs distributions, and the bayesian restoration of images,” in *Readings in Computer Vision*, pp. 564–584, Elsevier, 1987.
- [38] M. V. Afonso, J. M. Bioucas-Dias, and M. A. T. Figueiredo, “An augmented lagrangian approach to the constrained optimization formulation of imaging inverse problems,” *IEEE Transactions on Image Processing*, vol. 20, no. 3, pp. 681–695, 2011.
- [39] L. I. Rudin, S. Osher, and E. Fatemi, “Nonlinear total variation based noise removal algorithms,” *Physica D: Nonlinear Phenomena*, vol. 60, no. 1-4, pp. 259–268, 1992.
- [40] T. Chan, S. Esedoglu, F. Park, and A. Yip, “Recent developments in total variation image restoration,” *Mathematical Models of Computer Vision*, vol. 17, no. 2, 2005.
- [41] A. N. Tikhonov, “Solution of incorrectly formulated problems and the regularization method,” *Soviet Math.*, vol. 4, pp. 1035–1038, 1963.
- [42] C. R. Vogel, *Computational methods for inverse problems*, vol. 23. SIAM, 2002.
- [43] A. Chambolle, “An algorithm for total variation minimization and applications,” *Journal of Mathematical Imaging and Vision*, vol. 20, no. 1-2, pp. 89–97, 2004.

- [44] S. J. Wright, R. D. Nowak, and M. A. Figueiredo, “Sparse reconstruction by separable approximation,” *IEEE Transactions on Signal Processing*, vol. 57, no. 7, pp. 2479–2493, 2009.
- [45] M. V. Afonso, J. M. Bioucas-Dias, and M. A. Figueiredo, “Fast image recovery using variable splitting and constrained optimization,” *IEEE Transactions on Image Processing*, vol. 19, no. 9, pp. 2345–2356, 2010.
- [46] M. K. Ng, P. Weiss, and X. Yuan, “Solving constrained total-variation image restoration and reconstruction problems via alternating direction methods,” *SIAM Journal on Scientific Computing*, vol. 32, no. 5, pp. 2710–2736, 2010.
- [47] J. Nocedal and S. Wright, *Numerical optimization*. Springer Science & Business Media, 2006.
- [48] U. Kamaci, F. C. Akyon, T. Alkanat, and F. S. Oktem, “Efficient sparsity-based inversion for photon-sieve spectral imagers with transform learning,” in *2017 IEEE Global Conference on Signal and Information Processing (GlobalSIP)*, pp. 1225–1229, IEEE, 2017.
- [49] B. Noble and J. W. Daniel, *Applied linear algebra*, vol. 3. Prentice-Hall New Jersey, 1988.
- [50] H. H. Bauschke, P. L. Combettes, *et al.*, *Convex analysis and monotone operator theory in Hilbert spaces*, vol. 408. Springer, 2011.
- [51] J. W. Goodman, *Introduction to Fourier Optics*. Englewood, Colorado: Roberts, 3 ed., 2005.
- [52] R. Menon, D. Gil, G. Barbastathis, and H. I. Smith, “Photon-sieve lithography,” *JOSA A*, vol. 22, no. 2, pp. 342–345, 2005.
- [53] N. Antipa, G. Kuo, R. Heckel, B. Mildenhall, E. Bostan, R. Ng, and L. Waller, “Diffusercam: lensless single-exposure 3d imaging,” *Optica*, vol. 5, no. 1, pp. 1–9, 2018.
- [54] S. M. Nascimento, F. P. Ferreira, and D. H. Foster, “Statistics of spatial cone-excitation ratios in natural scenes,” *JOSA A*, vol. 19, no. 8, pp. 1484–1490, 2002.

- [55] J. R. Lemen, A. M. Title, D. J. Akin, P. F. Boerner, C. Chou, J. F. Drake, D. W. Duncan, C. G. Edwards, F. M. Friedlaender, G. F. Heyman, *et al.*, “The atmospheric imaging assembly (AIA) on the solar dynamics observatory (SDO),” *Solar Physics*, pp. 1–24, 2011.
- [56] K. Krapels, R. G. Driggers, E. Jacobs, S. Burks, and S. Young, “Characteristics of infrared imaging systems that benefit from superresolution reconstruction,” *Applied Optics*, vol. 46, no. 21, pp. 4594–4603, 2007.
- [57] A. Rogalski, “Fundamentals of infrared detector technologies,” *Taylor & Francis*, vol. 51, pp. 76600M–76600M, 2009.
- [58] R. M. Willett, R. F. Marcia, and J. M. Nichols, “Compressed sensing for practical optical imaging systems: a tutorial,” *Optical Engineering*, vol. 50, no. 7, pp. 072601–072601, 2011.
- [59] N. Akhtar, F. Shafait, and A. Mian, “Sparse spatio-spectral representation for hyperspectral image super-resolution,” in *European Conference on Computer Vision*, pp. 63–78, Springer, 2014.
- [60] M. Simões, J. Bioucas-Dias, L. B. Almeida, and J. Chanussot, “A convex formulation for hyperspectral image superresolution via subspace-based regularization,” *IEEE Transactions on Geoscience and Remote Sensing*, vol. 53, no. 6, pp. 3373–3388, 2015.
- [61] C. Kwan, J. H. Choi, S. Chan, J. Zhou, and B. Budavari, “Resolution enhancement for hyperspectral images: A super-resolution and fusion approach,” in *IEEE International Conference on Acoustics, Speech and Signal Processing (ICASSP)*, pp. 6180–6184, IEEE, 2017.
- [62] G. Licciardi, M. A. Veganzones, M. Simoes, J. Bioucas, and J. Chanussot, “Super-resolution of hyperspectral images using local spectral unmixing,” in *6th Workshop on Hyperspectral Image and Signal Processing: Evolution in Remote Sensing (WHISPERS)*, pp. 1–4, IEEE, 2014.
- [63] H. Huang, A. G. Christodoulou, and W. Sun, “Super-resolution hyperspectral imaging with unknown blurring by low-rank and group-sparse modeling,” in

- IEEE International Conference on Image Processing (ICIP)*, pp. 2155–2159, IEEE, 2014.
- [64] S. He, H. Zhou, Y. Wang, W. Cao, and Z. Han, “Super-resolution reconstruction of hyperspectral images via low rank tensor modeling and total variation regularization,” in *IEEE International Geoscience and Remote Sensing Symposium (IGARSS)*, pp. 6962–6965, IEEE, 2016.
- [65] T. Akgun, Y. Altunbasak, and R. M. Mersereau, “Super-resolution reconstruction of hyperspectral images,” *IEEE Transactions on Image Processing*, vol. 14, no. 11, pp. 1860–1875, 2005.
- [66] Y. Zhao, J. Yang, Q. Zhang, L. Song, Y. Cheng, and Q. Pan, “Hyperspectral imagery super-resolution by sparse representation and spectral regularization,” *EURASIP Journal on Advances in Signal Processing*, vol. 2011, no. 1, p. 87, 2011.
- [67] H. Arguello, H. F. Rueda, and G. R. Arce, “Spatial super-resolution in coded aperture spectral imaging,” in *Compressive Sensing*, vol. 8365, p. 83650A, International Society for Optics and Photonics, 2012.
- [68] E. Salazar, A. Parada, and G. R. Arce, “Spatial super-resolution reconstruction via sscsi compressive spectral imagers,” in *Computational Optical Sensing and Imaging*, pp. CTu5D–5, Optical Society of America, 2018.
- [69] R. Menon, D. Gil, G. Barbastathis, and H. I. Smith, “Photon-sieve lithography,” *J. Opt. Soc. Am. A*, vol. 22, no. 2, pp. 342–345, 2005.
- [70] G. Andersen, “Large optical photon sieve,” *Optics Letters*, vol. 30, no. 22, pp. 2976–2978, 2005.
- [71] F. S. Oktem, J. M. Davila, and F. Kamalabadi, “Image formation model for photon sieves,” in *IEEE Int. Conf. on Image Processing (ICIP)*, pp. 2373–2377, IEEE, 2013.
- [72] K. Nasrollahi and T. B. Moeslund, “Super-resolution: a comprehensive survey,” *Machine Vision and Applications*, vol. 25, no. 6, pp. 1423–1468, 2014.

- [73] H. Arguello and G. R. Arce, “Colored coded aperture design by concentration of measure in compressive spectral imaging,” *IEEE Transactions on Image Processing*, vol. 23, no. 4, pp. 1896–1908, 2014.
- [74] P. C. Hansen, *Discrete inverse problems: insight and algorithms*, vol. 7. SIAM, 2010.
- [75] C. R. Vogel and M. E. Oman, “Fast, robust total variation-based reconstruction of noisy, blurred images,” *IEEE Transactions on Image Processing*, vol. 7, no. 6, pp. 813–824, 1998.
- [76] D. Geman and C. Yang, “Nonlinear image recovery with half-quadratic regularization,” *IEEE Transactions on Image Processing*, vol. 4, no. 7, pp. 932–946, 1995.
- [77] J. M. Davila, “Slitless solar spectroscopy,” in *AAS/Solar Physics Division Meeting*, vol. 42, 2011.
- [78] A. Rajwade, D. Kittle, T.-H. Tsai, D. Brady, and L. Carin, “Coded hyperspectral imaging and blind compressive sensing,” *SIAM Journal on Imaging Sciences*, vol. 6, no. 2, pp. 782–812, 2013.
- [79] O. F. Kar, U. Kamaci, F. C. Akyon, and F. S. Oktem, “Compressive photon-sieve spectral imaging,” in *Computational Optical Sensing and Imaging*, pp. CTu5D–8, Optical Society of America, 2018.
- [80] O. F. Kar, F. S. Oktem, U. Kamaci, and F. Ç. Akyön, “Effect of different sparsity priors on compressive photon-sieve spectral imaging,” in *2018 26th Signal Processing and Communications Applications Conference (SIU)*, pp. 1–4, IEEE, 2018.
- [81] O. F. Kar and F. S. Oktem, “Compressive spectral imaging with diffractive lenses,” submitted.
- [82] T. Okamoto and I. Yamaguchi, “Simultaneous acquisition of spectral image information,” *Optics Letters*, vol. 16, no. 16, pp. 1277–1279, 1991.
- [83] A. Wagadarikar, R. John, R. Willett, and D. Brady, “Single disperser design

for coded aperture snapshot spectral imaging,” *Applied Optics*, vol. 47, no. 10, pp. B44–B51, 2008.

- [84] Y. Wu, I. O. Mirza, G. R. Arce, and D. W. Prather, “Development of a digital-micromirror-device-based multishot snapshot spectral imaging system,” *Optics Letters*, vol. 36, no. 14, pp. 2692–2694, 2011.
- [85] H. Arguello and G. R. Arce, “Colored coded aperture design by concentration of measure in compressive spectral imaging,” *IEEE Transactions on Image Processing*, vol. 23, no. 4, pp. 1896–1908, 2014.
- [86] D. L. Donoho, “Compressed sensing,” *IEEE Transactions on Information Theory*, vol. 52, no. 4, pp. 1289–1306, 2006.
- [87] X. Liu, Z. Wen, and Y. Zhang, “Limited memory block krylov subspace optimization for computing dominant singular value decompositions,” *SIAM Journal on Scientific Computing*, vol. 35, no. 3, pp. A1641–A1668, 2013.